THE FABRICATION OF PLASMONIC/PHOTONIC NANOSTRUCTURES IN POLYMERS: MECHANICAL SENSOR APPLICATIONS

A Thesis Submitted to
the Graduate School of Engineering and Sciences of
İzmir Institute of Technology
in Partial Fulfillment of the Requirements for the Degree of

DOCTOR OF PHILOSOPHY

in Materials Science and Engineering

by
Gökhan TOPÇU

July 2019
İZMİR

We approve the thesis of **Gökhan TOPÇU**

Examining Committee Members:

_____
Prof. Dr. Mustafa M. DEMİR
Department of Materials Science and Engineering, İzmir Institute of Technology

_____
Assoc. Prof. Dr. Yaşar AKDOĞAN
Department of Materials Science and Engineering, İzmir Institute of Technology

_____
Assoc. Prof. Dr. Mustafa EMRULLAHOĞLU
Department of Chemistry, İzmir Institute of Technology

_____
Assist. Prof. Dr. Nesrin HORZUM POLAT
Department of Engineering Sciences, İzmir Katip Çelebi University

_____
Assist. Prof. Dr. Elif ALYAMAÇ SEYDİBEYOĞLU
Department of Petroleum and Natural Gas Engineering, İzmir Katip Çelebi University

9 July 2019

_____   _____
Prof. Dr. Mustafa M. DEMİR   **Prof. Dr. Mehtap EMİRDAĞ EANES**
Supervisor, Department of Materials   Co-supervisor, Department of Chemistry
Science and Engineering

_____   _____
Assoc. Prof. Dr. Haldun SEVİNÇLİ   **Prof. Dr. Aysun SOFUOĞLU**
Head of the Department of Materials   Dean of Graduate School of
Science and Engineering   Engineering and Sciences

ACKNOWLEDGMENTS

ABSTRACT

THE FABRICATION OF PLASMONIC/PHOTONIC NANOSTRUCTURES IN POLYMERS: MECHANICAL SENSOR APPLICATIONS

Functional polymer nanocomposites offer futuristic properties by the association of inorganic additive micro-/nanostructures into the polymers. With the growing knowledge of the physical fundamentals, stimuli-responsive polymeric composites enable detection of chemical, thermal, and mechanical changes by optical sensors and probes. Since the accurate real-time detection of the change in mechanical loading is vital for construction and industrial fields, the use of colorimetric pressure elements in a static body is important for the prediction of catastrophic failures. In this thesis, strain/pressure responsive colorimetric films were produced. A number of polymer nanocomposite-based mechanical sensors are presented. By transferring the optical activity (coherent reflection and plasmonic coupling) of the additives into various polymeric matrices having different mechanical features, the strain and pressure sensors are developed for practical applications. There are two approaches used for the fabrication of polymeric mechanical sensors: i) PDMS/SiO$_2$ composites, ii) PAAm/Au NP composites. The coherent reflectivity of SiO$_2$ colloidal particle arrays was used to develop strain sensors while controllable localized surface plasmon resonance of Au NPs was employed for pressure sensors. These optical systems were separately associated with viscoelastic and elastic polymeric systems, and sensor properties were discussed.

ÖZET

POLİMERLERDE PLAZMONİK/FOTONİK NANO YAPILARIN ÜRETİMİ: MEKANİK SENSÖR UYGULAMALARI

Fonksiyonel polimer nanokompozitler, inorganik katkı mikro ve nanoyapıların polimerlere birleştirilmesiyle fütüristik özellikler sunar. Fiziksel temellere dair artan bilgi birikimiyle, uyarıcılara duyarlı polimerik kompozitler; optik sensörler ve problar tarafından kimyasal, termal ve mekanik değişiklikleri tespit etmeyi sağlar. Mekanik etkideki değişimin gerçek zamanlı olarak tespit edilmesi, inşaat ve endüstriyel alanlar için hayati öneme sahip olduğundan, statik bir gövdede kolorimetrik basınç elemanlarının kullanılması, felakete neden olabilecek kusurların tahmini için önemlidir. Bu tez çalışmasında, gerinim/basınç duyarlı kolorimetrik filmler üretilmiştir. Bir takım polimer nanokompozit temelli mekanik sensörler sunulmuştur. Katkı maddelerinin optik aktivitesini (uyumlu yansıma ve plazmonik eşleşme), farklı mekanik özelliklere sahip çeşitli polimerik ortamlara transfer ederek, pratik uygulamalar için gerilme ve basınç sensörleri geliştirilmiştir. Polimerik mekanik sensörlerin üretimi için iki yaklaşım kullanılmıştır; i) PDMS/SiO_2 kompozitleri, ii) PAAm / Au NP kompozitleri. SiO_2 kolloidal tanecik motiflerinin uyumlu yansıtıcılığı, gerinim sensörlerini geliştirmek için kullanılırken, Au nanotaneciklerin lokalize yüzey plazmon rezonansı basınç sensörlerinde kullanılmıştır. Bu optik sistemler ayrı ayrı viskoelastik ve elastik polimerik sistemler ile birleştirilmiş ve sensör özellikleri tartışılmıştır.

Dedicated to my wife and family…

TABLE OF CONTENTS

LIST OF FIGURES

LIST OF TABLES

LIST OF ABBREVIATIONS

CIE	Commission Internationale de l'Eclairage
DLS	Dynamic Light Scattering
EAP	Electroactive Polymers
EDX	Energy Dispersive X-Ray
EtOH	Ethanol
FA	Formaldehyde
FCC	Face Centered Cubic
FFT	Fast Fourier Transform
FTIR	Fourier Transform Infrared
FWHM	Full Width Half Maxima
IPA	Isopropyl Alcohol
LSPR	Localized Surface Plasmon Resonance
NP	Nanoparticle
PAAm	Polyacrylamide
PDMS	Polydimethylsiloxane
PDI	Polydispersity Index
PMMA	Polymethyl methacrylate
RGB	Red-Green-Blue
RH	Relative Humidity
SEM	Scanning Electron Microscope/Microscopy
SPR	Surface Plasmon Resonance
TEOS	Tetra Ethyl Ortho Silicate
UV	Ultraviolet
XRD	X-ray Diffraction

CHAPTER 1

INTRODUCTION

1.1. Motivation

Sensing is a function that provides information about the environment due to the interaction between system and medium. In our daily life, human beings use their sense mechanisms individually or synchronically, while working, running, or driving, etc. The human body is considered as one of the best model concepts of a complex system that consists of a number of sensors capable of sensitively and selectively detecting a wide variety of quantities or magnitudes. The most common macro sensors in the human body are those that provide vision, hearing, smell, taste, and touch, which are called the five senses. For instance, the human eye can distinguish colors and shapes, as well as perceive the size, dimension, or motion of objects. A conventional example for a combination of the aforementioned parameters is the recognition of a face. Perceiving difference and recognizing a familiar face in a crowd is evidence of the advanced selectivity in the vision system. Nevertheless, the human visual system has a limited dynamic range, which is defined as the visible part of the electromagnetic spectrum, namely, from wavelengths of 400 nm (violet) to 700 nm (red). This represents a very small fraction of frequency range (from 7.32×10^{14} cycles per second (cps) to 4.55×10^{14} cps). On the other hand, the human ear is an example of a precise sensor with a limited dynamic range. Particularly, the ear is able to sense sound levels as low as 10^{-12} W/m^2 (~0 dB) and as high as 1 W/m^2 (~120 dB), above which is the threshold of auto-protection appearing as pain. The frequency range for the ear is limited between 20 Hz and 20 kHz.

Typical smart sensors exist in not only our bodies but also our world. For instance, while the day starts with an alarm clock, we then proceed to go to work by using an automobile, which may have tens of different sensors helping in the operation and control of the vehicle. At our workplace, there are various types of sensors that can be either very simple, such as temperature, smoke, and humidity sensors or quite complex, such as

sensors to detect potential explosives, metal objects, etc. Classification of the sensors in logical design is a difficult challenge due to their multitude. One possible way is to categorize these into groups according to their design, fabrication, or utilization. Although it is impossible to list all the potential needs that may result in the development of a particular sensor, the needs may be grouped into various areas. Among these systems, scientific societies have interesting sensors that convert biological, chemical, and mechanical input to optical, electrical, or mechanical output due to their possible advantages in daily life.

During the contact of two objects, they exert force on each other. Hence, the average interface pressure is the total force divided by the area of the interface. To characterize the force onto interface as a measurand, pressure sensor applications have a vital role. The sensor technology is a practical application that perceives the pressure and converts it to electrical or optical signals. Recently, pressure sensor applications are not only a research field for solid state but also a qualified technique to measure the pressure that is exerted by liquid or gas. Typical pressure sensor systems consist of the sensor chip, receiver, and converter. In the design of sensor chips (transducer), phase of a measurand, magnitude and distribution behavior of pressure are considered for manufacturing an efficacious device.

In this thesis study, we focus on the development of stimuli-sensitive materials are based on giving distinct optical output upon external mechanical force. The systems are designed as an integration of photonic and plasmonic nanostructures, namely SiO_2 and Au nanostructures, into the polymeric systems. Their structural and optical characteristics against mechanical stimulus were investigated in terms of sensor application.

1.2. Structure and Scope of the Thesis

The first chapter of the thesis presents the main idea and purpose behind studies conducted during researches. In *Chapter 2*, the historical development of the mechanical sensors is reviewed. The studies conducted within the scope of the thesis are discussed in detail in *Chapter 3* and *Chapter 4* and divided depending on the underlying mechanisms of the optical nanostructures that are employed: photonic and plasmonics. In *Chapter 5*, the general concluding remarks and future prospects based on employing photonic/plasmonic nanostructures as an optical element for sensor applications are presented.

1.3. Characterization Methods

During the thesis studies, the size distribution of both SiO_2 and Au NPs was measured using Dynamic Light Scattering (DLS; Malvern, Zetasizer ZS90, UK). The morphology of the particles was studied by Scanning Electron Microscopy (SEM; Quanta 250, FEI, Hillsboro, OR, USA). During the colloidal particle synthesis, pH was measured by using a multimeter (pHenomenal® MU 6100 L, VWR International, Vienna, Austria). Images of the photonic films were captured by a camera (Canon EOS 5D, Tokyo, Japan) while the plasmonic pressure-sensitive films were recorded by a smartphone (Apple, Iphone 7, CA, USA). The crystallographic pattern of composites was recorded by X-ray diffraction (XRD; (X'Pert Pro, Philips, Eindhoven, the Netherlands). The optical properties of whole materials were recorded using USB2000+ spectrometer (Ocean Optics Inc., Dunedin, FL, USA) via a premium fiber cable.
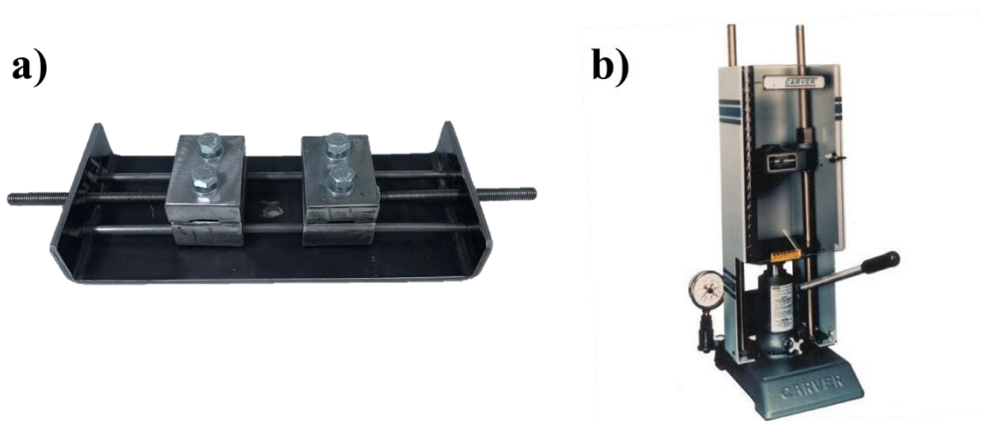
Figure 1.1. The apparatuses to apply (a) strain and (b) pressure to resulting materials during the thesis study.

The deformation of mechanical-responsive of polymeric composites was carried out by two different apparatuses. For strain responsive elastomers the lateral deformation was applied by using lab-made tensile apparatus consisting of clamps and screws placed on fixed-rails (Figure 1.1a). For pressure-sensitive composites, the controlled pressure is applied by a hydraulic pressure apparatus (Carver Inc., Model #3925, Wabash, IN, USA)
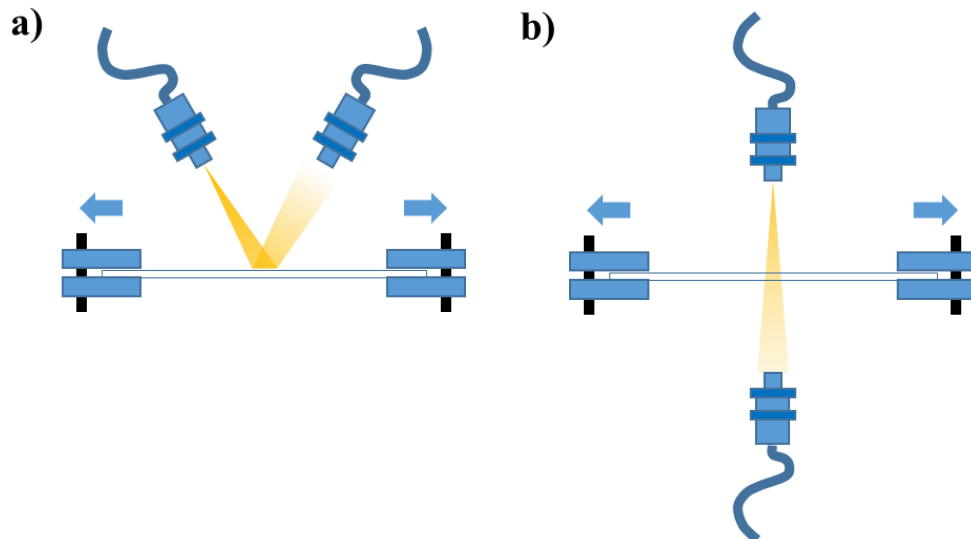
Figure 1.2. Schematic representation of (a) reflection, (b) transmission and absorption measurements of mechanical-responsive composites.

(Figure 1.1b). The samples were loaded between two parallel plates of the system and the desired pressure was applied onto materials.

The optical characterization that is carried out in both reflection, transmission, and absorption mode showed in representative cartoon demonstration in Figure 1.2. Fiber optic cables that are connected to light source and spectrometer located over the reflective surface of photonic and plasmonic films. Since the inside of the composite layer could not be characterized clearly in reflection mode, transmission and absorption modes were also used to examine the changing opacity and color of the material. In this case, cables are deployed as two-sided. For both modes, spectral information was recorded in various deformation levels. To characterize the color of the films, reflection mode was used since the color generation of strain-responsive films is based on structural interference. On the other hand, previously deformed pressure-sensitive films were characterized in absorption mode since the underlying mechanism is plasmonic.

CHAPTER 2

A BRIEF HISTORY OF MECHANICAL SENSORS

For a number of centuries, measurement of pressure has attracted significant attention. The first recorded observation was performed by Galileo Galilei, an Italian inventor and scientist who lived in the 17th century. Galilei developed the first pumping machine to irrigate a land via water from the river. During the process of the machine, it was observed that 10 meters is the rising limit of the water in the pump. However, there was no sensible explanation for this observation. After almost one century, the first empirical pressure measurement was carried out by Evangelista Torricelli using a tube, which was one meter long and filled with mercury, hermetically closed from one end. The column of mercury invariably fell to about 760 mm leaving an empty space above its level. These two experimental findings were interpreted and formulized in 1648 by Blaise Pascal, who defined "pressure" as the uniform distribution of the force on the exerted surface.

First attempt to measure atmospheric pressure via aneroid barometer system instead of a liquid was made by Lucien Vidie in 1844. The system was based on spring, whose extension was mechanically amplified on an indicator mechanism and was patented in 1849. After a couple of decades, electrical measurement methods began to be developed using transduction strategy. In 1930, Roy W. Carlson, who worked on the construction of dams, invented an unbonded wire strain gauge to measure compressive strain in concrete structure.[1] The strain gauge was designed in a sealed metal case with flanges and covered with a rubber sleeve. The setup consisted of a number of resistive wires whereby half of them were stretched and the rest were only strained under the exerted strain. Although the device worked well for the purpose, there were a number of limitations, including narrow pressure, fragile wires, and transportation issue. Alternatively, a couple of designs were made in the same decade, such as carbon resistor and bonded wire. These systems provided various advantages for measurement. For instance, carbon resistor based gauge

had a small size and low weight that offered simplicity for transportation, whereas the bonded wire gauge was able to carry out the more precise measurement.

The discovery of piezoresistivity in semiconductors led to the beginning of a new era for pressure measurement.[2, 3] In 1954, Charles S. Smith discovered piezoresistive properties of semiconducting germanium and silicon, which could not be explained through previously known mechanisms.[4] Within the following decade, the first piezoresistive sensor was developed and improved by using various designs. The resistive element was applied onto a silicon substrate. The system was not equipped with backing which provides ease of binding between the metal diaphragm and the silicon substrate by means of epoxy. Compared to the conventional foil and metal-wire gauges, the semiconductor counterpart had an electrical output almost 100 times larger. Nevertheless, using an adhesive which causes creeping and hysteresis was still disadvantageous for measurement. To overcome the obstacles originating from the adhesive, diffused semiconductor strain gauges were made by using photolithography. Besides surpassing hysteresis and creeping, the design had a number of other advantages such as small size, higher resistivity, higher fatigue limit, and higher sensitivity. Today, this design still plays a key role in sensor technology. In the 1970s, capacitive pressure transducers were discovered, which had quartz having doughnut-like shape. Inside of the doughnut, there was a vacuum cavity, which consisted of the two capacitor plates. On the outside of the body, two thin film sensor elements were deposited.[5] The lack of sensitivity by changing temperature is the main handicap for capacitive pressure transducers. Therefore, the quartz body was replaced by a ceramic one.[6] The transducer had upper and lower halves, which were gathered by the molded glass. The cavity between both halves is filled by a very small absolute pressure. This design is still used in modern sensors.

In daily life, many pressure sensor designs have been employed for various applications. Therefore, these devices may be classified by considering their working principle.[7] According to their designs, they can be divided into three groups, which are load cells, tactile sensors, and pressure indicating films. On the other hand, the sensor systems can be classified as electromechanical, potentiometric, capacitive, or reluctive, based on the working principle.

One of the commonly-used devices is load cell, which works by measuring the force acting on a given surface. Load cells are also used to measure weight in industrial

applications. They can be installed on hoppers, reactors, etc. to control their weight capacity. There are various load cell designs, which are based on electromechanical, pneumatic, and hydraulic systems. For electromechanical process, the load cell perceives a change in pressure by measuring the alteration in resistance of a Wheatstone Bridge Circuit. Piezoelectric materials are also employed in load cells, which are based on the same principle of deformation as the strain gauge load cells. However, the voltage output is generated by deforming the basic piezoelectric material. When precision mechanical balances are required and where intrinsic safety and optimal hygiene is essential, pneumatic type load cells are a better option since they contain no fluids that may contaminate the process if the diaphragm ruptures. In the case of remote operation, the most applicable load cell is the hydraulic one. Hydraulic load cells have a piston that raises the hydraulic fluid as force increases. The pressure may be locally indicated or transmitted for remote control or indication.

Tactile pressure sensors are used to measure dynamic changes in pressure.[8, 9] Compared to load cells, they work at lower magnitudes. Pressure sensor arrays are large grids, which are termed as tactel. Each tactel is capable of detecting specifically exerted forces. The arrays are usually formed as thin film. Tactel-based sensors provide a high resolution 'map' of the applied pressure. In addition to spatial resolution and force sensitivity, systems-integration issues such as signal routing and wiring are important for these kinds of sensors. They are primarily used in the manufacturing and R&D processes as an analytical tool and have been adapted for use in the robotics industry. Examples of such sensors available for consumers include arrays built from lead zirconate titanate (PZT), conductive rubber, poly(vinylidene fluoride) (PVDF) and its composites, and metal-like capacitive sensing elements.

In a typical pressure measurement, experimental conditions may differ from theoretical assumptions. For instance, it is necessary to record a peak pressure while the interface pressure is non-uniformly distributed. In this sense, pressure-indicating films are good candidates for the examination of pressure distribution. Instead of electrical output, the films are based on optical output. For instance, *Lee et al.* fabricated mechanochromic polymer composite films and examined their optical responses upon mechanical force.[10] The coloration of the films is based on photonic interference due to periodic dielectric structure, and is known as Bragg-Snell Law.[11, 12] The underlying sensing mechanism of the pressure-indicating photonic film is the change in interplanar distance between two

nanostructure arrays. During the application of lateral strain, interplanar distance lowers, which causes a dramatic decrease in wavelength of reflected light. Another type of pressure indicating the film is designed by taking advantage of plasmonic nanoparticles.[13] *Han et al.* reported the colorimetric pressure sensors including Au nanoparticles showing plasmonic absorption in poly(vinyl pyrrolidone). Due to their tunable optical absorbance (due to the change in color of the particles upon aggregation), embedded-plasmonic particle aggregates disintegrate each other according to mechanical force. Therefore, color change directly indicates the magnitude of the applied pressure.

Besides the classification based on working mechanism and design, the sensor systems can be sorted according to the type of pressure sensitive element. As previously described, the pressure sensitive element can provide either an optical or electrical signal. In the electrical one, they can be divided into electromechanical,[14-16] potentiometric,[17] capacitive,[18] or reluctive[19] signals. Piezoelectric and electroactive polymer (EAP) systems are commonly used as an element for electromechanical systems. In a typical piezoelectric crystal-based sensor, pressure-induced twisting of a crystal leads to the formation of a small amount of electric charge. Hence, the amplitude of pressure is proportional to the intensity of the electric charge and its precision reaches up to 0.1 MPa. Potentiometric sensors work on the basis that change in pressure causes a movement of an arm back and forth across a potentiometer influencing the resistance. They have an arm attached to the elastic pressure-sensing material. Note that, the sensing material in the system has a working range due to their mechanical limit that restricts the resolution of the system. Potentiometric pressure sensors are efficient candidates to use as a cheap detector evaluating a coarse process. The sensor is designed to operate within a wide pressure range with high sensitivity (~0.07 MPa). A capacitive sensor consists of two parallel plates and an electrode connected to a diaphragm that is able to sense the pressure difference between two sides (applied and reference sides). Displacement along the diaphragm is detected by an electrode, which leads to fluctuation in capacitance. An attached circuit detects the change in capacitance, in which turn read the voltage in relation to pressure change. The flexible element is stimulated by moving the ferromagnetic plate, which leads to a change in the magnetic flux of the circuit. One of the conditions in which reductive pressure is employed is when the inductive sensor does not generate a precise enough measurement. Therefore, the pressure range is relatively narrow and sensitivity is lower (~0.35 MPa) compared to potentiometric counterparts.

The fabrication of pressure indicating films can be done by mixing the particles with a polymer solution that provides homogeneous diffusion into the matrix and using simple drop-casting method to produce the films.[13] To measure a reversible change in pressure, structural colored elastomers are promising candidates instead of plasmonic resonance based colored films. The elastomers having opal or inverse opal structure are fabricated by using both top-down and bottom-up strategies. For instance, building blocks of origin of coloration can be obtained by using Stöber or emulsion polymerization, which resulted in uniformed-size SiO_2 or polymeric beads, respectively. For integration of building blocks into elastomer, several techniques are used such as capillary force induced assembly [10] and drop-casting onto glassy film having nanoparticles in the periodic nanostructure.[20] Besides, lithographic techniques are also used to produce periodic nanostructures onto the film for pressure measurement in wearable devices.[21]

CHAPTER 3

FABRICATION OF PHOTONIC NANOSTRUCTURES AND STRAIN SENSOR APPLICATION

3.1. Fabrication of Photonic Crystal/Glass by Colloidal SiO$_2$

Color is an important information carrier between the environment and color sensitive living organisms. As a well-known interesting example, chameleons have the unique ability to exhibit rapid color changes when they feel danger or during social interactions such as male contests or courtship.[22] Color is, in fact, an integral part of daily life [23-30] not only for animals but also for human beings including art, decoration, and clothing. In general, three different types of mechanisms are known to be responsible for color generation: 1) absorption of particular wavelength resulting in the reflection of others, which is responsible for the coloration of flowers, paints, dyes, pigments, etc.;[31] 2) emission at specific wavelengths such as LEDs;[32, 33] and 3) structural colors [34] based on diffraction, scattering, and dispersion of light as a result of its interaction with the periodic materials. The first method suffers from photobleaching,[35, 36] toxicity,[37] and poor color quality due to absorption and reflection. Coloration as a result of the second method can provide bright and pure colors but necessitates external power supplies. The third one, on the other hand, shows no photobleaching[38] and can generate a wide range of colors[39, 40] through non-toxic and environmentally-friendly means.

Structural coloration is a well-known phenomenon and is commonly observed in nature, e.g., the *Morpho* butterflies,[41] beetles, etc.,[42, 43] and attracts great attention.[34, 44-48] This type of coloration can be divided into two groups depending on its behavior with respect to the angle of observation: irisdescence[44, 46, 49, 50] and non-iridescence.[51, 52] The former one offers colors, which are generated from structures that contain periodically arranged nano- or microparticles, depending on the observation angle (iridescence). These periodically arranged and colored structures are named as *photonic crystals*. On the other

hand, the latter possesses a quasi-ordered arrangement of colloids called *photonic glass* and offers the opposite; angle-independent color generation (non-iridescence). In this case, unlike the photonic crystal, the arrangement of the colloidal particles shows a glassy structure and short-range order. This type of coloration finds a wide range of potential applications such as reflective displays, colorimetric sensors, and, textiles, etc.[38, 51, 53-58] In general, there are various methods developed for the generation of non-iridescent structural color using polymeric or inorganic colloidal systems.[38, 51, 52, 59-65] For instance, *Takeoka et al.* reported the formation of non-iridescent film using uniform SiO_2 colloidal particles of 280-360 nm diameter by spraying.[38] It was argued that fast solvent evaporation in the course of spraying process allows the formation of the colloidal amorphous array, which is, in fact, the main requirement of non-iridescence. Clogging of spraying nozzle appears to be a common handicap in the processing of colloidal dispersions. *Harun-Ur-Rashid et al.* achieved the amorphous array by mixing of two monodisperse SiO_2 colloids with two populations of different size of 220 and 310 nm..[66] While large colloidal particles form the periodic structure, small ones were employed to deteriorate the regularity of the colloidal crystal arrangement. Silica is a cheap, abundant, easily-prepared material and it is also capable of being associated frequently with functional counterparts. As an example, *Wang et al.* employed ZnS as a core that is encapsulated by SiO_2 to achieve saturated emission.[67] ZnS is a typical II-VI type of semiconductor giving bright and intense emission in the visible region. Another metal oxide core - SiO_2 shell system has been reported by *Lee et al.*[68] The authors employed Fe_3O_4 core to obtain both structural color and magnetic response from the resulting colloidal film. Apart from binary material components, using a unary system, for instance merely uniform-sized SiO_2 colloidal particles without involving a second material, and/or employing tedious process may simplify the formation of photonic glass with non-iridescent color.

In this part of the thesis, non-iridescent coloration is achieved using merely SiO_2 colloidal particles. The preparation of SiO_2 colloidal films includes isolation of monodisperse particles and their re-dispersion into fresh solvent as aggregated-colloidal particle domains. Then, the photonic glass is obtained by evaporating the re-dispersed colloids over a substrate. Moreover, the colloidal particles with a diameter of 150-300 nm generate various angle-independent colors such as violet, blue, green, or orange depending on the particle size. This approach offers a facile way of generating non-iridescent colors that

can readily be applied to colorimetric applications including sensors, decoration, and textile.

3.1.1 Materials and Methods

Tetraethyl orthosilicate (TEOS, >99.9%, Sigma Aldrich) and ammonia solution (25%, Sigma Aldrich) were purchased and used without any further purification. Ethanol (EtOH, >96%, Tekkim) was employed as a solvent. The residual moisture in reactants and solvent was removed by molecular sieve (4Å pore size).

3.1.2 Preparing the Photonic Nanostructures

Monodisperse SiO_2 colloids were synthesized by using a modified Stöber method.[69] Initially, the mother solution containing ammonia (in range between 1 to 2 mL) and EtOH (in the range between 15 to 40 mL) was prepared in Erlen flask and homogenized for 5 min. Subsequently, TEOS (1 mL) was added to the mixture and the reaction was maintained for 1 h at room temperature. The SiO_2 particles were collected by centrifugation (6000 rpm for 5 min) and washed with EtOH for three times to eliminate unreacted TEOS and ammonia. Isolated SiO_2 particles were then re-dispersed into EtOH such that the concentration of re-dispersed particles was fixed at 5 mg/mL.
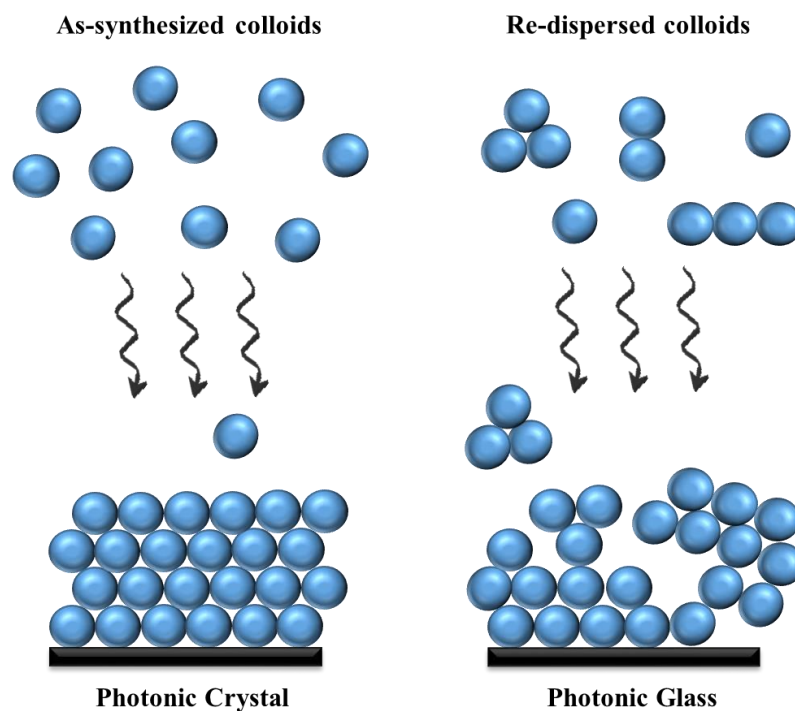
Figure 3.1. Schematics of the formation of ordered SiO_2 colloidal particles in photonic crystal and photonic glass.

Photonic crystals were obtained through the sedimentation of the as-synthesized colloidal particles on a substrate upon solvent evaporation. An aliquot of (4 mL) the SiO_2 colloids mentioned above was cast onto a Petri dish (diameter: 5 cm). Drying of colloids was carried out at room temperature under 200 mbar for 24 h. On the other hand, photonic glasses were prepared in two steps: i) isolation of the colloids by centrifugation (6000 rpm for 5 min) and ii) re-dispersion of the colloids into a fresh solvent. The resulting dispersion was cast on a substrate; an assembly of the SiO_2 colloidal particles is obtained after solvent evaporation. Schematic illustration of the preparation of photonic nanostructures is presented in Figure 3.1.
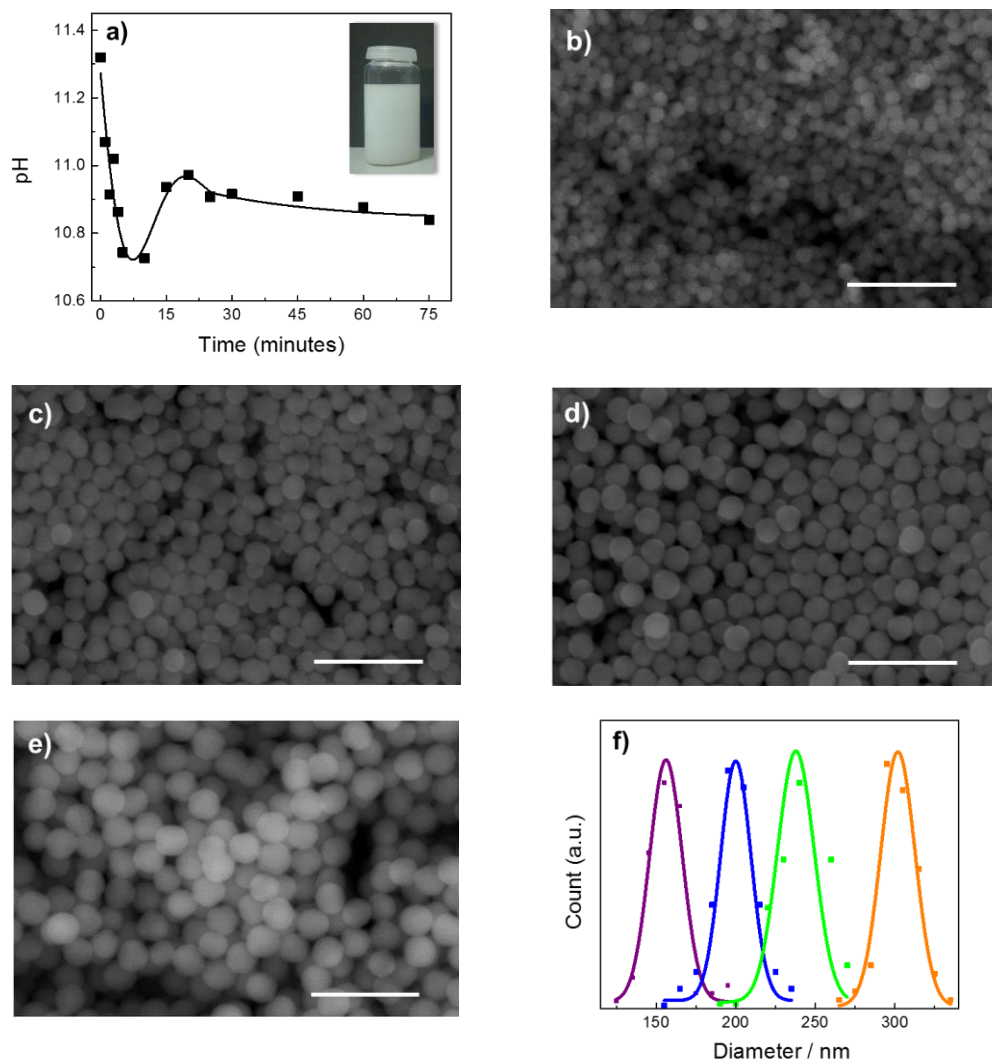
Figure 3.2. (a) pH of the reaction medium in the course of SiO_2 synthesis. The inset shows photographic image of representative colloidal SiO_2 dispersion. SEM images of various size SiO_2 colloids. Scale bar indicates 1 μm. [b) SiO_2-violet, c) SiO_2-blue, d) SiO_2-green and e) SiO_2-orange]; (f) particle size distributions (d_{SEM}) of the SiO_2 colloidal particles in various ratios of EtOH:TEOS.

3.1.3 Results and Discussion

TEOS is the source of SiO_2. It is hydrolyzed in a basic reaction medium such that -OH groups are readily substituted with C_2H_5O- that leads to the formation of silicic acid, $Si(OH)_4$. The pH of the medium accordingly decreases from 11.3 to 10.7. (Figure 3.2a) The condensation of $Si(OH)_4$ develops the formation of SiO_2 clouds. When the SiO_2 clouds reach a critical mass, which is considered to be of 2-3 nm diameter, nuclei are born.[70] The consumption of –OH group causes a slight increase of pH to 11.0. The nuclei are insoluble primary particles and tend to aggregate in alkali medium to reduce their surface area. Hence, larger colloidal particles begin to form as a result of their association. Figure 3.2b-e shows SEM images of the colloidal particles prepared at various TEOS:EtOH compositions. The size of the colloids gets larger as the concentration of TEOS increases. Table 3.1 presents synthesis conditions and the feature of the resulting colloids. A direct correlation was found between the amount of EtOH and diameter of the

Table 3.1. The features of the SiO_2 colloids at various conditions.

	ratio (v:v)		d_{SEM} (nm)	d_{DLS} (nm)	PDI	$\lambda_{refl.}$ (nm)
	EtOH	TEOS				
SiO_2-*violet*	40	1	157	181	0.021	380
SiO_2-*blue*	30	1	204	236	0.011	435
SiO_2-*green*	20	1	233	279	0.019	498
SiO_2-*orange*	10	1	301	347	0.029	578

SiO_2 colloidal particles. As the amount of EtOH increases, the mean diameter of the colloidal particles is reduced from 301 to 157 nm most probably due to the dilution of the reactants. The fifth column of Table 3.1 shows the results of the same colloidal dispersion obtained by DLS. The number size distributions are given in Figure 3.2f. Consistent with the results obtained by SEM, there is a systematic decrease of the mean diameter of the colloids with increasing the amount of solvent (EtOH). The distributions are uniform and Gaussian type. Note that the size obtained by DLS is nearly 20% larger than the one obtained by microscopy. The difference may be based on the fact that the diameter in SEM is measured under vacuum while DLS measures hydrodynamic diameter (*Rh*) of the
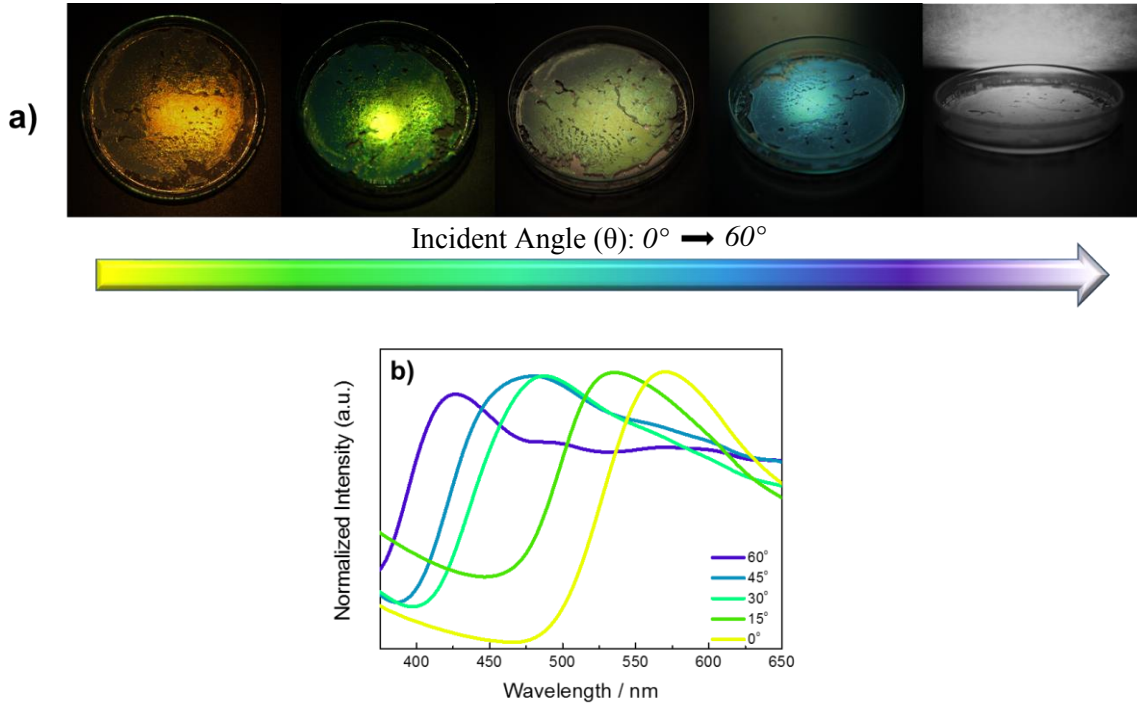
Figure 3.3. (a) Photographs and (b) reflection spectra of the *iridescent* photonic crystal film.

colloidal particles in solvent. Since the silanol groups on the surface of the colloidal particles form hydrogen bonds with surrounding water molecules, namely adhering a thin electric dipole layer of the solvent to the surface of the particle, size distribution appears larger in DLS than the corresponding particles in the dry state (SEM). The inset of Figure 3.2a shows a representative SiO_2 dispersion. Independent of the size, the dispersions are milky due to the optical scattering of the colloidal particles.

The as-synthesized colloidal dispersion is cast on a glass substrate. Solvent evaporation at room temperature leaves behind a photonic crystal film composed of SiO_2 colloidal particles. Figure 3.3 shows photos and spectra of the resulting representative photonic crystal at various angles. The upper frame (Figure 3.3a) presents that the same film takes color from yellow to blue depending on the angle of observation. Figure 3.3b shows reflection spectra of the photonic crystal at various angles. The shape of the spectrum and wavelength corresponding to maximum intensity were found to vary. The wavelengths at maximum intensity changes from 570 nm to 425 nm (blue shifting) as the angle increases. Iridescent coloration satisfies the following Bragg-Snell equation

$$\lambda_{max} = 2d_{(111)}\sqrt{(n_{eff}^2 - sin^2\theta)} \tag{3.1}$$

Obviously, the wavelength of the reflected light depends on the incident angle θ, lattice spacing of the face-centered cubic (FCC) structure, i.e. $d_{(111)}$ (corresponding to the close-packed structure), and effective refractive index n_{eff}. The index is considered to be additive on the basis of volume fractions of SiO$_2$ and air. The parameters ($d_{(111)}$ and n_{eff}) can be calculated as follows:

$$d_{(111)} = \frac{\sqrt{3}}{2}D \qquad (3.2)$$

$$n_{eff} = n_s V_s + n_{air}(1 - V_s) \qquad (3.3)$$

where diameter of SiO$_2$ sphere D is 262 nm, and refractive indices of SiO$_2$ (n_s) and air (n_{air}) are 1.45 and 1.00, respectively; V_s refers to volume fraction of SiO$_2$ colloidal particles in crystal that is 0.74 for the close packed fcc structure. Theoretically, calculated λ_{max} are found as changing from 566 to 430 nm in case of using observation angles from 0° to 60°, which are compatible with the obtained wavelengths from the observation.
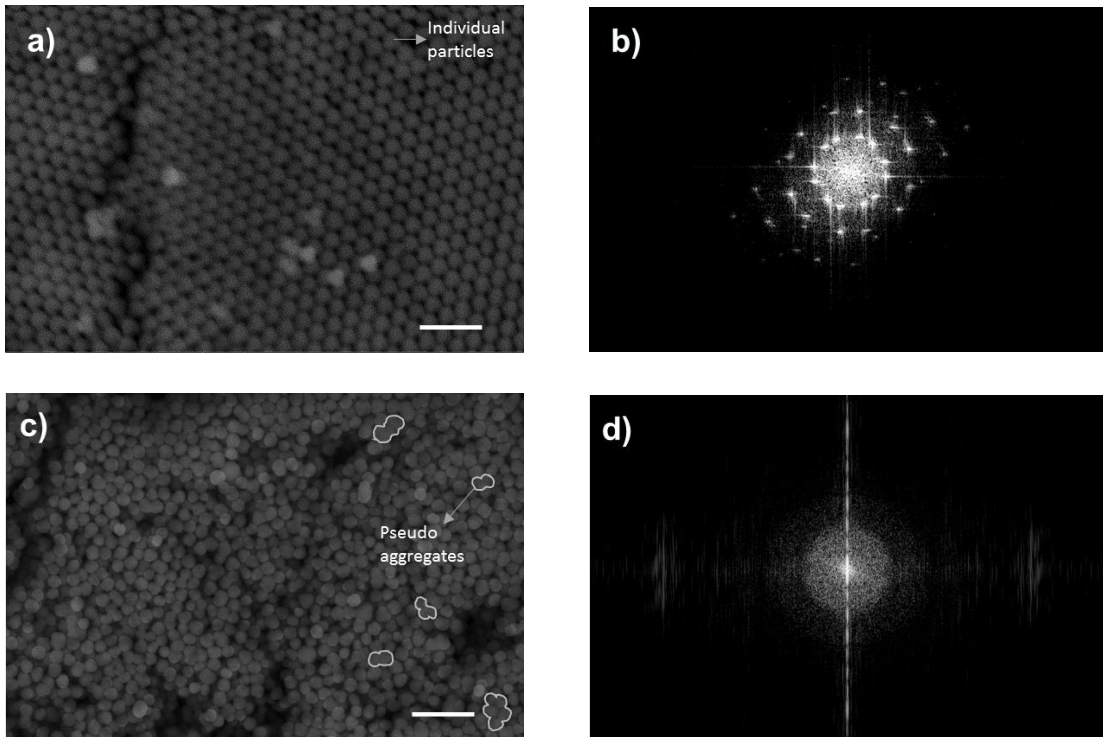
Figure 3.4. SEM image and corresponding FFT pattern of photonic crystal (a, b) and photonic glass (c, d) (Scale bars indicate 1 μm).

An overview SEM image of the photonic crystal film is given in Figure 3.4a. Colloidal particles are arranged periodically which leads to a long-range structural order. *Fast Fourier Transform (FFT)* is run through this electron micrograph using ImageJ. Sharp

16

spots are observed in the diffraction pattern (Figure 3.4b) indicating close-pack ordered formation and specific positions of the colloidal particles in the crystal. Monodisperse colloidal SiO_2 particles allow the formation of ordered structure in long-range since they are able to fill the gaps due to their size matching.[46, 47, 49, 71]

In order to obtain photonic glass, the as-synthesized SiO_2 colloids were initially subjected to centrifugation. Fresh solvent is added onto the resulting colloidal precipitate such that the colloids are re-dispersed in the solvent volume. It is known that once the colloidal particles are isolated and packed, it is hard to re-disperse them as individual particles because they already reduce their surface energy by aggregation. Thus, the aggregates of individual particles inevitably appear in the dispersion along with individual particles. The casting of this dispersion over a substrate provides a colloidal film where the arrangement of the particles is not well-ordered contrasting to the structure of the photonic crystal; rather, a quasi-ordered structure is developed. Figure 3.4c shows SEM image of the film prepared by re-dispersed SiO_2 colloidal particles. The resulting diffraction pattern after running FFT over this electron micrograph demonstrates that there are no sharp spots (Figure 3.4d). This result suggests the absence of periodic arrangement of the colloidal particles, i.e. there is no long-range structural order in the photonic film. Unlike the individual particles in Figure 3.3a, pseudo-agglomerated particle domains (Figure 3.3c) cannot be accumulated in compact packing due to the mismatch of the size of the colloidal domains. In other words, the centrifugation and re-dispersion cause the formation of SiO_2 colloidal aggregates and allow them to accumulate randomly.

Although the same dispersion is processed, the average size of these colloidal particles in the photonic crystal is larger (d= 262 nm) than the one in the photonic glass (d=204 nm). This difference can be attributed to the presence of residual NH_3 in the crystal film. NH_3 is one of the ingredients that cause the colloids to continue to grow even after the formation of the photonic crystal. Since it is washed out during the centrifugation, the concentration of NH_3 is diminished so that the growth stops in the preparation of photonic glass. Figure 3.5a shows the photographic image of a photonic glass prepared by this approach (centrifugation and re-dispersion of the colloidal dispersion) at various angles of observation. The resulting film has a blue color and does not vary depending on the angle of viewing. Unlike the spectral feature of the photonic crystal film shown in Figure 3.2b, both the shape and λ_{max} of the reflection spectra of the film in Figure 3.5b are almost unchanged suggesting the generation of the non-iridescent color. This approach was
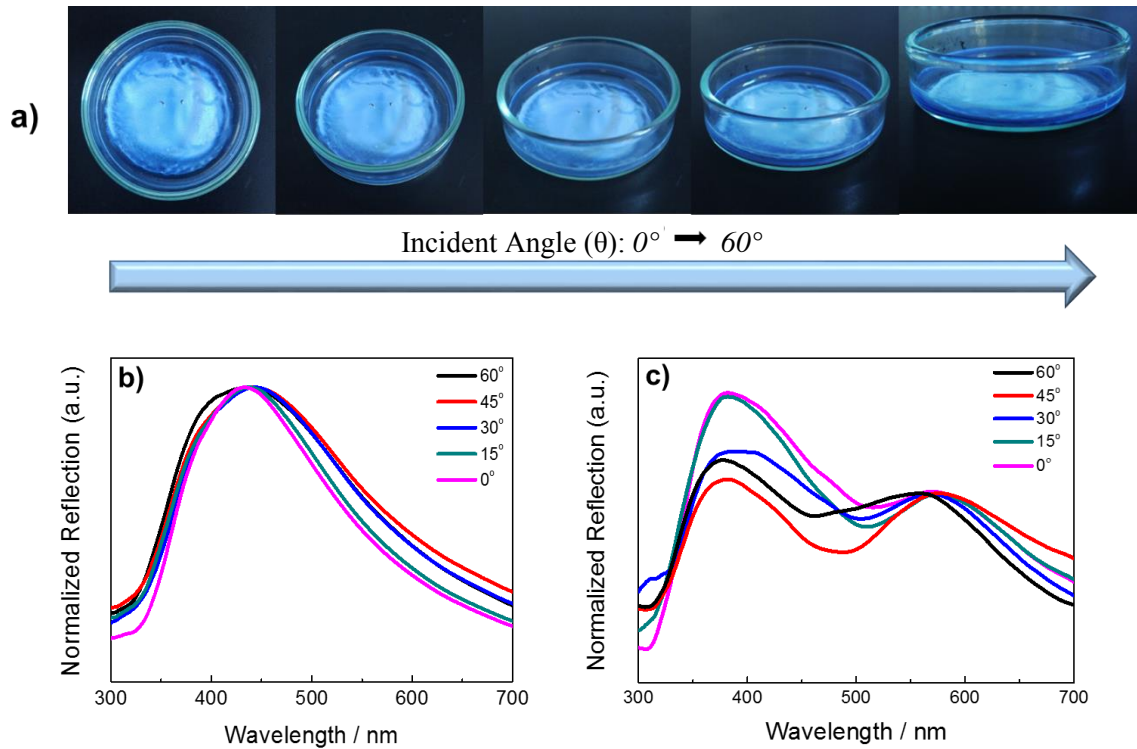
Figure 3.5. (a) Photographs of the *non-iridescent* blue photonic glass. The reflection spectra of quasi-ordered photonic glass film, (b) blue and (c) orange.

successfully applied to the fabrication of other visible colors by simply controlling the size of the colloidal particles. Figure 3.5c presents the reflection spectra (normalized with respect to the maxima of the long wavelength signal) of the photonic glass prepared by SiO_2 with 301 nm in diameter showing orange color. The spectra provide two reflection signals at 390 and 575 nm. The placement of the signals remains almost unchanged for all angle of incidence employed. Figure 3.6a shows the photographic images of the photonic glasses prepared by SiO_2 colloids of various size from 157 to 301 nm. As the diameter increases, non-iridescent colors shift from violet to orange. Figure 3.6b presents the reflection spectra of these photonic films. It is seen that violet and blue colors show a single signal inside the visible range. However, for green and orange colors, two signals appear. As in case of orange, similar set of signals at 385 and 500 nm are observed in green. The reflection signal at long-wavelength is primarily due to coherent scattering from the particle assembly. On the other hand, the origin of reflectivity at short wavelengths is under debate in literature. Attempts have been made to understand the occurrence of this signal because the structural color in photonic glasses arises from the combination of both signals.[66, 72-74] It plays significant role in the fabrication of non-iridescent structural colors. *Noh et al.*[75, 76] reported the effect of multiple (single and

double) scattering. The authors claimed that the appearing at short wavelength results from double scattering of light by the correlated structures in short range. This scattering could be one possible reason for this poor color saturation observed at longer
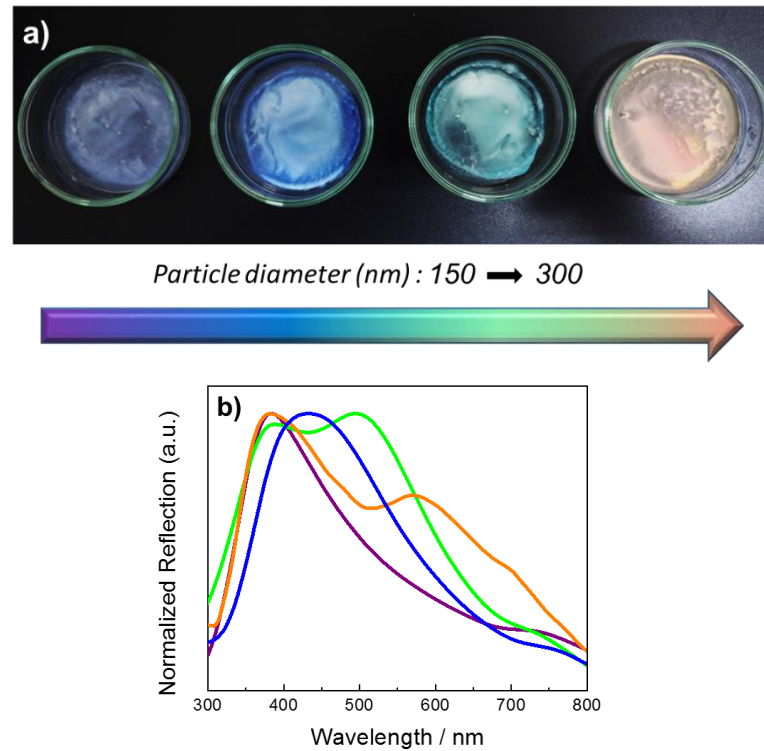
Figure 3.6. (a) Photographs of the non-iridescent photonic glass films that are formed by SiO_2-violet, SiO_2-blue, SiO_2-green, and SiO_2-orange. (b) Reflection spectra of the resulting films.

wavelengths, particularly in red. Another possible reason could be the single particle resonance that may develop multiple scattering in such colloidal materials. Manoharan's group[77] pointed out that the scattering behavior of the constituent individual particles plays a key role. The interference of light inside the particles leads to enhanced scattering at wavelengths other than those related to the interparticle correlations. Individual particles backscatter light arising from cavity modes more strongly in blue; thus, it is hard to achieve angle independent red in structural color. For violet and blue non-iridescent colors, the scattered light from the particles falls into UV region that does not affect the resulting color at least taking into account the perception of the eye. However, in the case of longer wavelengths, scattered light from individual particles starts to fall into visible, particularly around the blue region. This scattering may reduce the color saturation and even can shift the perceived color toward blue.[77] In this sense, the fabrication of violet, blue or green non-iridescent colors is easier and more common compared to red color generation in nature.

The wavelengths showing maximum intensity (λ_{max}) as a function of incident angle θ are presented in Figure 3.7a. Black circles represent the colloidal film prepared by individually dispersed SiO_2 colloidal particles, while squares refer to the one obtained by re-dispersed SiO_2 colloidal particles. In the former case, wavelengths are found to decrease with the increasing observation angle (iridescence). More than 100 nm shift is evident in λ_{max} depending on the angle of observation from 0° to 60°. However, in the latter one, the wavelength remains unchanged with respect to incident angle θ (non-iridescence). *The Commission Internationale de l'Éclairage* (CIE) 1931 chromaticity diagram is given in Figure 3.7b. As the incident angle θ increases, the generated color shifts from red to blue for the iridescent film; however, it remains almost unchanged at the blue region at every angle for the non-iridescent one.
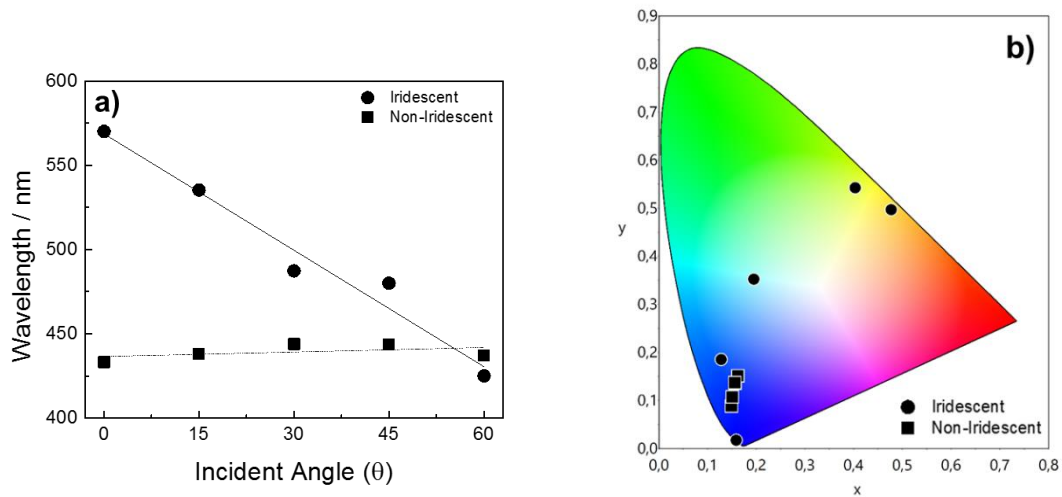
Figure 3.7. (a) λ_{max} of both photonic glass and photonic crystal (iridescent) film as a function of incident angle. (b) CIE coordinates of the both photonic

3.1.4 Conclusions

In this part, a non-iridescent photonic glass of various colors violet, blue, green, and orange were prepared from SiO_2 colloids. The colloids of submicrometer size (150-300 nm) were obtained by traditional Stöber method. The casting of the as-synthesized SiO_2 colloids on a solid substrate allows the production of the photonic crystal. The crystal exhibits an iridescent coloration. The re-dispersion of the isolated particles into fresh solvent develops pseudo-aggregation for the colloidal particles. The casting of the re-dispersion does not allow the formation of long-range order; rather leads to a quasi-ordered photonic glass. The coloration of the resulting films is independent on the angle of observation (non-iridescent). In other words, a single centrifugation step in the

procedure makes a clear difference in the arrangement of the colloidal particles. The size of the individual colloidal particles is still the dominant parameter in the determination of the non-iridescent structural color. As the particle size increases, the obtained non-iridescent color shifts towards orange. Considering the absence of long-wavelength non-iridescent structural colors in nature, this method can be a reliable approach (centrifugation and re-dispersion) obtaining angle-independent orange color at 575 nm. This approach may have potential applications in paints, cosmetics, textile, and displays.

3.2   Strain-Responsive PDMS/SiO₂ Composites

Optical polymer nanocomposites offer synergetic functionalities by the association of organic or inorganic additive nanostructures into the polymers either in molten or solution state.[78, 79] The particulate structures are randomly dispersed over polymer volume and the optical activity of these materials is commonly based on the absorption of the incident light. The formation of colloidal crystals and filling out the vacant spaces among the colloidal particles can be an alternative approach for the structural evolution of polymer/particle composites. The challenge of this strategy is to maintain the crystalline structure of the colloids and therefore iridescent nature. With the growing knowledge of the physical fundamentals, stimuli-responsive composites that are able to detect chemical, thermal, and mechanical changes, have been used to effectively develop sensors, probes, and information displays.[80] The colorimetric response upon external stimuli may be obtained from physical phenomena including interference and diffraction of the incident light, namely structural color.[81-83]

The interference resulting from diffraction and scattering of light from nano- or microstructures with a specific wavelength, namely structural color, offers a promising route to dynamically tune the optical properties of materials in response to external stimuli without changing their bulk properties. In nature, bio-organisms switch color or transparency for adaptation to the local environment such as hiding from their predators or mating purposes.[43, 84-86] For instance, squids and octopuses in the deep sea are very talented at camouflage. They are normally transparent in the sea, and thus invisible to a predatory fish in down-welling light. Nevertheless, they can rapidly transform into red and becoming invisible again with bioluminescent searchlights according to circumstances.[87]

Likewise, numerous species of chameleons have an uncanny ability to rapidly tune their colors between camouflage and visible states according to the situation, including in male to male combats and courtship.[88] Since their skins consist of dermal photonic crystals, they are able to generate colors through the reflection of visible light. As the lattice spacing of the photonic crystals governs the wavelength of reflection, the color can be controlled by squeezing/releasing the skin.[89] From this point of view, the bio-inspired structural color tuning by external stimuli has become prominent for optical and sensing applications.[90-94] Motivated by examples of nature, synthetic materials that have structural periodicity over long range can be used to mimic these structures. Colloidal assemblies have been employed to provide strain-induced color change for various applications. For instance, strain or pressure can be estimated in a colorimetric manner by mechanochromic films[95, 96] and fingerprints can be readily recognized by analyzing color pattern.[97] In addition, lasing from fluorescent molecules in the photonic structures can be modulated by strain-induced adjustment of the stop band position.[98] Through a local modulation of the elastic modulus, the color pattern can be encrypted; the hidden pattern is disclosed while the films are subjected to extensional stress.[99, 100]

In this part, SiO_2 colloidal particles having five different diameters were synthesized using the Stöber method. The photonic films of SiO_2 and their strain responsive polymer composites were obtained. Colloids were applied to PMMA substrates by using the spraying process. The obtained photonic films having structural color were characterized in terms of a relation between morphology and optical features. For polymer photonic nanocomposites, particles were merged to PDMS matrix. The optical characteristics under external stress were monitored and discussed.

3.2.1. Preparing the PDMS/SiO_2 Composites

The SiO_2 colloidal particles were synthesized by Stöber method and particle size was controlled using the aforementioned strategy, namely TEOS concentration. The colloids were centrifuged to remove unreacted reagent. The desired amount of collected particles were re-dispersed in EtOH, isopropyl alcohol (IPA), and water, respectively. The PDMS/SiO_2 composites were prepared as shown in Figure 3.8. The colloidal dispersions of SiO_2 were sprayed onto black PMMA substrates to obtain photonic films. The PDMS precursor (Sylgard 184) with 10% w/w crosslinker was drop-casted onto resulting films. Subsequently, the samples were allowed to stand in a vacuum (200 mbar) to eliminate air

bubbles and cured at 60 °C for 4 h. The rigid composite structures were then carefully peeled off from the substrate.
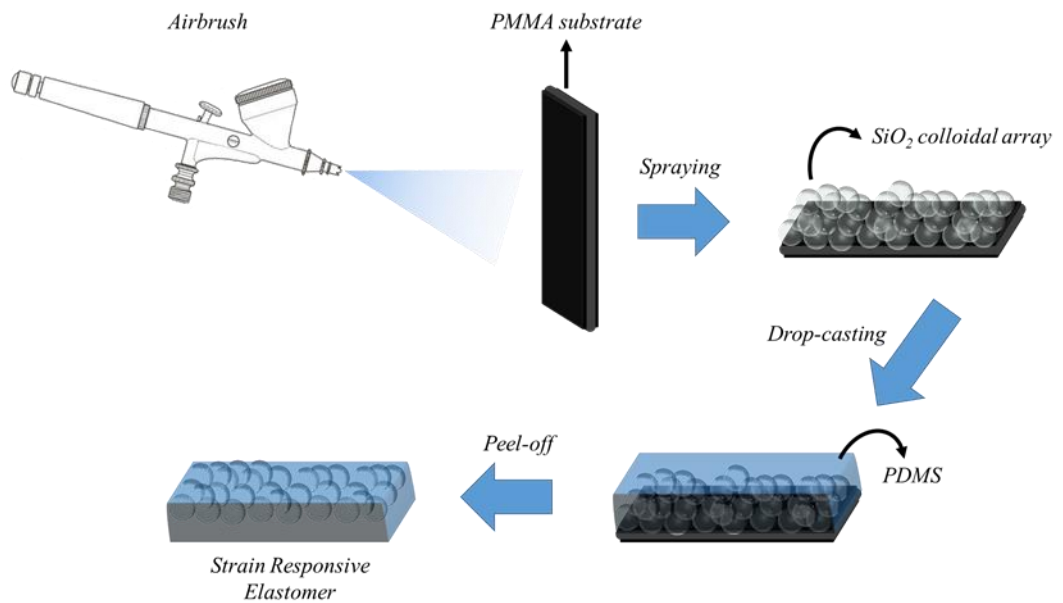
Figure 3.8. Schematic representation of strain responsive elastomer preparation.

3.2.2. Results and Discussion

The image of SiO₂ particles was taken by using SEM, presented in Figure 3.9. All synthesized particles have a spherical shape and various diameter. The desired size of particles was achieved by using a different amount of solvent (EtOH) during the synthesis. As mentioned in our previous study,[11] TEOS volume and particle size have a proportional relation.

Particle size was determined by using both DLS and SEM images (Figure 3.10). To the best of our knowledge, the DLS method gives the hydrodynamic radius of the particles; whereas, image processing provides the results from dry content. Hence, size distributions have a negligible difference. It is concluded that both distributions are uniform sized and their polydispersity index (PDI) between 1% and 6%, which is defined as monodisperse. Five different size distributions were obtained, which were 160, 198, 210, 253, and 298 nm.

3.2.2.1. Spraying Application

Spraying application was carried out by using airbrush system, which is connected to motor pump. To fabricate structural colored films, colloidal dispersion (50 µL, 10% w/v)
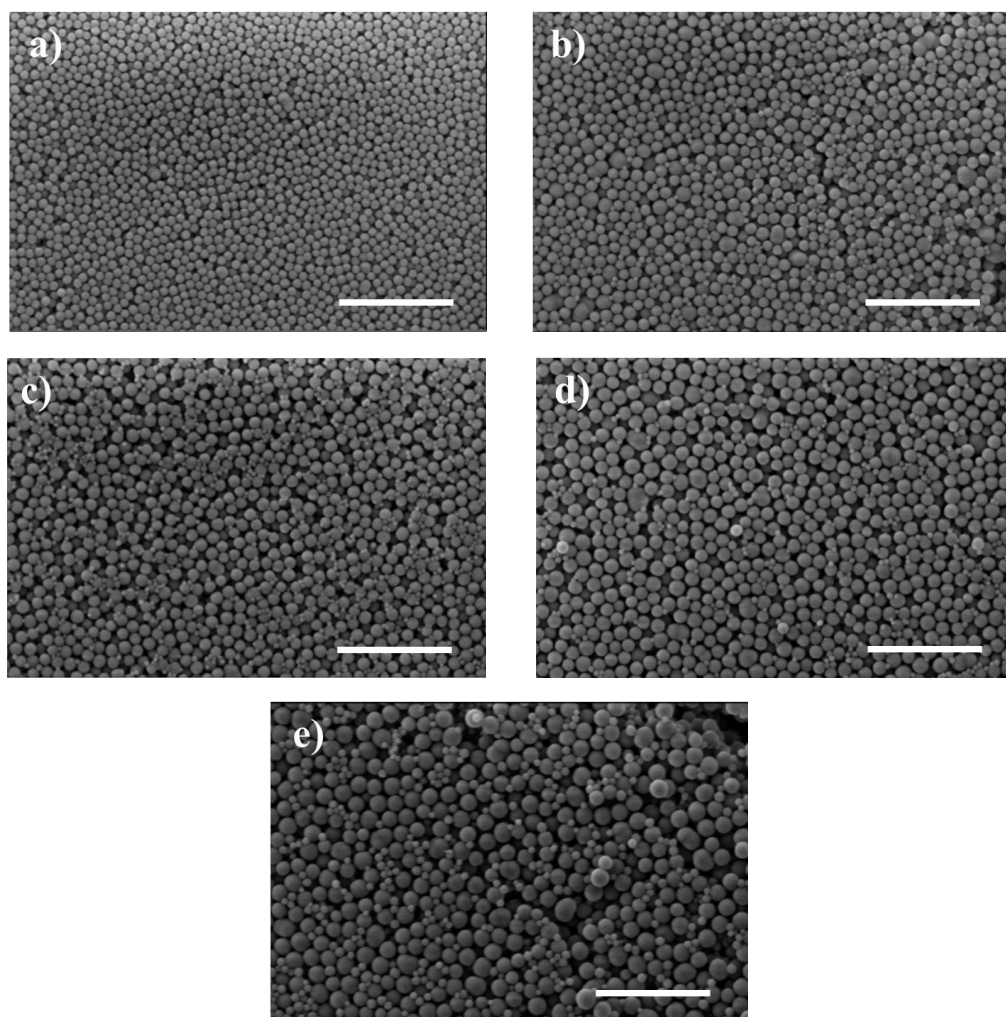
Figure 3.9. SEM images of SiO$_2$ colloidal particles having various diameter. Scale bars refer to 2 µm.
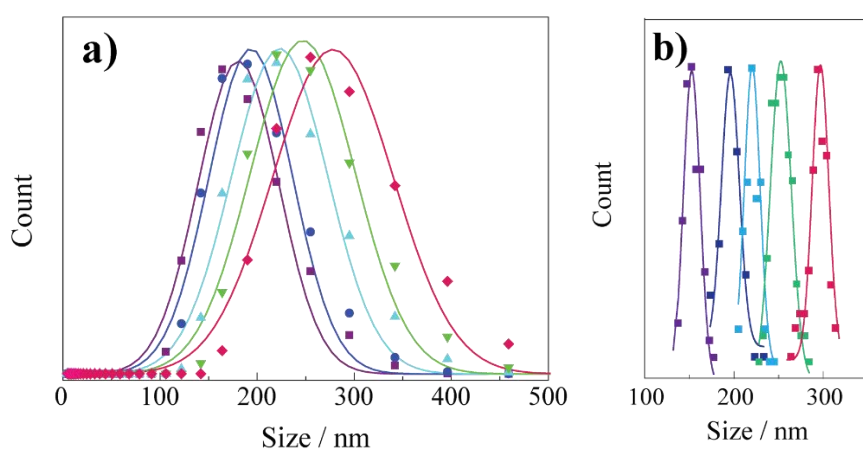
Figure 3.10. Size distribution of the particles ((a) DLS, (b) SEM).

was loaded to the system and sprayed onto the PMMA substrate having 2×5 cm^2 dimension. The colloid was sprayed from approximately 10 cm distance until the particles homogenously spread out to surface. During the process, different liquids (IPA, EtOH,

24

and water) were employed to system and their effect on color saturation was examined, respectively. In Figure 3.11a, the appearance of photonic films, prepared by using equivolume IPA, EtOH, and water, are presented. Among these films, the palest one is prepared by using water, while the others exhibit relatively brighter blue color. Corresponding reflection spectra of the photonic films (Figure 3.11b) verify the aforementioned observation. In reflection spectra, color saturation can be estimated from the ratio between significant signal and baseline. Hence, even if reflection signal at ~390 nm is higher for the photonic film that is prepared by using water, it appears light blue due to higher baseline. On the other hand, saturation of the photonic films prepared by using alcoholic dispersion is significantly higher, and only a slight difference between these films. The CIE 1931 chromaticity diagram is shown in Figure 3.11c according to reflection spectra. According to observation, the color of the waterborne photonic film is given almost in the middle of the diagram, where the others are in the blue region.
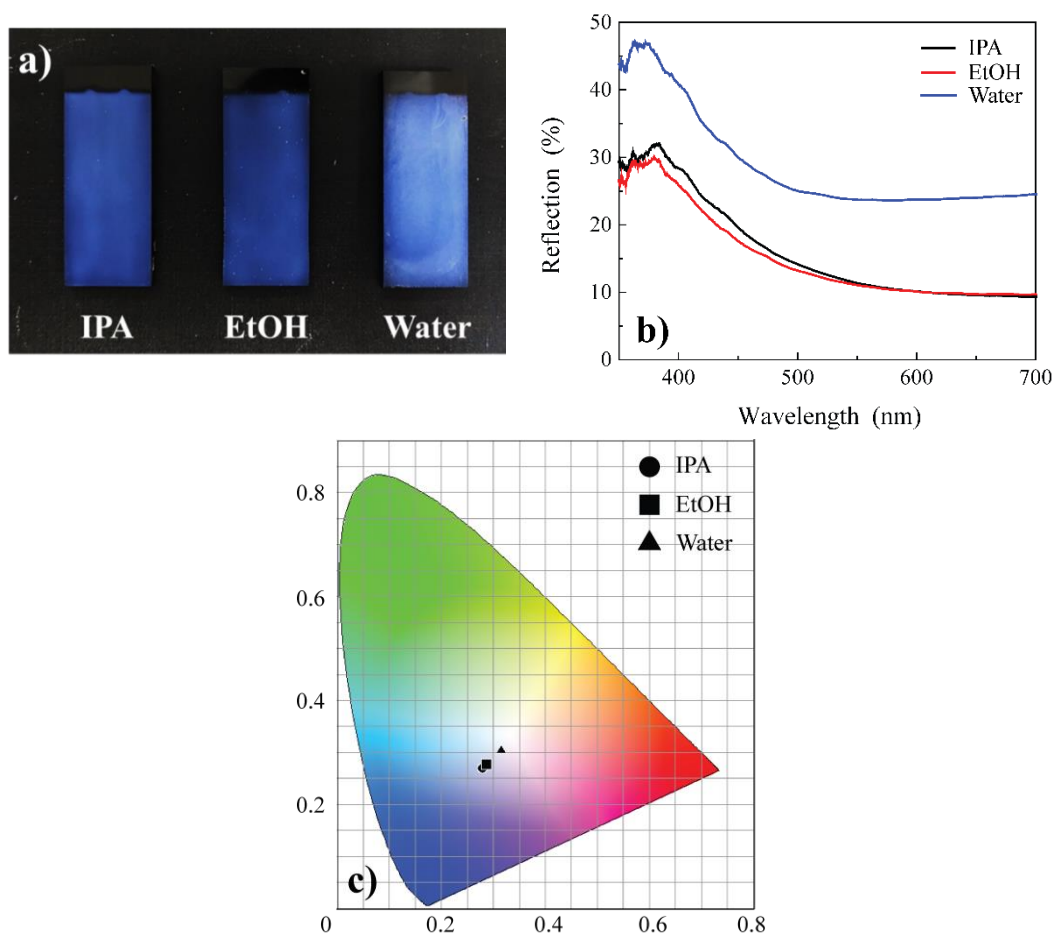
Figure 3.11. (a) Appearance of photonic films prepared by using various dispersants. (b) Reflection spectra and (c) CIE color coordinates of corresponding films.

The underlying mechanism of this color saturation depending on colloidal dispersion is the interaction between substrate and dispersant. In other words, the contact angle is a key parameter for the color saturation of the photonic films. For a robust color generation, the order of building blocks (in this case SiO_2 particles) provides more coherent scattering from the nanostructure. Therefore, different degree of order is observed by evaporation of micro droplets having various contact angles onto the substrate. In Figure 3.12, optical microscopy images of photonic films prepared by using IPA, EtOH, and water are presented. The films obtained by spraying IPA and EtOH exhibit uniform distribution, where the water-borne film contains heterogeneous colloidal particle mounds. In the spraying process, the chemistry of the substrate was chosen as PMMA, which has hydrophobic nature. According to literature, colloidal dispersion having contact angle below ~30° is appropriate for forming ordered nanostructures, while above this limit,
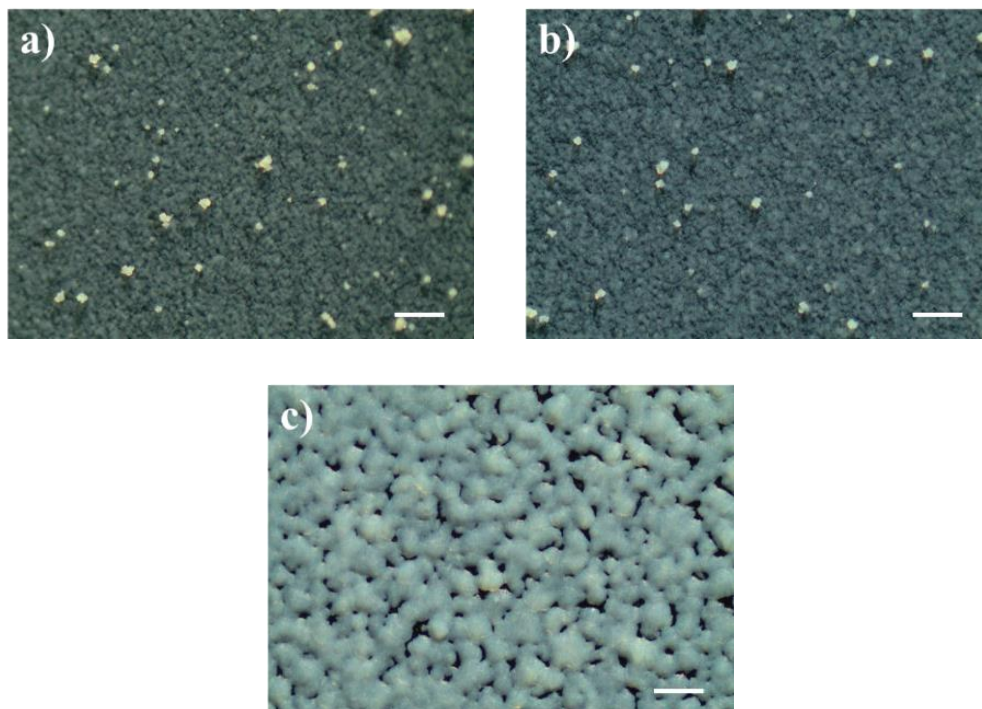
Figure 3.12. Optical microscope images of colloidal arrays that are sprayed by using various dispersants ((a) IPA, (b) EtOH, and (c) water). Scale bars refer to 200 µm.

particles accumulate at the edge of the droplet due to convection flow. On the other hand, *Takeoka et al.* state that for above 90°, convection flow heads to the center of the droplet during the evaporation, which provides order though not as much as at lower magnitudes. In this context, EtOH and IPA have organic chains that provide better wettability on a PMMA substrate. Hence, the order of particles and color saturation are higher than their

water-borne counterpart. Color saturation difference between the films prepared by using IPA and EtOH can be explained in terms of evaporation time. The orientation of the nanostructure not only depends to contact angle but also is related with the vapor pressure of the dispersants, if even has relatively minor influence. In the case of IPA and EtOH, their enthalpy of vaporization values can be found as 44 and 38.6 kJ.mol^{-1} using the Clausius-Clapeyron Equation.[101] Therefore, evaporation of the alcohol having longer chain takes more time than the other, which may provide more homogenous film.

SEM images of thin films prepared by different dispersants are represented in Figure 3.13. In both films prepared by alcohol, evaporation leaves a number of circular patterns behind due to convection flow. Nevertheless, the accumulation is achieved not only circular but also along the surface due to the low contact angle. For EtOH, spreading of the particles onto the surface is observed more sparsely due to faster vaporization. Therefore, a number of well-arranged particles are relatively low compared to the counterpart prepared by using IPA. Not surprisingly, it affects color saturation. On the other hand, aggregates are clearly observed for water-borne film due to aforementioned contact angle issue.
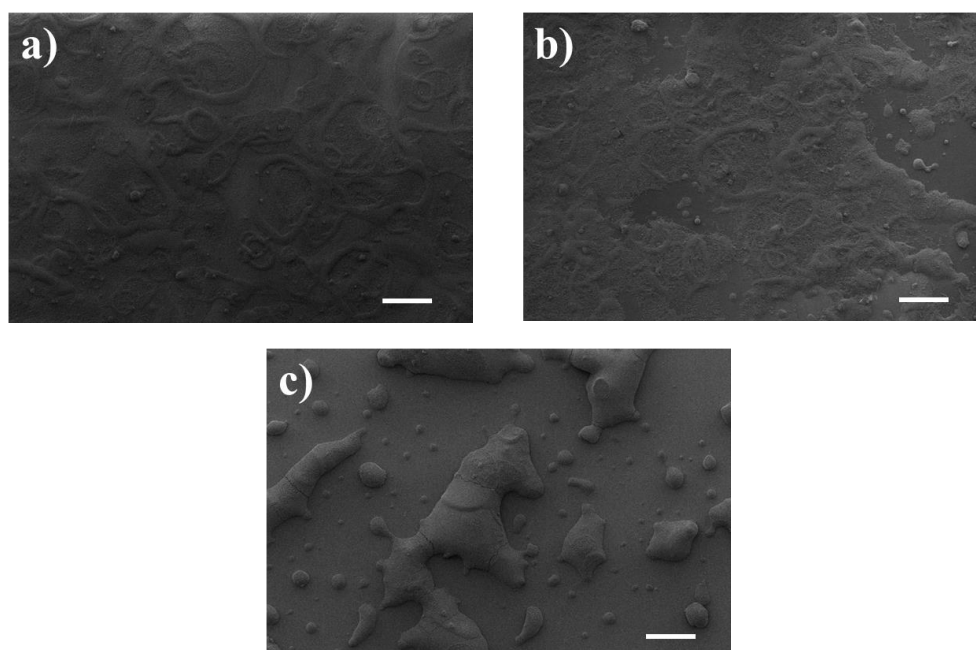
Figure 3.13. SEM images of colloidal arrays sprayed by using various dispersants ((a) IPA, (b) EtOH, and (c) water). Scale bars refer to 20 µm.

3.2.2.2. Quasi Arranged Photonic Films

For further spraying process, IPA was assigned as a dispersant of colloidal SiO$_2$ particles having a diameter in the range of 160 to 298 nm. The concentration of the colloidal

solution was kept at 10% (w/w), while an aliquot of 50 µL dispersion was sprayed onto black PMMA substrates. In Figure 3.14a, the photograph of photonic films having various colors due to the different size of colloidal particles is represented. According to Bragg-Snell equation, the wavelength of coherently scattered light is directly related to the size of the building blocks of the periodic nanostructure. Therefore, colors unsurprisingly emerge different from each other. Corresponding reflection spectra is given in Figure 3.14b.
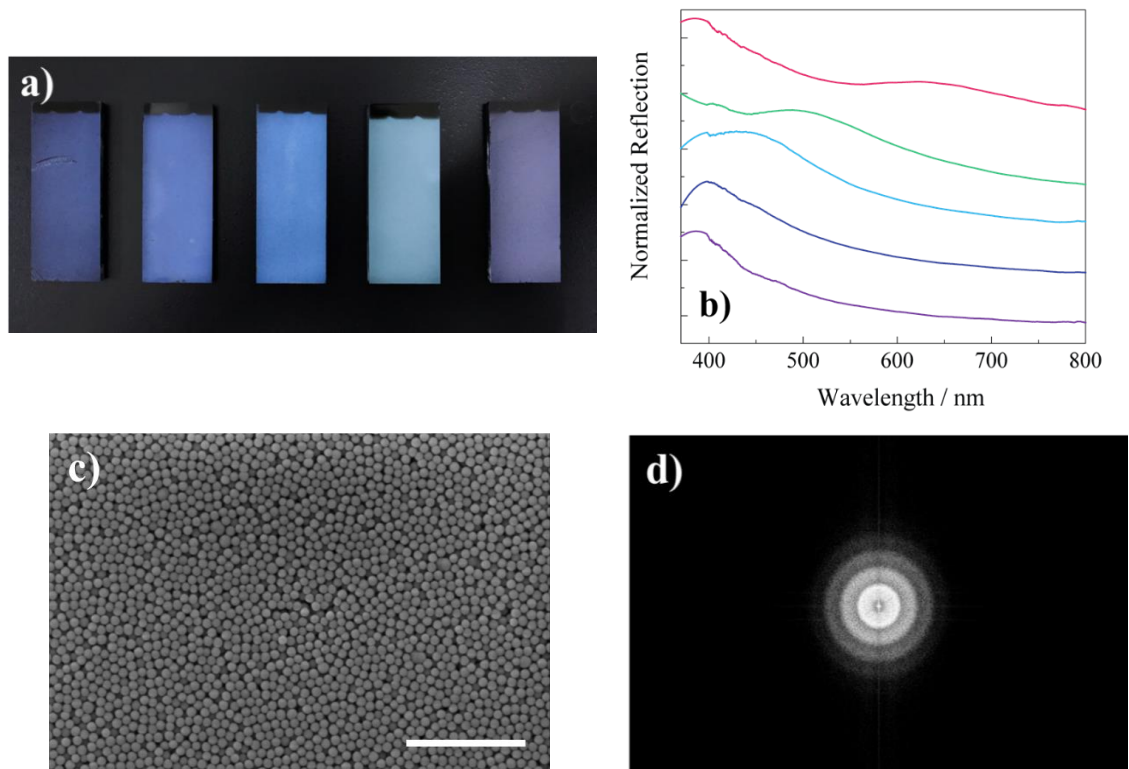
Figure 3.14. (a) Appearance and (b) reflection spectra of photonic films having different particle size. (c) SEM image, and (d) corresponding FFT power spectrum of photonic glass consisting of the particles having diameter of 160 nm. Scale

With increasing particle size, reflection wavelength shifts from 390 to 620 nm, where the color changes from violet to magenta. In larger particle size, color arises from mixing of two reflection signals (for magenta: 400 and 620 nm), which belong to coherent scattering (longer one) and single particle resonance (shorter one). In representative SEM image (Figure 3.14c) of photonic film forming the particle 160 nm in diameter, order of building blocks are observed as amorphous. FFT is run through this SEM image using ImageJ software to unambiguously examine the order of structure. Circular shapes in FFT image (Figure 3.14d) verify that there is no long-range ordered domain.

3.2.2.3. Strain Responsive Photonic Elastomers

The fabrication of the strain responsive elastomer films is formerly illustrated in Figure 3.8. First, the SiO_2 colloidal dispersion was spray-coated onto a Plexiglass substrate following the procedure reported earlier to obtain angle-independent color coatings from quasi-arranged arrays. Here, angle-independent blue and green films, which were obtained from SiO_2 colloidal particles with diameters of 210 and 253 nm were readily obtained. According to the aforementioned description, the particle array has local spaces, which can allow the penetration of oligomeric resin. An aliquot of PDMS precursor solution (Sylgard® 184; 700 µL) was then cast over the photonic films, filling the voids between the particles. The composite films were cured at 60 °C and 250 mbar for 4 h. Subsequently, they were carefully peeled off from the substrate to avoid serious deformation such as microcrack, rupture, or scratch. Since the refractive index of PDMS
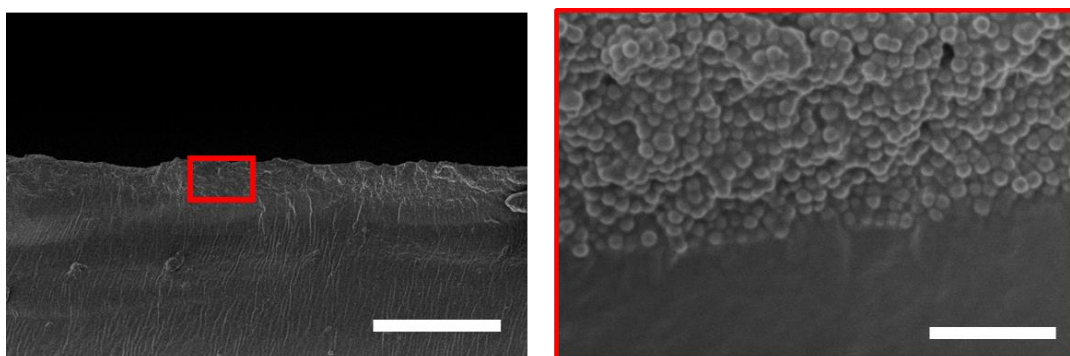
Figure 3.15. Cross-sectional SEM image of strain responsive elastomer nano composite at various magnification. (Scale bar: (a) 20 µm and (b) 2 µm)

(1.425 at 632.8 nm)[102] is very close to that of SiO_2 (1.457 at 632.8 nm),[103] the composite films were unsurprisingly transparent in the visible region. Therefore, it is difficult to recognize the unstrained PDMS films with and without embedded colloidal SiO_2 particles.

In Figure 3.15, it is seen that the elastomers have two layers, which are a thin layer of hard PDMS/SiO_2 composite (~6 µm thick, represented in inset) and a bulk layer of pure PDMS. The thickness of the pure PDMS layer ranged from 0.5-0.7 mm depending on conditions in casting. The quasi-arranged structure of spray-coated NP films possessed random distribution, thus larger pores allow to infiltrate PDMS. Furthermore, the resulting thicker PDMS layers between the SiO_2 particles offer higher mechanical strength against macroscopic rupture, hence the use of quasi-arranged systems are preferred rather than ordered ones (crystals) for casting of macromolecules on photonic
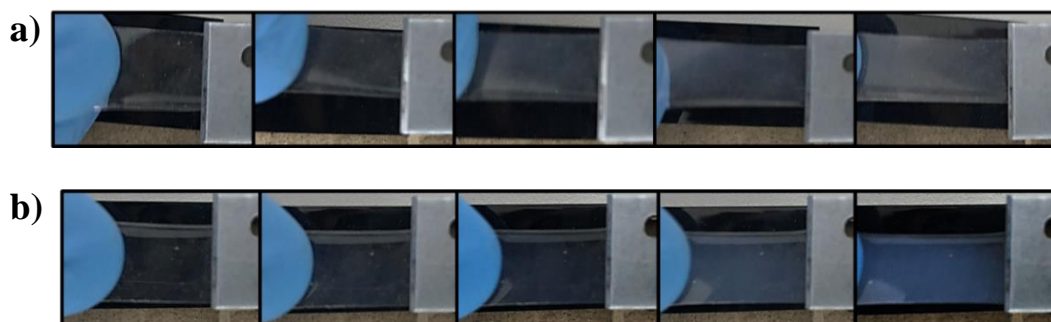
Figure 3.16. Frames of the appearance of PDMS/SiO$_2$ elastomers with the particle diameters of (a) 200 nm and (b) 250 nm at various strain rate.

nanostructures. Upon stretching, two optical phenomena were observed: i) switching from transparency to opacity (Figure 3.16a) and ii) appearance of the uniform, angle-independent reflective blue color (Figure 3.16b). By naked eyes, transparent as-prepared PDMS/SiO$_2$ film began to appear translucent at about 20% strain, subsequently, it transforms to completely opaque above 60%.

In both elastomer having different sized SiO$_2$, baseline rises with increasing strain level (Figure 3.17a and b). Reflection signals start to arise at 10% strain and intensified at 40%
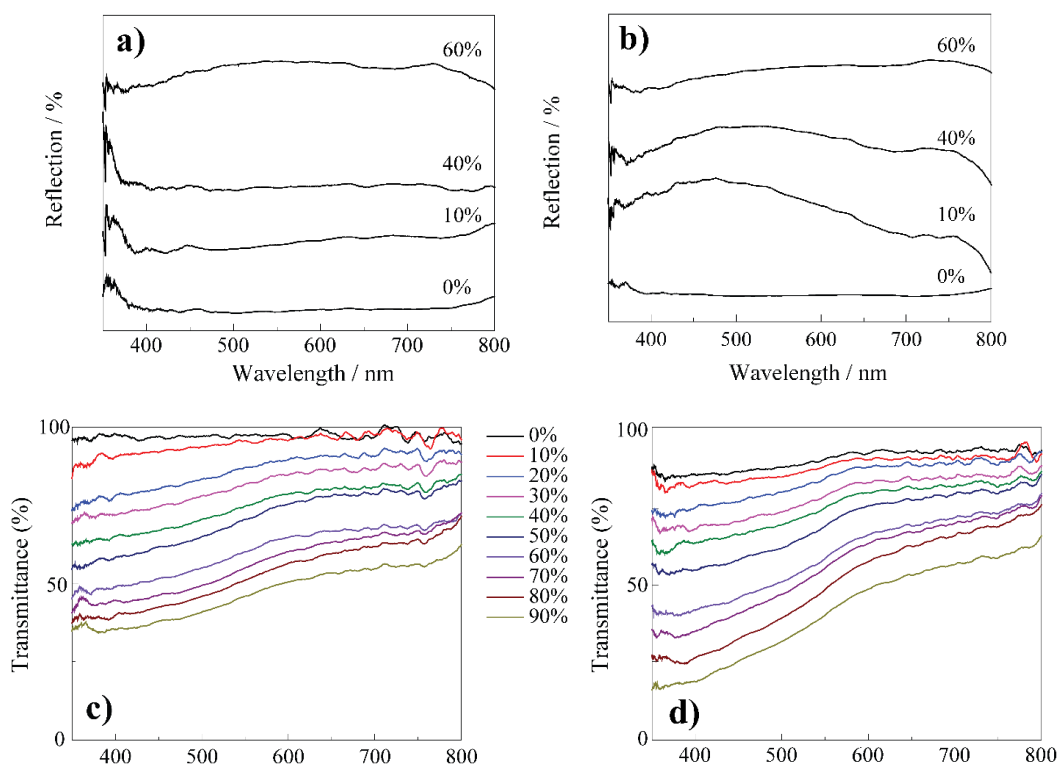
Figure 3.17. (a, b) Reflection and (c, d) transmission spectra of strain responsive elastomers by forming SiO$_2$ (a, c) 200 nm and (b, d) 250 nm in diameter.

strain. The peak position change with increasing strain is negligible. The reflectance peak of cyan color (SiO_2 diameter: 250 nm) is observed at 490 nm. Nevertheless, color saturation is lost in higher strain levels. On the other hand, strain-dependent transmission measurements (Figure 3.17c and d) show that their transmission dramatically decreases with increasing strain level for both PDMS/SiO_2 elastomer. At the beginning, the
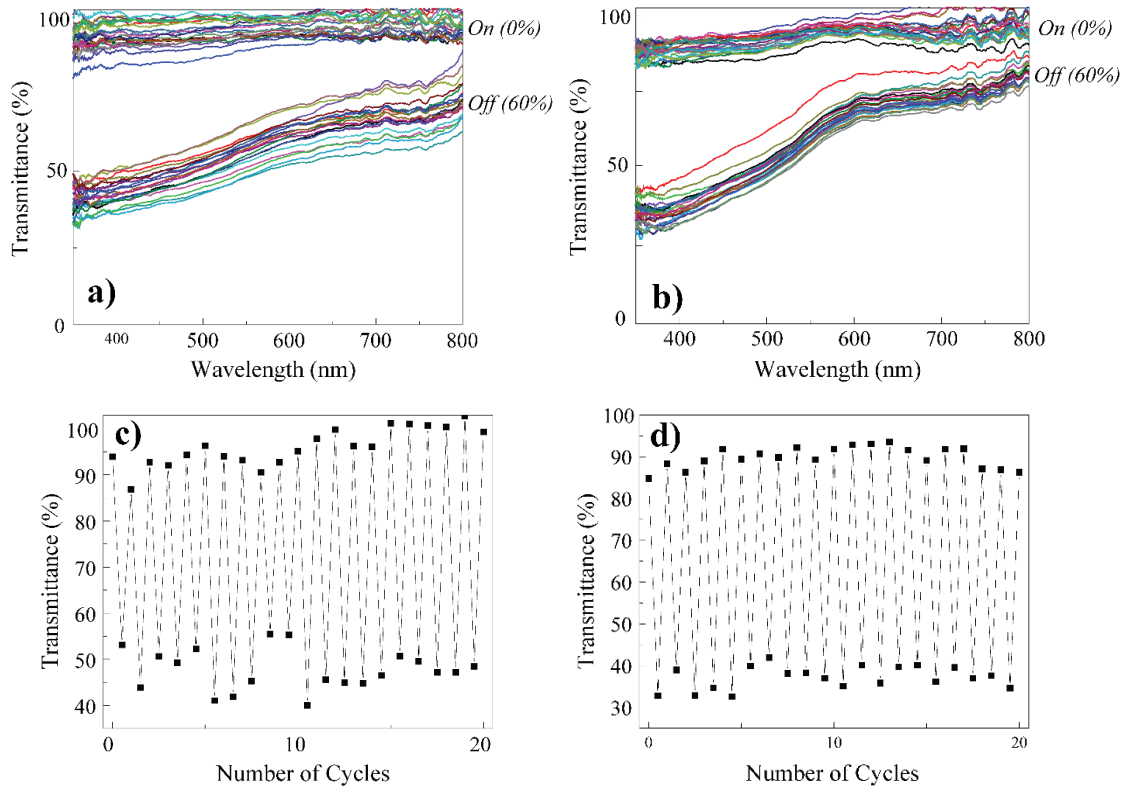
Figure 3.18. Transmission spectra of strain responsive PDMS/SiO_2 elastomers (a: 200 nm, b: 250 nm) as unstrained and strained (60%) for 20 cycles and (c and d) their intensity at 450 nm wavelength for each cycle.

transmission rate is approximately 90-95%, where the strain level is 0%. For PDMS/SiO_2 elastomer having 200 nm particles, transmission spectrum uniformly decreases to 35% at 90% strain. In the case of elastomer having greater sized particles, transmission decreases non-uniformly as expected due to its reflective color. Hence, with increasing strain level, transmission decreases more dramatically at 400 nm.

To demonstrate repeatability and robustness of strain-responsive elastomer, the films were stretched and released from 0% to 60% strain for 20 times, and the transparency was measured continuously. The transmittance of the films after stretching and releasing 20 times was nearly identical to that of the unstretched film, while they exhibit almost same transparency at 60% strain for each cycle (Figure 3.18a and b). Their transparency levels

at 450 nm are also represented in Figure 3.18c and d for each cycle (0% - 60%). Both films show an efficient and repeatable on-off process under external stress. It is thought that the durability and stability of the films can be attributed to the dual structure of the elastomer, which are thick PDMS layer and the thin PDMS/SiO$_2$ composite layer. While the top thin layer is responsible for color/transmittance change, the bottom thick PDMS layer produces necessary restoring force for the entire film for repeated stretching and release.

To investigate the origin of this phenomenon, which has reported in the literature, optical microscopy was employed to PDMS/SiO$_2$ films stretched at various strains. As seen from optical microscope images (Figure 3.19), microcracks begin to appear in the formally undeformed surface, while the strain level increases (Figure 3.19a and b). With further increase of strain, the number and length of microcracks enlarge and wrinklings appear that are transverse to the applied strain (Figure 3.19c and d). The wrinkle formation can be explained by the mismatch of mechanical properties of the two-phase nature of the composite film. While the stress is removed on the elastomer, microcracks leave behind irreversible deformation that appears in line-shaped crack having perpendicular alignment to stress axis (Figure 3.19e).
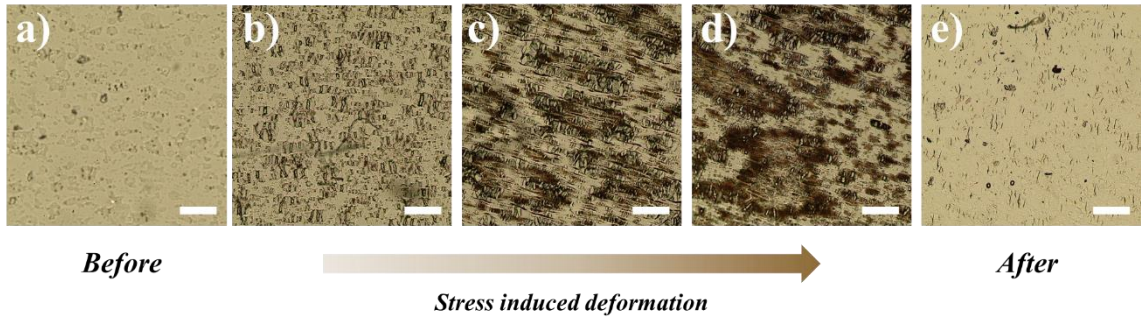
Figure 3.19. Optical microscopy images from the surface of PDMS/SiO$_2$ elastomer during stretching cycle. Scale bars refer to 200 µm.

The volume fraction of void (ϕ_{void}) can be estimated based on the model schematically shown in Figure 3.20a. Here, the void is assumed as a perfect ellipsoid and a SiO$_2$ particle is embedded in the void. So the volume of void is

$$V_{void} = \frac{4}{3}\pi a r^2 - \frac{4}{3}\pi r^3 = \frac{(a-r)}{r}V_{SiO2} \qquad (3.4)$$

$$\phi_{void} = \frac{V_{void}}{V_{void} + V_{SiO2} + V_{PDMS}} \qquad (3.5)$$

The SiO$_2$ particles are nearly close-packed, so the edge PDMS thickness is very small compared to the particle diameter. Here the thickness is ignored, the strain is *ε= (a-r)/r* and V_{PDMS}:V_{SiO2} = 0.65:0.35. Therefore,

$$\phi_{void} = \frac{0.65\varepsilon}{0.65\varepsilon + 1} \tag{3.6}$$

According to Equation 3.6, *ε-ϕ$_{void}$* curve is given in Figure 3.20b. For the particle having 200 nm average diameter, threshold volume fraction (ϕ_{th}) is approximately 0.35 to provide coherent scattering.[10, 104] Based on this knowledge, structural color generation is possible if the strain level exceeds 80%. However, cyan color is experimentally observed
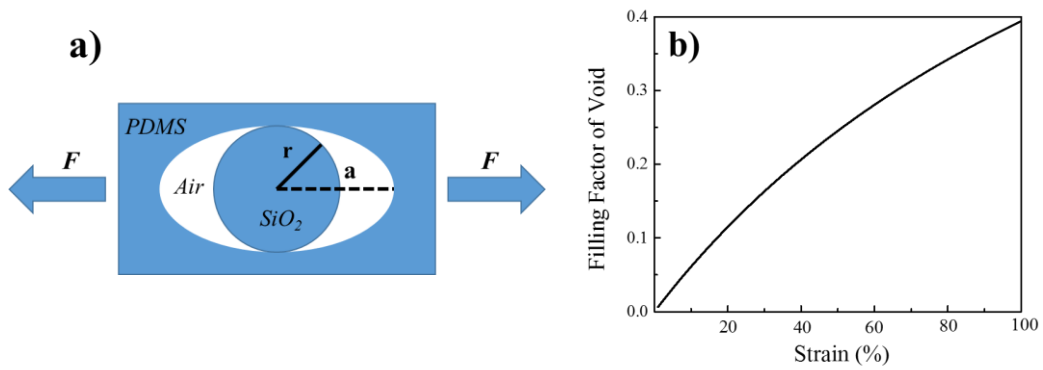
Figure 3.20. (a) Schematic representation of existing voids at PDMS/SiO$_2$ interface and (b) relation between volume fraction and strain (Source: Ge et al., 2015).[20]

at between 10-40% strains. The underlying reason for this theoretical and experimental conflict is stress distribution on the material. In other words, the local strain on PDMS/SiO$_2$ domains already exceeds the threshold level, where the total strain is relatively lower.

3.2.3. Conclusions

In summary, strain responsive PDMS/SiO$_2$ elastomers having bilayer were obtained successfully. Their transmission and reflection characteristics at various strain levels show that the material design concept can be useful in mechanical sensor applications. On the other hand, the robust and repeatable properties can be applied to the other materials that are sensitive to heat, light, or humidity.

CHAPTER 4

COLORIMETRIC AND SELF-HEALABLE PRESSURE SENSORS: A SMART PHONE-ASSISTED DETECTION

Colloidal NPs have attracted intensive research interest not only owing to their size- and shape-dependent features but also the development of novel and unique properties through their collective effects such as interparticle coupling and structural ordering.[11, 105, 106] Hence, the controllable geometry and properties depending on the assemble behavior make them promising candidates for wide range of applications from stimuli-responsive smart materials to sensors.[13, 20, 107] Gold nanoparticles (Au NPs) appear to be a good example for this group of materials since they have optical properties distinct from analogous atomic or bulk counterparts. Upon illumination with incident electromagnetic beam, the free electrons are confined and exhibit collective oscillation that leads to absorption of visible light. This phenomenon is termed as localized surface plasmon resonance (LSPR).[108]

For colorimetric sensors that give optical response according to the measurand, there are various strategies based on color change. A dramatic colorimetric change upon the aggregation of Au NPs is one of the well-known systems among others.[109-111] The particles can be assembled or disassembled either by varying ionic strength or by changing pressure so that LSPR coupling-induced responsive color may switch from red to blue, or vice versa.[112] The sensing strategy based on the change of LSPR properties of Au NPs can be designed to detect the presence of external conditions, and even more, their magnitude can be estimated. This strategy allows performing a wide variety of functions such as chemical and biochemical sensing,[113, 114] pH,[112, 115] strain,[13, 107] temperature,[116, 117] and photosensing.[118-120] Furthermore, upon the removal of existing stimuli, the system may relax back to the initial state. Therefore, the reversible characteristics of plasmonic nanoparticle-based colorimetric sensors offer the potential of

improved specificity and long-term availability as one can use the sustained stimulus-response function in diverse precision for measurement.

Among LSPR-based sensors, strain sensors are promising materials, in which viscous flow of polymeric materials during deformation leads to the shift in plasmonic band via disassembly of Au NP aggregates.[13, 121, 122] Mechanical and chemical properties of the polymers that are used as a matrix for colorimetric strain sensors are vital since the motion of Au NPs is either facilitated or prohibited. The former feature determines the reversibility of sensor depending on the elasticity of the polymer while the latter one is responsible from the interaction of the polymer macromolecules with the Au NPs surface, which is able to enhance the disassembly rate of these nanoparticles. Polyacrylamide (PAAm) and its derivatives are appropriate to use in these type sensors due to their viscoelastic properties,[123] heteroatomic structure,[124, 125] and biocompatibility.[126]

In this study, Au NP embedded PAAm composite films were fabricated and their performance as a colorimetric pressure sensor was studied. The shift in the plasmonic signal, therefore color from blue to red due to the disassembly was recorded as a function of applied force, time, and temperature (Figure 4.1.). The resulting responses against external mechanical force were correlated with the morphological change of both nanoparticles and polymer matrix, i.e. disassembly of Au NPs and crystallinity of PAAm. In addition, a simple algorithm based on the RGB values of the pixels referring to capture images through a digital camera was presented for the design of possible pressure measuring smart-phone application.
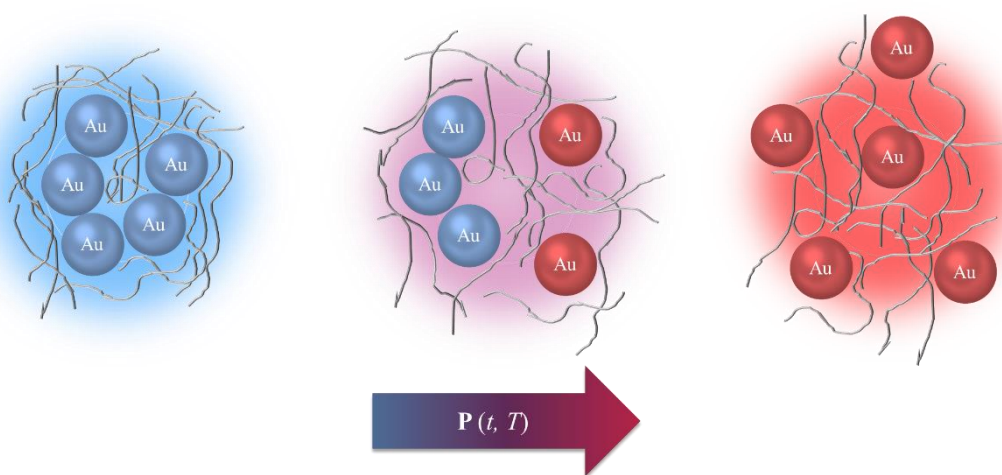
Figure 4.1. Schematic illustration of color changing of PAAm/Au films during deformation.

4.1. Materials and Methods

Tetrachloroauric (III) acid trihydrate (HAuCl$_4$.3H$_2$O, 99%), trisodium citrate dihydrate (≥99%), PAAm solution (50% w/v, M$_w$: 1500 g/mol), and poly(vinyl pyrrolidone) (PVP; M$_w$: 10 kg/mol) were purchased from Sigma-Aldrich. All chemicals were used as received without any further purification. The deionized water (18.2 MΩ•cm^{-1} at 25 °C) used in all experiments was produced by a Milli-Q Advantage water treatment system.

4.1.1. Preparation of Au NP / PAAm Composites

The synthesis of Au NPs was carried out via reduction of HAuCl$_4$. This procedure was reported by *Turkevich et al.* [127] In a typical synthesis, an aqueous solution of HAuCl$_4$ (0.24 mM, 200 mL) was loaded one-necked flask and heated up to reflux with magnetic stirring. Subsequently, trisodium citrate solution (0.34 M, 1 mL) was added to system. The solution was allowed to reflux for 30 min, while its color changed from pale yellow to ruby red. Final mixture was centrifuged (6000 rpm, 1 h) and re-dispersed in 2 mL water.

PVP solution (10 µL of 1.66 mg/mL) was added to Au NP dispersion (0.5 mL) to stabilize the colloids. The PAAm solution (250 µL) was added to mixture and mixed for 5 min to obtain homogeneous blue dispersion. The mixture was then drop-casted into mold and placed in oven for 2 h at 60 °C to allow the evaporation of water. The resulting composites were cut into small pieces with 1 mm diameter.

4.2. Results and Discussion

4.2.1. Characterization of Au NPs
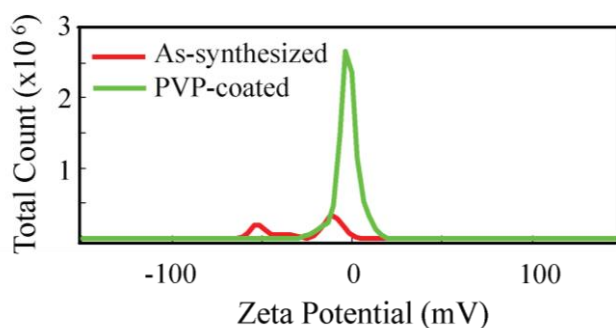
Figure 4.2. Zeta-potential distribution of as-synthesized and PVP coated Au NPs.

Au NPs were obtained by reduction of HAuCl$_4$ salts. The particles intrinsically have a negative surface charge; however, upon the incorporation of PVP, the overall charge gets

zero and they show neutral character (Figure 4.2). PVP acts as a stabilizer for the particles and sterically-stabilizes the individual particles, as a result, prevents aggregation. The dispersion containing individual particles has a deep red color. When PAAm is introduced into the system, the pH of the dispersion changes from 6.8 to 5.9. Since there is an only a trace amount of PVP (16.6 µg in entire volume) incorporated to the mixture, citrate molecules still exist onto Au NP surface. Therefore, citrate molecules are protonated with
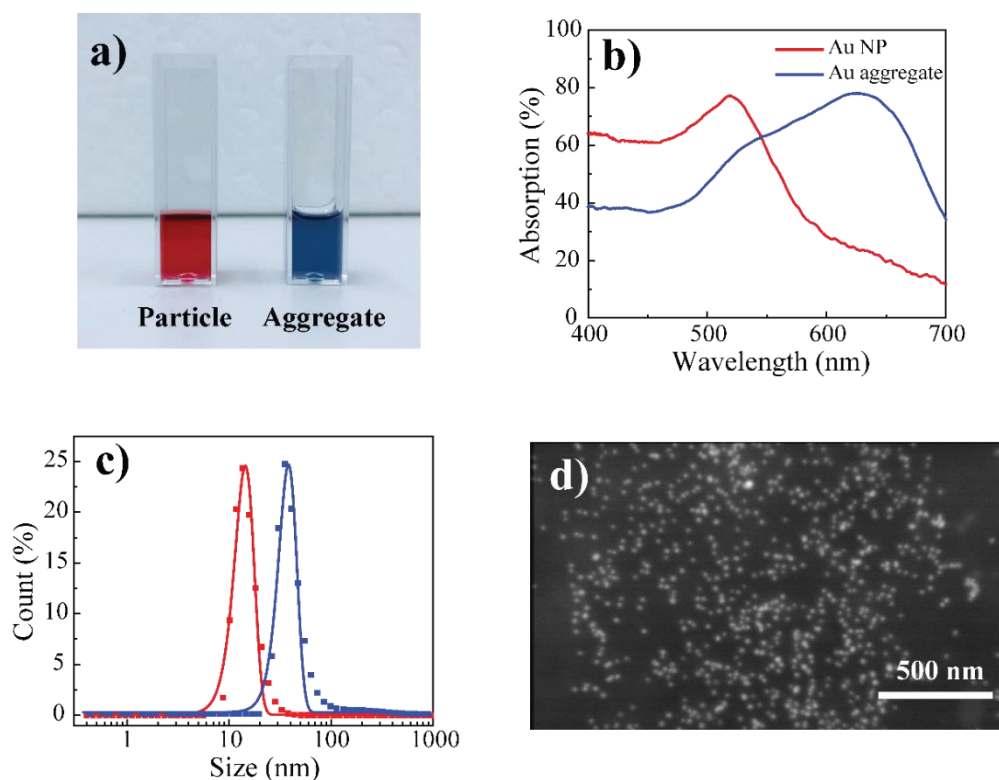
Figure 4.3. (a) Photographic images of Au dispersion appearing in red (individual nanoparticles) and blue color (aggregates), (b) absorption spectra, and (c) size distribution of as-synthesized individual Au NP and aggregate dispersions. (d) SEM image of the Au NPs.

decreasing pH and can detach from the particle surface. Removal of citrate leads to a reduction of stability, thus aggregation of the particles. Figure 4.3a shows a photographic image of the Au NP containing dispersions. The left image presents PVP-stabilized individual particles appearing in red. On the other hand, the right one illustrates the saturated blue appearance of the particles in aggregated form. The UV-Vis absorption spectra of the particles are given in Figure 4.3b. The spectrum of the individual particles has absorption maxima nearly at 520 nm; however, the aggregates of the particles present a broad signal giving a peak at 630 nm. The spectrum has a shoulder at 520 nm exactly

at the signal of individual particles. Since both signals appear in the blue dispersion, one can propose that both individual particles and aggregates coexist together in the blue dispersion. These two signals in UV-Vis spectra appear most probably due to LSPR and plasmon coupling, respectively. The broadening of the absorption can be attributed to the clustering and/or chain structure of the Au NPs in the dispersion. The spectroscopic results agree with the ones reported in the literature.[128] The diameter of the particles was measured by DLS and the results are presented in Figure 4.3c. The size range is scanned from several nm to 1 µm. The diameter of individual particles was 13.5 nm and this result is consistent with the size of individual particles seen in the SEM image (Figure 4.3d). On the other hand, the size of the Au aggregates in blue dispersion was 45 nm with a uniform Gaussian distribution. In contrast to the results of spectroscopy, the size distribution obtained by scattering only shows the aggregates in the dispersion. Light scattering measurement is based on the change of the scattering profile of the particle domain population in the system. Since they are in Brownian motion, the scattering profile varies depending on the size of the particles. The existence of the individual particles in the bluish mixture can be detected by spectroscopy; however, they cannot be observed in scattering profiles due to their low numbers in the particle population.

4.2.2. Pressure Measurements
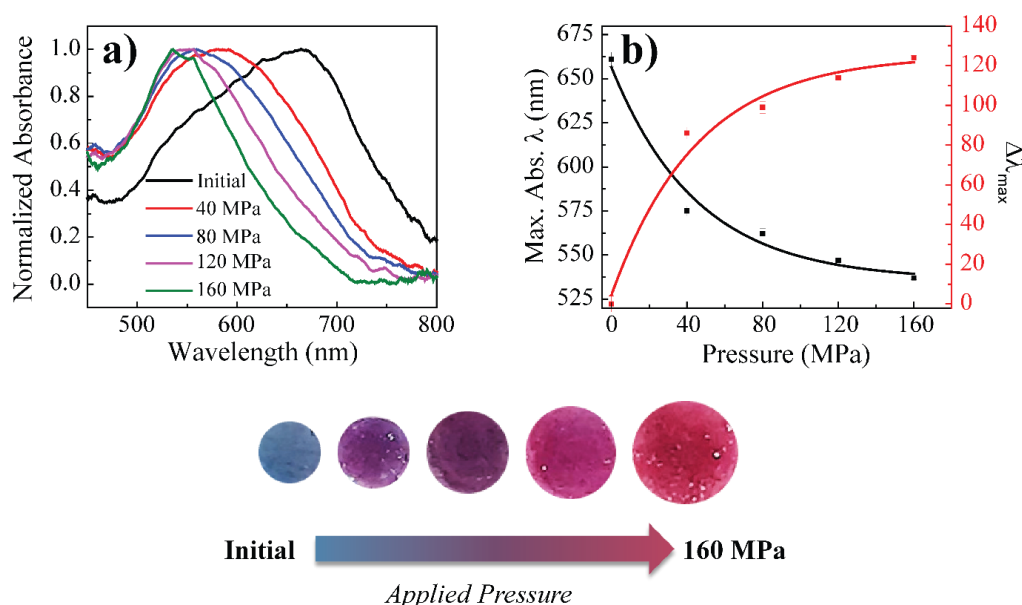
Figure 4.4. (a) Absorption spectra of the films under various magnitudes of pressure, (b) corresponding maximum absorption wavelength (λmax) and its change (Δλmax) with respect to pressure, and photographs of the films employed under various pressures.

The evaporation of water induces aggregation of the particles so that the dispersion containing Au NP aggregates shows deep blue appearance after drying. These films were cut into small pieces to perform compression tests between 40 and 160 MPa. The initial pressure applied to the composite film was calculated by dividing the force by the initial area. The application of a high pressure onto the composite film for 2 min caused a clear change in color from blue to ruby red. The change in color of the films with respect to the applied pressure is given in Figure 4.4 in terms of absorption spectra and their corresponding photographs. By means of the increase in pressure, the peak of the absorbance gradually shifts from 660 to 538 nm. Compared to the particle-water dispersion (Figure 4.1b), the absorption peak position exhibits a remarkable difference in the solid film state. For the initial state of film, peak position experiences 30 nm red shift. This may arise due to the evaporation-induced aggregation. On the other hand, the difference between individual Au NP dispersion and the compressed red film shows that complete disassembly may not be obtained, even if the most of the aggregates are separated after applying strong pressure. Since the more deformation causes a larger displacement for the Au NPs due to growing inter-particle distance, the extent of the shift in the coupling signal increases at higher pressure. It has been established that the inter-particle distance above 10 nm, plasmons cannot couple with the surface of neighboring particle.[129, 130] A morphological investigation to figure out the dispersion of the particles over PAAm volume is performed by electron microscopy. SEM images of the initial and deformed samples are demonstrated in Figure 4.5. The particles appear in large clusters
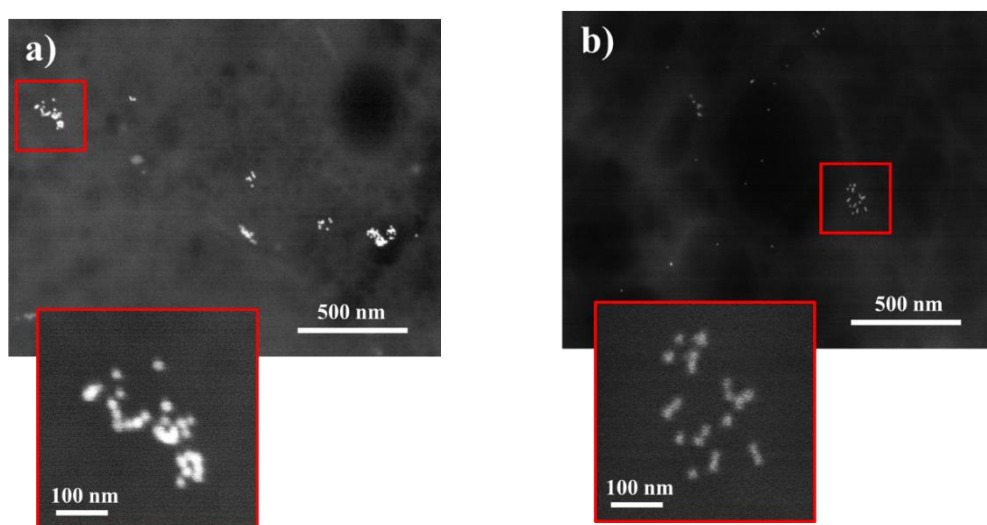
Figure 4.5. SEM images of the Au NPs in (a) unloaded and (b) loaded films.

with a diameter of about 100 nm. The aggregates in the initial state seem to be separated into individual particles as a result of deformation.

The change in color at constant pressure with respect to time was examined studying the viscoelastic properties of PAAm. In general, the Kelvin-Voigt Model allows examining the deformation of the polymer under sufficient shear stress for viscoelastic solids (Equation 4.1) (otherwise it follows Hooke's Law under lower shear stress). The deformation is proportional to change in time under constant shear stress;

$$\varepsilon(t_0) = \int_0^{t_0} \frac{\sigma(t_0)}{\eta} \, dt \tag{4.1}$$

where ε is deformation, σ is applied stress, t is time, and η is viscosity. Figure 4.6a shows absorption spectra of the film at constant pressure (40 MPa) for various time periods ($t = 0, 1, 2, 3,$ and 5 min). A clear blue shift of the absorption maxima from 575 to 552 nm is observed as the pressure time is extended from 2 to 5 min, i.e. Au NP clusters can find more time to be separated into individual particles. A similar trend of the spectral shift was observed when the magnitude of the applied pressure is varied. The maximum wavelength (λ_{max}) of the absorption versus duration of time of the applied pressure is given in Figure 4.6b. For each pressure scale, λ_{max} gradually decreases in time and saturates at approximately 538 nm. Not surprisingly, the rate of the shift gets higher under higher pressure. On the other hand, a series of change in absorption ($\Delta\lambda_{max}$) for different pressures is given as a function of the logarithmic time scale (Figure 4.6c). To provide a simple prediction for the superposition, the effect of pressure in different logarithmic time scales is simply to shift the y-axis, to the right/left without a change in the magnitude of $\Delta\lambda_{max}$.

A "time-pressure shift factor" α_P (P) can be defined as the horizontal shift that has to be applied to the curve plotted at an arbitrary pressure in order to move it to the curve at reference pressure. In our case, 40 MPa was particularly assigned as a reference curve and α_P was calculated for the other curves at different pressure scales. To obtain a single "master curve" by horizontal shifting, a simple logarithmic calculation is carried out using α_P values of each curve and the negative shift is provided (in the arrow direction). In Figure 4.6d, the calculated master curve is given as a result of the calculation. Since the curve satisfies the Boltzmann superposition principle that describes the response of a
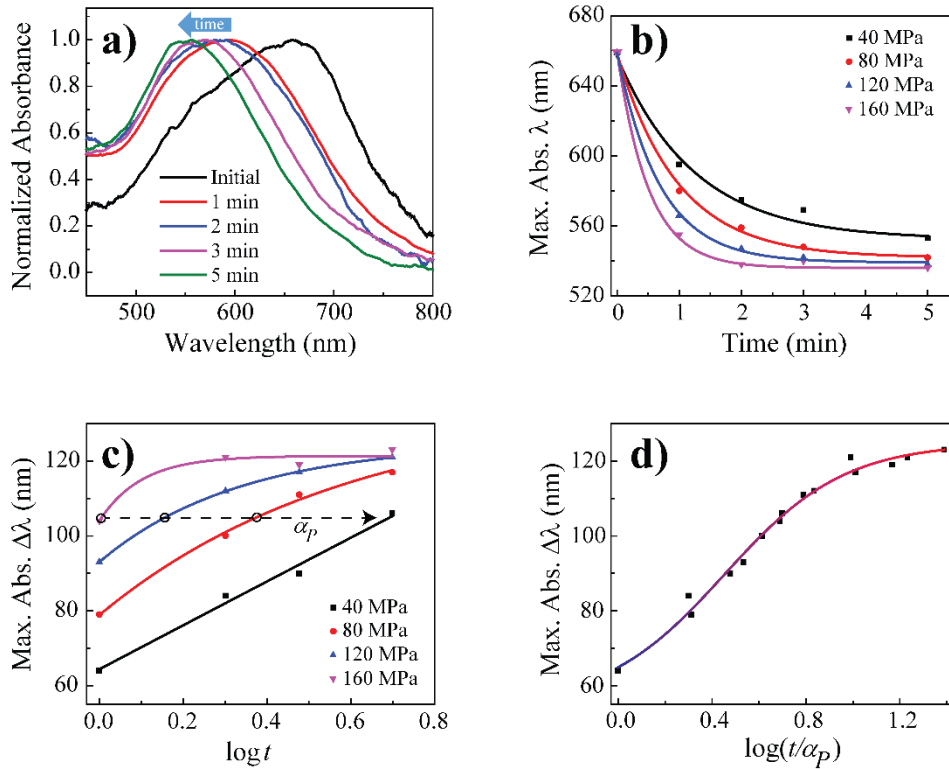
Figure 4.6. (a) Absorption spectra of the pressure (40 MPa) applied film for the different duration, (b) the change of the corresponding λmax with respect to time, and (c) Δλmax in logarithmic time scale for different pressure (shifting factor (αP) is presented with arrow). (d) Time-Pressure superposition of PAAm/Au film.

material to different loading histories, PAAm/Au films have "time-pressure superposition" as a function of shift in absorption.[131] Note that the deformation (creeping) of a linear viscoelastic material follows this mathematical approach. Therefore, the change in absorption may be the evidence for the governing of the color transformation through the rate of deformation and the change in time according to the Kelvin-Voigt viscoelastic model.

Since matrix polymer provides a viscous medium for the diffusion during dis/assembly of the Au particles, the viscoelastic properties of the surrounding polymer is a significant parameter for this sensor system. The viscosity of a polymer is inversely proportional to temperature; therefore one can suggest that a change in temperature causes a dramatic effect on the shift of absorption signal at constant pressure. In this sense, the change in color of PAAm/Au films was investigated in terms of the relation between viscosity and temperature (Equation 4.2). The relation can be given according to Exponential relation;

$$\eta\,(\text{T}) = \eta_0 \exp(-b\text{T}) \qquad (4.2)$$

where η_0 is absolute viscosity, b is constant, and T is the temperature. In Figure 4.7, temperature-dependent minor alterations in the absorption signal are given for different pressure scales. At the low pressure of 40 MPa, λ_{max} peak position shifts from 575 nm to 562 nm as the temperature increases to 50 °C. Note that the resolution of the spectrometer is 1.02 nm. At constant pressure, the viscosity of the composite film is expected to decrease as the temperature increases (according to Equation 4.2). Therefore, the rate of deformation increases with the lowered viscosity and causes the shift of λ_{max} in the
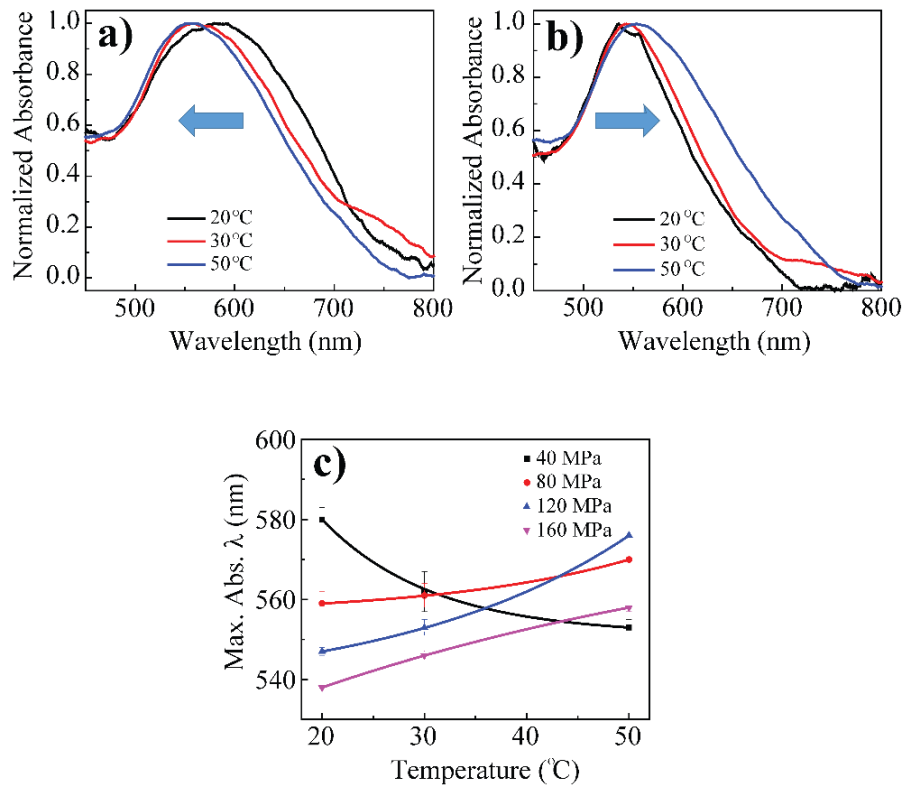
Figure 4.7. Absorption spectra of the constant pressure applied films ((a) 40 MPa and (b) 160 MPa) at various temperatures and (c) the change of the corresponding λmax with respect to temperature.

absorption spectrum to become more dramatic. For higher-pressure scales, the aforementioned trend in the shift gradually turns into opposite direction and λ_{max} starts to increase as temperature increases. This temperature-induced reverse shift may be attributed to a morphological change in the PAAm matrix upon the deformation.

To elucidate the morphological changes of the films at elevated temperature, a detailed structural analysis was performed. SEM images and XRD patterns of pressure-loaded and -unloaded films at 50 °C are presented in Figure 4.8. The composite film of PAAm matrix

and Au NPs shows a smooth surface upon compressing with 40 MPa (Figure 4.8a). When the pressure is doubled to 80 MPa, the rice-like shape elongated bright structures are surprisingly observed. The thickness of the structures is 305 nm and the length is 960 nm. The shape remains unchanged as rice-like; however, the diameters are getting longer, when the pressure further increases to 160 MPa. They grow into 480 nm and 2.6 µm, respectively (Figure 4.8b and c).

Figure 4.8d presents the XRD pattern of the PAAm/Au films employed under different deformations at 50 °C. All patterns exhibit characteristic Au signals at 38.9° and 45.1° (2θ), which may belong to (111) and (200) planes, respectively.[132, 133] The unloaded film
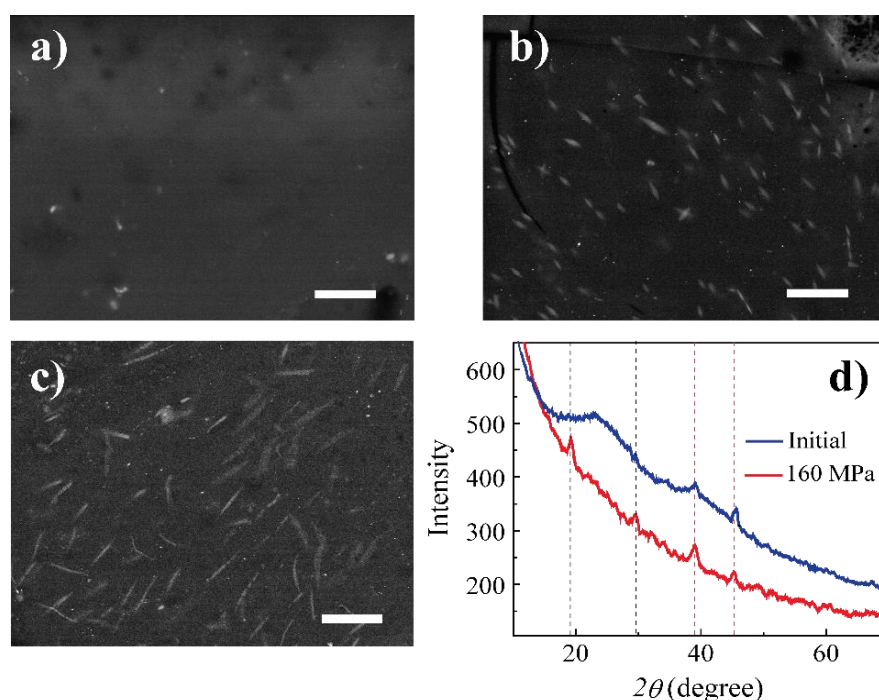
Figure 4.8. SEM images of the films in diverse conditions (a) 40 MPa, (b) 80 MPa, and (c) 160 MPa at 50 °C (Scale bar: 5 µm) , (d) XRD patterns of loaded and unloaded films at 50 °C.

shows amorphous halo at the initial state, which disappears as the pressure increases. The additional signals that may arise from polymer crystallites are observed at 19.1° and 29.3° (2θ). Since rice-like formations consist of a similar chemical structure with the polymer matrix (Figure 4.9) and XRD pattern shows sharp additional reflections, they may hint about the occurrence of *pressure-induced crystallization*. Therefore, the contrast in microscopy images can be attributed to a crystallized polymer structure that is oriented along the flow direction upon application of pressure. Since the polymer chains are packed more closely and tightly in crystalline formation than its amorphous counterpart,

the density of crystallites (ρ_c) will be higher than the corresponding amorphous region. For the polymers having both substituent, namely semi-crystalline, Equation 4.3 gives an approximate relationship between densities;

$$\rho_{sc}/\rho_a = 1 + 0.13\chi_c \qquad (4.3)$$

where ρ_a and ρ_a are density of the amorphous and semi-crystalline polymer and χ_c is the degree of crystallinity.[134] In the case of stress-induced crystallization of PAAm, volumetric loss of equal weighted polymer region can be defined as the difference between volumes of amorphous (V_a) and crystalline (V_c) regions (Equation 4.4). Therefore, the change in peak position with different regimes at elevated temperatures may be attributed to this volumetric loss upon crystallization because it inversely affects the deformation of PAAm/Au film.
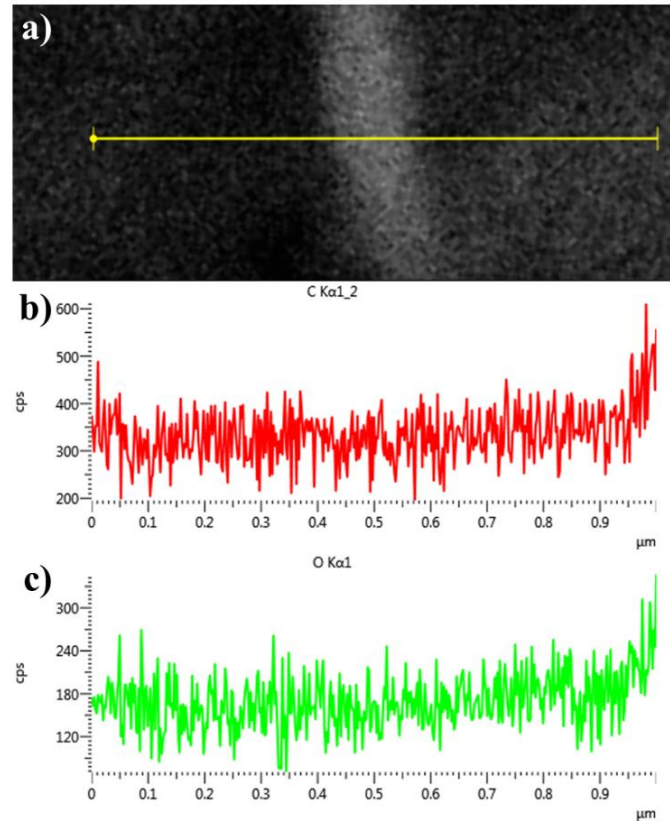
Figure 4.9. (a) SEM image and corresponding EDX line spectra of the loaded film (160 MPa, 50 °C) recorded from both smooth surface and rice-like shape regions for (b) carbon and (c) oxygen.

$$V_a - V_c = 0.13\chi_c V_c \qquad (4.4)$$

The self-healing materials possess the ability to heal in deformation including cracks, voids, rupture, etc. Therefore, the materials having self-healing feature provide accurate measurement of the applied force even they exposed shape deterioration. Considering the nature of PAAm, i.e. capability to form hydrogel via H-bonding, it is expected that the pressure sensitive PAAm/Au composites could demonstrate self-healing feature under appropriate conditions. This feature of the PAAm/Au stimuli-responsive film was determined by simple deformation test under ambient condition. The time-evolution of the self-healing period is presented in Figure 4.10 as a photo frame. Initially, the non-deformed bluish films were divided into two pieces and placed 1 mm apart from each other. After a while, it is observed that these two pieces start to contact each other and the gap is completely filled in five days. The recovery of PAAm hydrogels has been reported in the literature.[135, 136] Since the acrylamide pendant group consists of acidic hydrogen, oxygen and nitrogen that are able to form secondary interaction (hydrogen bond) with both intermolecular and water molecules, the re-arrangement of polymer chains may be triggered by their exposure to the water molecules. Therefore, not surprisingly, the PAAm matrix in this study having lower molecular weight (1500 g/mol) can be self-recovered even in the presence of moisture in air. Self-healing of PAAm/Au films without any chemical additive is robust enough to overcome detrimental problems in biocompatibility and environmental contamination issues, which may provide a wide range application.

Figure 4.10. Photographs of the Au NP/PAAm composite divided into two pieces. The self-healing feature is shown as a function of time.

Considering the cell phones are ubiquitous devices in daily life, smartphone-assisted detection may offer inexpensive and accessible alternative quantifying the dramatic color change of PAAm/Au films.[137] In this sense, since almost all the cell phones have the ability to take a photograph today, a simple algorithm in order to estimate applied pressure is proposed here as a possible cell phone application. Under a fixed pressure, a PAAm/Au composite film can response a particular color back from a range spanning a continuous color distribution between blue and red. Even though data points regarding to color versus applied pressure have been obtained throughout this study are discrete (because there are only 5 data in total representing the color vs pressure from 0 to 160 MPa), one can try to search for a possible pattern that these data points may follow in order to obtain a
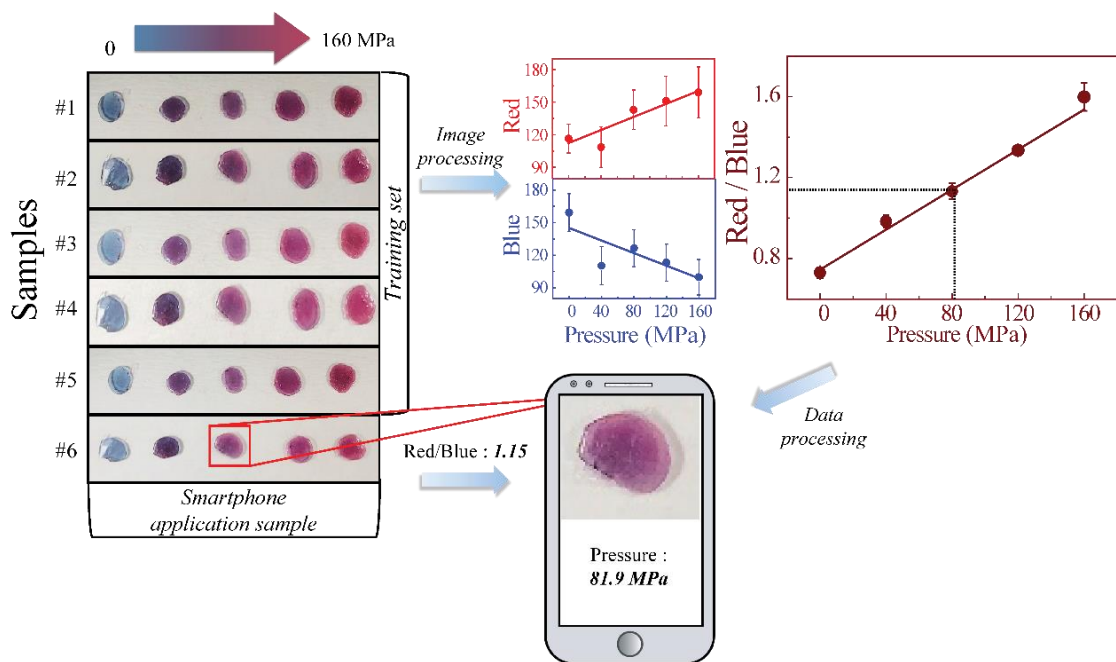
Figure 4.11. Schematic illustration of smart-phone application and linear curve of red and blue color intensity.

continuous one-to-one matching of color-pressure distribution. By using such a pattern, one can design a regression algorithm based on performing image processing on the taken photograph of PAAm/Au composite film to estimate the applied pressure even apart from the ones used in this study. Captured photograph of any sample shows variation in the red-green-blue (RGB) values of the corresponding pixels depending on the distance and angle between the phone and sample. Therefore, to reduce estimation error, a satisfactory dataset should be constructed to obtain the pattern, which can be achieved by employing multiple images for every color and corresponding pressure. In this sense, the dataset consists of two different sample sets consisting of initial state and 40, 80, 120, and 160

MPa pressures, and their three different photographs were considered. To train the algorithm, for every pressure including initial state, there are five different corresponding images were employed. This training dataset, as presented in Figure 4.11, was then used to determine average red (red plot) and blue (blue plot) pixel values of every image referring to its corresponding pressure. As the pressure increases, corresponding average pixel values for red follow an increasing linear curve while blue follows a decreasing linear pattern as expected. To reduce the dimension in order to simplify the algorithm, the ratio of these two parameters (red/blue) was considered. Red/blue coordinates versus applied pressure fitted to almost a perfect linear curve, which hints about that there is a significant error reduction compared to the case of analyzing red and blue individually. Remaining sample (Sample 6) was employed as a test dataset to estimate the pressure and calculate corresponding errors. As an illustration, the image of the resulting color under 80 MPa pressure was considered. After taking its photograph by cell phone through the application, the algorithm behind this application calculates the red/blue immediately, which was found as 1.15 for this case. Then, by putting 1.15 as y in the linear equation of y=mx + b, where m (0.00494), and b (0.74501) already determined through curve fitting process, one can obtain the corresponding pressure as x. Here, the pressure was calculated as 81.9 MPa, which has an error ~ 2%. For the remaining samples, from 0 to 160 MPa, estimated pressures and their errors were given in Table 4.1. For the further reduction of error, one can produce and use more samples in training dataset or optimize the image processing techniques since cropping the specific region from the rest of the image leads to information loss while determining the values of red and blue. Nevertheless, the algorithm proposed in this study has sufficient error rate, it is simple, and can be employed

Table 4.1. Numerical results for RGB test set.

Applied Pressure (MPa)	Red	Blue	Red / Blue	Pressure	Error (%)
0	125.71	170.83	0.74	-1.01	<1
40	99.11	108.23	0.92	35.42	11
80	153.85	133.30	1.15	81.98	2
120	165.30	123.24	1.34	120.44	<1
160	169.74	107.00	1.59	171.05	7

as a cell phone application to estimate the pressure using the resulting color of PAAm/Au composite.

4.3. Conclusions

A stress-responsive colorimetric PAAm/Au films having self-healing properties were fabricated and their optical response upon external mechanical force was examined. Initially, the films with dark blue color turn into ruby red as the pressure is applied to 160 MPa most probably due to the disassembly of Au NP clusters in the film. Since PAAm chains interact with Au NPs, the motion of polymer acts as a part of the disassembly during a deformation. The distinct plasmonic shift not only depends on the magnitude of pressure but also the duration of applied pressure. Therefore, the stimuli-responsive PAAm/Au films can be employed even lower scales by extending the duration of applied pressure. The red-shift in absorbance was observed at lower pressures as the temperature increases probably due to decreasing the viscosity of PAAm. In order to increase the working range of the sensor, i.e. at higher pressures, one can crosslink the chains where the diffusion of Au particles is hindered. Such that the blue color is hardly transformed into reddish individual particles. Moreover, for the practical applicability of the PAAm/Au films, RGB-based algorithm was developed to use in the simple for the smart-phone application for photographic detection of applied pressure with ~ 2% error.

CHAPTER 5

EFFECT OF CHAIN TOPOLOGY ON PRESSURE SENSOR FILMS BASED ON POLY(ACRYLAMIDE) AND AU NANOPARTICLES

Au NP-based colorimetric sensors have been developed for a wide variety of functions. In general, the particles can be associated with the surrounding polymer matrix of which mechanical and viscoelastic properties play a significant role. For instance, *Han et al.* proposed that the addition of poly(ethylene glycol) into poly(vinyl pyrrolidone) (PVP) as a plasticizer remarkably facilitate and enhance the plasmonic shift due to provide ease of diffusion of Au NPs, therefore their separation.[13] In addition, the disassembly of plasmonic nanoparticles upon external mechanical stimuli is more favorable if the polymer has pendant group that is able to easily interact with the particle, e.g. pyrrolidone or amide.[138] Since the surrounding matrix plays a vital role for the disassembly of the nanoparticles, hindering particle diffusion through various topologies of polymer chains may offer an alternative for the fabrication of colorimetric pressure sensors working at higher-pressure ranges in various fields such as industrial machinery, construction, agriculture, where high-pressure monitoring is essential.[139]

The polymers consisting of linear chains intrinsically resemble liquids with regard to their flow behavior. On the contrary, the crosslinked chains provide solidification and maintaining the material shape against deformation. Therefore, the crosslinking of polymer chains has been predominantly used for the enhancement of the material toughness and chemical inertness due to its ease of implementation. A three-dimensional network of polyacrylamide (PAAm) can be obtained by using aldehyde compounds due to the capability of reacting with amide groups.[140-142]

This part of the thesis provides insight into the effect of polymer chain topology on the optical properties of Au NP/PAAm films upon pressure. The fabrication of the colorimetric pressure sensor films was carried out by integration of Au NPs into PAAm

matrix. The spectral and colorimetric changes by disassembly of Au NP clusters were observed as a function of the amount of crosslinking agent (formaldehyde) and the applied pressure. Besides the crosslinking of the PAAm chains, the humidity was also studied since the motion of the particles in the polymeric system is significantly influenced. The effect of humidity on colorimetric response against pressure and color healing was examined.

5.1. Materials and Methods

The synthesis of Au NPs was carried out using the aforementioned strategy by similar reagents. PAAm solution (50% w/v, M_w: 1500 g/mol, Sigma-Aldrich), methanol (≥99.8%, VWR) and formalin (40% w/v formaldehyde, Carlo Erba) were purchased and used to prepare polymer network having a various concentration of crosslink agents.

The crosslinking was obtained by the reaction between PAAm and formaldehyde (FA) (Figure 5.1). An aliquot of PAAm solution (2 mL) was diluted to 35% w/v using 0.84 mL deionized water. Subsequently, the mixture was acidified using 25 µL HCl solution (0.1 M) and loaded to a sealed glass container to purge with nitrogen. The desired amount of formalin solution was (from 0.5 to 5% mol of PAAm) injected to the system. The solution was then allowed for mixing at 60 °C for 12 h. The resulting polymers were precipitated using an excess amount of methanol. Afterward, the white precipitates were filtered and washed with methanol 3 times and dried at 40 °C under vacuum. The dried white powders
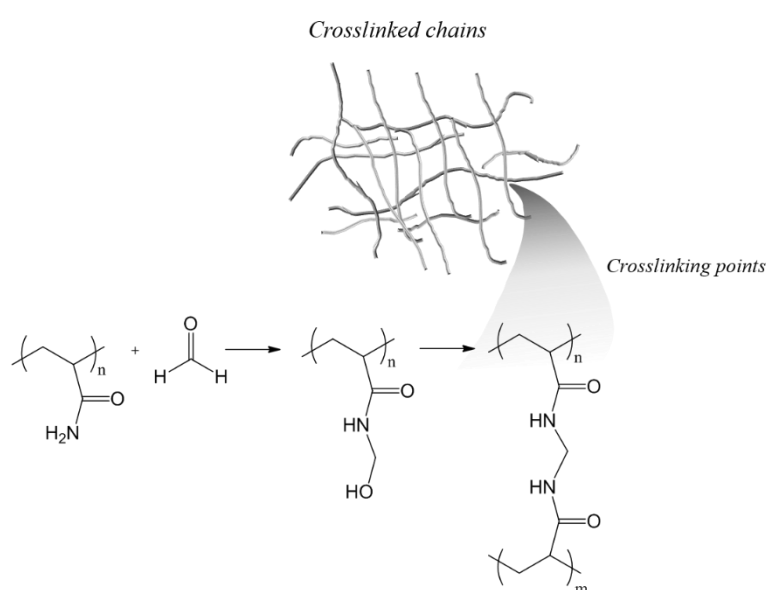
Figure 5.1. Schematic illustration of the crosslink reaction.

were dissolved in deionized water and the concentration was fixed to 50% w/v for further use.

Firstly, Au NP (50 µL) solution was mixed to PVP solution (10 µL, 0.16% w/v in water) to enhance the stabilization of the particles. Next, the PVP modified Au NPs were loaded to PAAm solutions (400 µL), respectively. The solution of which the ruby red color rapidly transformed into deep blue color was drop-casted into a mold and dried at 60 °C for 2 h.

5.2. Results and Discussion
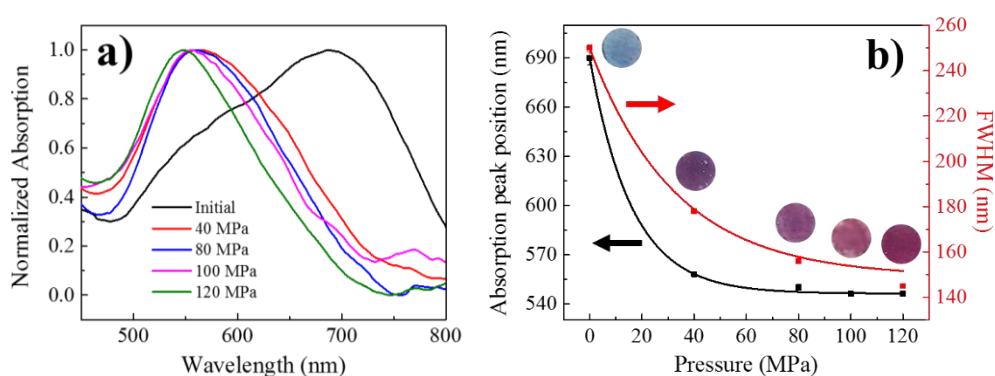
Figure 5.2. (a) Absorption spectra and corresponding (b) peak position and FWHM of neat PAAm/Au film under various pressure at 73% RH. Insets show appearance of film color.

The addition of PAAm solution into PVP-stabilized Au NP dispersion causes aggregation probably due to the change in pH. The remaining citrate molecules detach from particle surface that leads to aggregation. The color of the mixture changes from red to blue. By evaporation of the water from the mixture, the blue appearance was fixed and the composite films were obtained. The blue films were divided into small pieces to perform compression experiments between 40 and 160 MPa. The intensive compression onto PAAm/Au films resulted in a significant color change from blue to red. The corresponding absorption spectra of the film for each pressure are given in Figure 5.2a. For initial state, the broad signal is observed at 690 nm with a shoulder. The position of the shoulder (550 nm) is close to the signal of the individual particle dispersion. There is a clear difference between the absorption signal of individual Au NPs (520 nm) and its aggregates (690 nm). Since these two levels of particle state coexist in the composite system, the effect of pressure is mainly examined by their spectroscopic signals. For this

particular spectrum, it can be stated that a few numbers of individual particles still exist together with aggregates in the dried form of the blue composite. As the pressure increases, the absorption spectrum clearly shows a shift toward lower wavelength and finally reaches to 545 nm for 120 MPa compression. This dramatic spectral change is originated from the pressure-induced disassembly of Au NP aggregates. Nevertheless, the difference between peak positions is nearly 25 nm obtained from individual particle dispersion and compressed films. This result suggests that complete disassembly cannot be achieved even at higher pressure; rather aggregated domains still exist in the compressed film structure. Besides the spectral shift, the shape of the spectra also changes. The absorption signals get narrow as the pressure increases. Both dissipative and radiative mechanisms to the damping of the collective electron oscillation may contribute to this result.[143-145] More specifically, light re-emission (scattering) becomes negligible for small spherical metal nanoparticles, which leads to spectral narrowing of the LSPR with the disassembly of aggregates. The limit of spectral narrowing may be a result of the dissipative mechanisms. In Figure 5.2b, the changes (shift and narrowing) in the spectra with respect to pressure are given. Both the signal position and full width at half maximum (FWHM) of the spectrum show an exponential decrease as the pressure increases. On the other hand, the appearance of films for each compression level is presented as an inset of the figure such that a clear change in color from blue to red is clearly observed.

The spectral change at constant pressure was examined as a function of FA content used during the preparation of the films. The absorption spectrum of each film having different FA content under 40 MPa compression is presented in Figure 5.3a. The signal position of the non-crosslinked film in the spectrum falls to 556 nm while it shifts to higher wavelength by increasing FA concentration. Moreover, the signal is getting broaden at longer wavelengths. For the disassembly of the particles in the polymer matrix, the general sense is the use of the polymer that can allow continuous flow under the external mechanical stimuli. On the other hand, the use of FA leads to the reduction in the flow rate of the matrix under fixed mechanical force. The effect of crosslinking on the optical properties of the film has been investigated for the structural development of PAAm/Au particle nanocomposite materials. It was previously reported that the crosslinking points of the polymer chains reduce the free volume in the material, hence hinder the diffusion of the nanoparticles.[146, 147] Therefore, the Au NP aggregates with an inhibited diffusion

result in relatively weaker disassembly under similar mechanical stimuli compared to the particles in a non-crosslinked matrix. Thus, the shift in absorbance decreases as the concentration of crosslinking agent increases. The higher the crosslinking, the harder the particles diffuse. In Figure 5.3b, the change in peak position with respect to pressure for
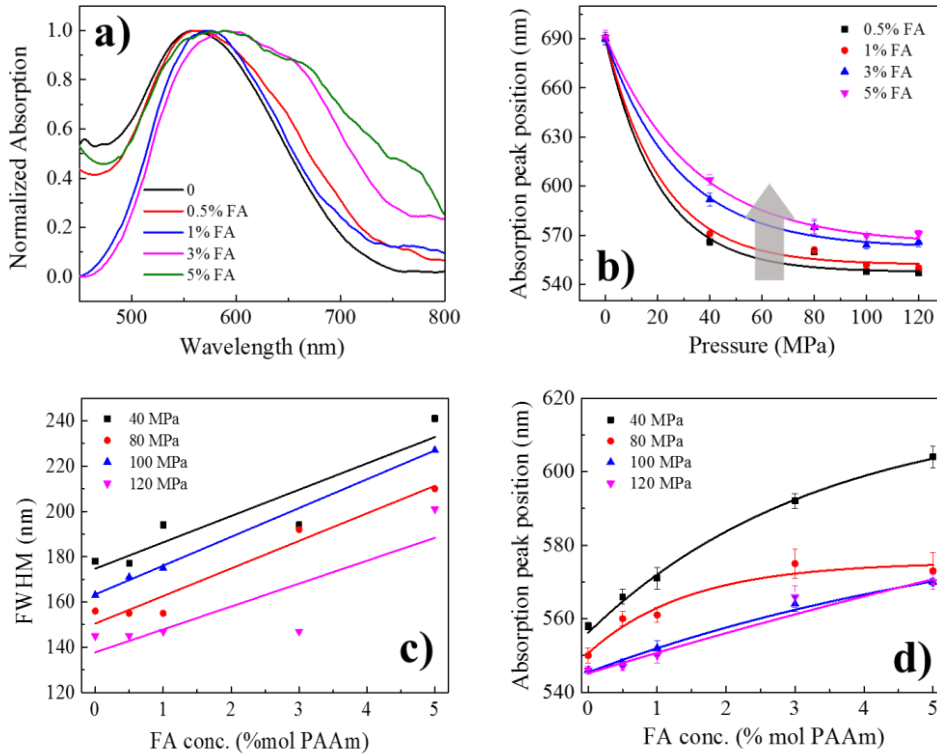
Figure 5.3. (a) Absorption spectra of PAAm/Au films for each FA content under 40 MPa and (b) peak position of the films versus pressure. The change in (c) FWHM and (d) peak position of the films with changing FA content, respectively. The measurements were carried out at 73% RH.

different FA content is presented. Obviously, all regimes follow a dramatic decrease as the pressure increases and the range of shift differs for each film. At high concentration of the crosslinking agent, this range gets narrower and final peak position reaches to only 571 nm, namely 26 nm higher than non-crosslinked one. FWHM of the signal of the films shows a linear increase with respect to FA content under all pressures (Figure 5.3c). The viscosity of the medium is dramatically increased by crosslinking. The particle domains prefer to stay in aggregated state because the crosslinking points may hinder their diffusion into individual particles. Similarly, the shift in peak position increases as FA content increases (Figure 5.3d). At low FA content, the peak position is close to the signal of individual Au particles. However, at high concentrations, the signal is close to one of

their corresponding clusters probably due to the aforementioned formation of a three-dimensional network by crosslinking agent.

Since the PAAm consists of hydrophilic pendant groups on carbon backbone, the material frequently employed in a diverse application as a hydrogel.[148, 149] PAAm especially having short chain length has hygroscopic nature, hence their solid form may be dramatically affected by even moisture in the air atmosphere.[150, 151] Therefore, the optical response of PAAm/Au NP sensor films was investigated in a humid environment. The films were exposed to various relative humidity (RH; 73, 80, and 87 %) for half an hour
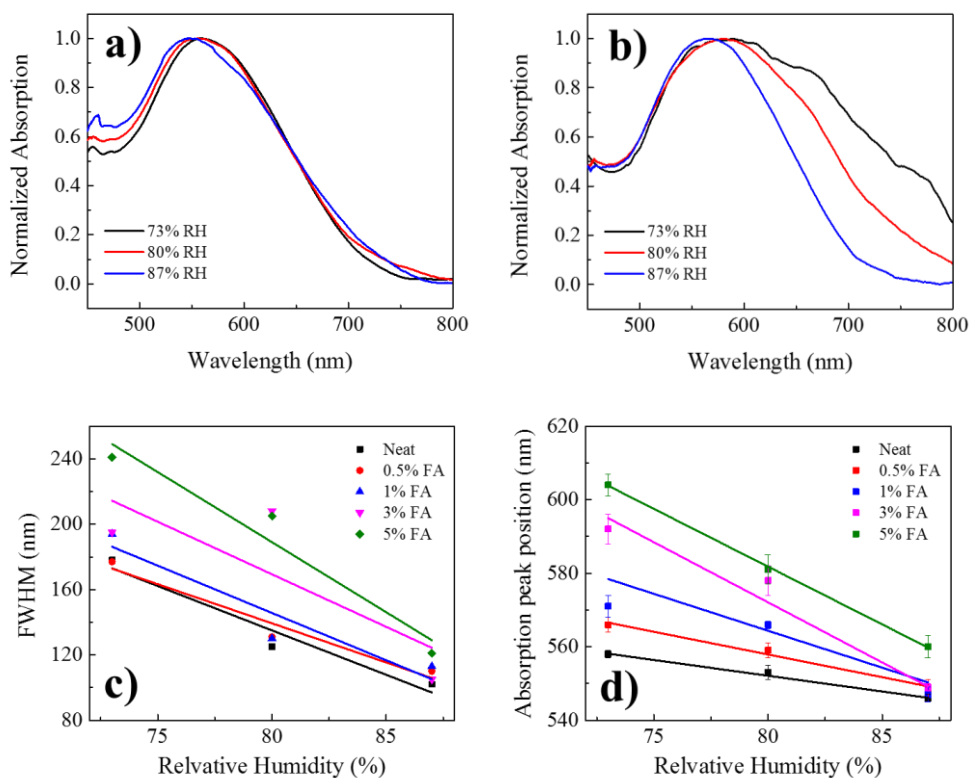
Figure 5.4. Absorption spectra of the (a) non-crosslinked and (b) crosslinked (5% FA) films for various RH. The change in (c) FWHM and (d) peak position of the films having various FA content with changing RH, respectively. The measurements were carried out under 40 MPa.

and the compression tests were carried out. In Figure 5.4a, absorption spectra of the films prepared by non-crosslinked (linear) chains at different RH conditions for 40 MPa pressure are presented. The spectra remain more or less unchanged under all humidity levels tested. On the other hand, humidity has a strong influence on the crosslinked PAAm matrix and corresponding spectra are shown in Figure 5.4b. Compared to the neat counterpart, the signals differentiate dramatically for the films prepared by 5% FA. The

signal falls to 604 nm for 73% RH while it is observed at 566 nm for 87% RH. Since the number of remaining aggregates appears more dominant in the crosslinked films, the softening by increasing RH has a considerable change in absorption compared to the non-crosslinked case. In Figure 5.4c and d, FWHM and absorption peak position are given as a function of RH, respectively. Both of them show linear decrease as the RH increases. It is well established that humidity swells the polymer chains such that the particles find a convenient medium for the diffusion. Under pressure, the particle domains can diffuse into the individual particles and the signal shifts toward 540 nm even for the crosslinked systems.

The crosslinking has a strong influence on the absorption spectrum and as well as the appearance of the films. The photo-frame of the corresponding films is given with respect to the amount of FA in the course of film preparation (column) and applied pressure (row) (Figure 5.5a). The color of the film gradually turns into reddish as the pressure increases as each of the rows are followed. The change in color ambiguously observed in the case of a higher degree of crosslinking. The effect of crosslinking at constant pressure on color change can be clearly distinguished for each column. In contrast to the effect of pressure, the color turns into bluish as the FA content increases. Note that the change in color with increasing crosslinking is more clearly observed in the case of higher compression. These results may suggest that the films can be employed not only for the measurement of the magnitude of pressure but also for the distribution of the pressure over the material. Two
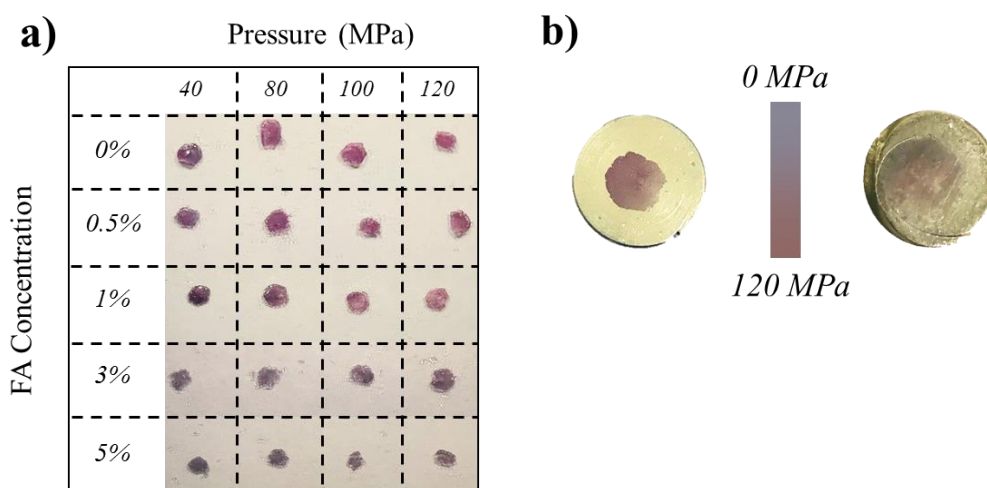
Figure 5.5. (a) Photo frame of the films having different FA content under various pressure at 73% RH. The appearance of the films after compression on (b) smooth (left) and rough (right) surfaces.

identical films were compressed on smooth and rough surfaces, separately. The photographs of the resulting films are presented in Figure 5.5b. The former case leads to smooth and single colored reddish film. It can be claimed that the pressure is homogeneously dispersed over the smooth surface. On the other hand, the latter one resulted as having multiple colors with a gradual transition and seems a mixture of the blue and red, i.e. the pressure is heterogeneously dispersed over the film surface. The change in the color throughout the film may hint about the distribution of applied pressure.

Since the hygroscopic feature of PAAm has a considerable influence on the motion of the Au NPs, the humidity may affect dis/assembly in steady state as much as upon the compression. The film was compressed with 120 MPa and exposed to 95% RH for 6 h. The appearance of the film for each stage is presented and corresponding absorption spectra are given in Figure 5.6a and b. The initial blue colored film turns into reddish by
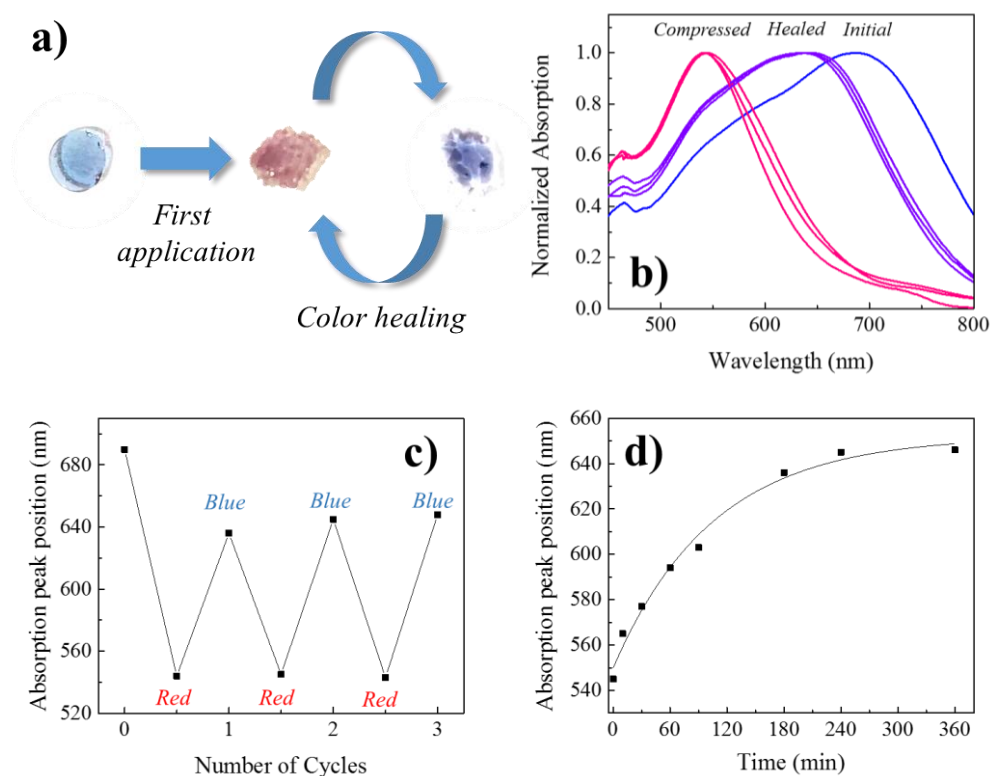
Figure 5.6. Detailed approach for color healing feature of the films; (a) the appearance during process, (b) absorption spectra (recorded after 6 h healing), (c) the peak position upon color healing cycle, and (d) time evolution of color healing.

compression, not surprisingly. Subsequently, the humidity treatment causes color back from reddish to bluish and the absorption signal shifts from 545 to 645 nm. The color

healing process may be simply explained by further gelation of the polymers due to excessive humidity. The particles have enough free volume to assemble back that results in bluish colored aggregates. Even though the color cannot be fully healed under humidity, the peak position of the compressed film falls to 545 nm for each cycle, which may suggest that it is a reversible process (Figure 5.6c). The time evolution of color healing is presented in Figure 5.6d. The peak position exponentially increases to 645 nm and fixed at this wavelength.

5.3. Conclusions

Pressure-sensitive colorimetric PAAm/Au NP films containing the various degree of crosslinking were fabricated and their sensor properties were investigated in terms of their optical response upon pressure up to 120 MPa under various humidity levels. The blue
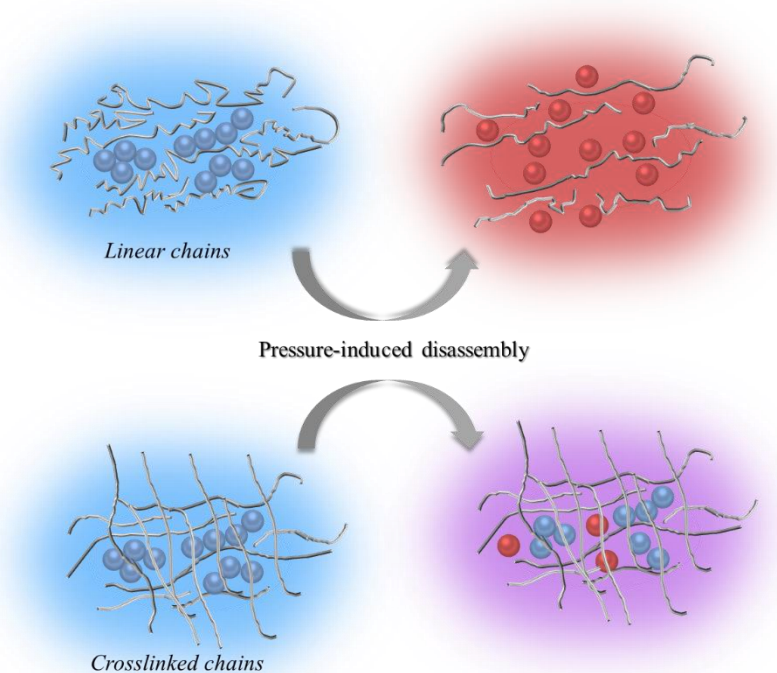
Figure 5.7. The effect of linear and crosslinked chains on optical change under

color of the films at the initial state gradually turns into reddish under pressure due to the disassembly of Au NP aggregates, which results as a spectral shift in the absorbance. The shift under certain pressure not only depends on the magnitude of applied force but also internal and external circumstances such as the amount of crosslinking agent in the preparation and humidity of the environment. Since the dis/integration of the Au nanoparticles is based on the diffusion process in the presence of polymer chains,

changing the architecture of the polymer chains from linear to crosslinked allows controlling the pressure range where the sensor is active (Figure 5.7). The usage of formaldehyde retards the colorimetric change, this result suggests that the pressure range required obtaining the same amount of shift increases, i.e. meaning that this material system can shift the working range of the sensor material to higher pressures. For the reusability of the PAAm/Au films, its exposure to humidity seems a promising way for healing both in structure and in color.

CHAPTER 6

OVERALL CONCLUSIONS

In this thesis, for the fabrication of colorimetric sensing materials, advanced optical composites were fabricated and their optical activity upon applied mechanical forces was examined. The SiO_2 and Au NPs were employed to obtain photonic and plasmonic features. The particles were synthesized by Stöber and Turkevich methods, respectively. Since the colorimetric activity is directly correlated to the size and shape of the particles, their size was controlled by the concentration of raw materials, i.e. TEOS and $HAuCl_4$.

The SiO_2 colloidal particles were deposited onto different substrates by using both the drop-casting and spraying process. The oriented SiO_2 colloidal particles provide vivid structural colors due to a strong interfered scattering of incident light from the ordered nanopattern. The degree of particle orientation results in angle in/dependent coloration. The contact angle of the colloid onto surface plays an important role for particle order. The iridescent colors are directly satisfied by Bragg-Snell's Law. Therefore, the colors vary with observation angle and size of building blocks. In similar, quasi-ordered SiO_2 patterns also show different and stable colors. As particle size increases from 150 to 300 nm, the reflection wavelength increases from 385 to 575 nm. Moreover, the additional reflection signal is observed for greater diameters of the particles, which may arise due to single particle resonance and/or double scattering mechanisms.

The quasi-ordered structures were integrated into the PDMS matrix. Since the refractive indices of the particles and the polymeric matrix are quite similar, the structural colored films transform into colorless and highly transparent films. The change in reflection and transmission of the elastomer was recorded under various lateral strain levels. The transparency of the film gradually turns into opaque and the intensity of transmission decays by half while strain level reaches to 60%. On the other hand, the reflection signals become detectable while the strain level exceeds the threshold level. It is concluded that

the optical activity of transparent films depends on the voids forming strain direction due to refractive index mismatching.

The Au NPs were integrated into PAAm having low molecular weight. The red colored particle dispersion was precisely aggregated and color transforms to blue due to LSPR. The pressure-induced colorimetric change of the resulting blue polymeric film is examined. The color turns back to red, i.e. absorption signal shifts from 690 to 540 nm, while the magnitude of exerted force exceeds 100 MPa. The underlying mechanism of this pressure sensitive colorimetric change may arise due to disassembly of Au NPs. Since the diffusion of the particles governed by the motion of the polymeric matrix, the disassembly rate is strongly correlated to mechanical properties of the surrounding polymer. Therefore, the parameters such as temperature, duration of pressure, humidity, and crosslinking that are able to affect the mechanical properties of the film were examined. The viscoelastic nature of PAAm governs the disassembly of the particles. The relation between optical and mechanical features of the films are expressed and discussed mathematically, namely with the Kelvin-Voigt model. In addition, the colorimetric changes were recorded and a simple algorithm was developed to pave the way for smartphone-assisted detection.

In summary, colorimetric mechanical sensors appear to be a young member of the sensor family with unique optical properties. In this thesis, a number of detailed works regarding colorimetric strain and pressure sensors based on plasmonic and photonic mechanisms were presented and their mechanical sensor applications and fabrication processes were discussed. Most of the advancements in plasmonic and photonic polymer composites have been observed in the last two decades, thus the development of colorimetric mechanical sensors is still far from attaining maturity. Hence, this work may provide further understanding for advanced optical composites and their application in mechanical sensors.

REFERENCES

1.   Carlson, R. W., Telemetric device. *Google Patents*: **1936**.

2.   Katzir, S., The discovery of the piezoelectric effect. *The begınnıngs of pıezoelectrıcıty*, Springer: **2006**; pp 15-64.

3.   Ballato, A. *Piezoelectricity: history and new thrusts*, 1996 IEEE Ultrasonics Symposium. Proceedings, IEEE: **1996**; pp 575-583.

4.   Smith, C. S., Piezoresistance effect in germanium and silicon. *Physical Review* **1954,** *94* (1), 42.

5.   Polye, W., Temperature compensator for capacitive pressure transducers. Google Patents: **1973**.

6.   Bell, R. L., Capacitive pressure transducer. *Google Patents*: **1979**.

7.   Topcu, G.; Guner, T.; Demir, M. M., Pressure Sensors Based on IPMC Actuator. *Ionic Polymer Metal Composites for Sensors and Actuators*, Springer: **2019**; pp 161-182.

8.   Gong, S.; Schwalb, W.; Wang, Y.; Chen, Y.; Tang, Y.; Si, J.; Shirinzadeh, B.; Cheng, W., A wearable and highly sensitive pressure sensor with ultrathin gold nanowires. *Nature Communications* **2014,** *5*, 3132.

9.   Someya, T.; Sekitani, T.; Iba, S.; Kato, Y.; Kawaguchi, H.; Sakurai, T., A large-area, flexible pressure sensor matrix with organic field-effect transistors for artificial skin applications. *Proceedings of the National Academy of Sciences* **2004,** *101* (27), 9966-9970.

10.   Lee, G. H.; Choi, T. M.; Kim, B.; Han, S. H.; Lee, J. M.; Kim, S.-H., Chameleon-Inspired Mechanochromic Photonic Films Composed of Non-Close-Packed Colloidal Arrays. *ACS Nano* **2017,** *11* (11), 11350-11357.

11.   Topçu, G.; Güner, T.; Demir, M. M., Non-iridescent structural colors from uniform-sized SiO2 colloids. *Photonics Nanostructures-Fundamentals Applications* **2018,** *29*, 22-29.

12.   Gu, Z. Z.; Uetsuka, H.; Takahashi, K.; Nakajima, R.; Onishi, H.; Fujishima, A.; Sato, O., Structural Color and the Lotus Effect. *Angewandte Chemie International Edition* **2003,** *115* (8), 863-863.

13.   Han, X.; Liu, Y.; Yin, Y., Colorimetric stress memory sensor based on disassembly of gold nanoparticle chains. *Nano Letters* **2014,** *14* (5), 2466-2470.

14.   Hierold, C.; Jungen, A.; Stampfer, C.; Helbling, T., Nano electromechanical sensors based on carbon nanotubes. *Sensors and Actuators A: Physical* **2007,** *136* (1), 51-61.

15. Smith, A.; Niklaus, F.; Paussa, A.; Vaziri, S.; Fischer, A. C.; Sterner, M.; Forsberg, F.; Delin, A.; Esseni, D.; Palestri, P., Electromechanical piezoresistive sensing in suspended graphene membranes. *Nano Letters* **2013,** *13* (7), 3237-3242.

16. Keshavarzi, A.; Shahinpoor, M.; Kim, K. J.; Lantz, J. W. *Blood pressure, pulse rate, and rhythm measurement using ionic polymer-metal composite sensors*, Smart Structures and Materials: Electroactive Polymer Actuators and Devices, International Society for Optics and Photonics: **1999**; pp 369-377.

17. Maruyama, T.; Sasaki, S.; Saito, Y., Potentiometric gas sensor for carbon dioxide using solid electrolytes. *Solid State Ionics* **1987,** *23* (1-2), 107-112.

18. Akar, O.; Akin, T.; Najafi, K., A wireless batch sealed absolute capacitive pressure sensor. *Sensors and Actuators A: Physical* **2001,** *95* (1), 29-38.

19. Chattopadhyay, S.; Sarkar, J.; Bera, S. C., A low cost design and development of a reluctance type pressure transducer. *Measurement* **2013,** *46* (1), 491-496.

20. Ge, D.; Lee, E.; Yang, L.; Cho, Y.; Li, M.; Gianola, D. S.; Yang, S., A Robust Smart Window: Reversibly Switching from High Transparency to Angle-Independent Structural Color Display. *Advanced Materials* **2015,** *27* (15), 2489-2495.

21. Zhang, Y.; Hu, Y.; Zhu, P.; Han, F.; Zhu, Y.; Sun, R.; Wong, C.-P., Flexible and Highly Sensitive Pressure Sensor Based on Microdome-Patterned PDMS Forming with Assistance of Colloid Self-Assembly and Replica Technique for Wearable Electronics. *ACS applied materials & interfaces* **2017,** *9* (41), 35968-35976.

22. Teyssier, J.; Saenko, S. V.; Van Der Marel, D.; Milinkovitch, M. C., Photonic crystals cause active colour change in chameleons. *Nature Communications* **2015,** *6*, 6368.

23. Kristensen, A.; Yang, J. K.; Bozhevolnyi, S. I.; Link, S.; Nordlander, P.; Halas, N. J.; Mortensen, N. A., Plasmonic colour generation. *Nature Reviews Materials* **2017,** *2* (1), 16088.

24. Fu, Y.; Tippets, C. A.; Donev, E. U.; Lopez, R., Structural colors: from natural to artificial systems. *Wiley Interdisciplinary Reviews: Nanomedicine Nanobiotechnology* **2016,** *8* (5), 758-775.

25. Braun, P. V., Materials science: Colour without colourants. *Nature* **2011,** *472* (7344), 423.

26. Ball, P., *Bright earth: art and the invention of color*. University of Chicago Press: 2003.

27. Zollinger, H., *Color chemistry: syntheses, properties, and applications of organic dyes and pigments*. John Wiley & Sons: 2003.

28. Schroden, R. C.; Al-Daous, M.; Blanford, C. F.; Stein, A., Optical properties of inverse opal photonic crystals. *Chemistry of Materials* **2002,** *14* (8), 3305-3315.

29. Marlow, F.; Sharifi, P.; Brinkmann, R.; Mendive, C., Opals: status and prospects. *Angewandte Chemie International Edition* **2009,** *48* (34), 6212-6233.

30. Joannopoulos, J.; Johnson, S.; Winn, J.; Meade, R., Photonic Crystals: Molding the Flow of Light. *Princeton University Press* **2008,** *2*, 94-99.

31. Özçelik, S.; Demir, M. M.; Birkan, B., Probing nanoscale domains of J-aggregates deposited on a mica surface. *The Journal of Physical Chemistry B* **2004,** *108* (15), 4679-4683.

32. Güner, T.; Köseoğlu, D.; Demir, M. M., Multilayer design of hybrid phosphor film for application in LEDs. *Optical Materials* **2016,** *60*, 422-430.

33. Güner, T.; Şentürk, U.; Demir, M. M., Optical enhancement of phosphor-converted wLEDs using glass beads. *Optical Materials* **2017,** *72*, 769-774.

34. Kinoshita, S.; Yoshioka, S.; Miyazaki, J., Physics of structural colors. *Reports on Progress in Physics* **2008,** *71* (7), 076401.

35. Colombini, M. P.; Andreotti, A.; Baraldi, C.; Degano, I.; Łucejko, J. J., Colour fading in textiles: A model study on the decomposition of natural dyes. *Microchemical Journal* **2007,** *85* (1), 174-182.

36. Ghelardi, E.; Degano, I.; Colombini, M. P.; Mazurek, J.; Schilling, M.; Khanjian, H.; Learner, T., A multi-analytical study on the photochemical degradation of synthetic organic pigments. *Dyes and Pigments* **2015,** *123*, 396-403.

37. Lundberg, I.; Milatou-Smith, R., Mortality and cancer incidence among Swedish paint industry workers with long-term exposure to organic solvents. *Scandinavian Journal of Work, Environment Health* **1998**, 270-275.

38. Takeoka, Y.; Yoshioka, S.; Takano, A.; Arai, S.; Nueangnoraj, K.; Nishihara, H.; Teshima, M.; Ohtsuka, Y.; Seki, T., Production of colored pigments with amorphous arrays of black and white colloidal particles. *Angewandte Chemie International Edition* **2013,** *52* (28), 7261-7265.

39. Graham-Rowe, D., Tunable structural colour. *Nature Photonics* **2009,** *3* (10), 551.

40. Han, M. G.; Shin, C. G.; Jeon, S. J.; Shim, H.; Heo, C. J.; Jin, H.; Kim, J. W.; Lee, S., Full color tunable photonic crystal from crystalline colloidal arrays with an engineered photonic stop-band. *Advanced Materials* **2012,** *24* (48), 6438-6444.

41. Ingram, A.; Parker, A., A review of the diversity and evolution of photonic structures in butterflies, incorporating the work of John Huxley (The Natural History Museum, London from 1961 to 1990). *Philosophical Transactions of the Royal Society B: Biological Sciences* **2008,** *363* (1502), 2465-2480.

42.   Srinivasarao, M., Nano-optics in the biological world: beetles, butterflies, birds, and moths. *Chemical Reviews* **1999,** *99* (7), 1935-1962.

43.   Potyrailo, R. A.; Ghiradella, H.; Vertiatchikh, A.; Dovidenko, K.; Cournoyer, J. R.; Olson, E., Morpho butterfly wing scales demonstrate highly selective vapour response. *Nature Photonics* **2007,** *1* (2), 123.

44.   Kinoshita, S.; Yoshioka, S., Structural colors in nature: the role of regularity and irregularity in the structure. *ChemPhysChem* **2005,** *6* (8), 1442-1459.

45.   Zhao, Y.; Xie, Z.; Gu, H.; Zhu, C.; Gu, Z., Bio-inspired variable structural color materials. *Chemical Society Reviews* **2012,** *41* (8), 3297-3317.

46.   Vukusic, P.; Sambles, J. R., Photonic structures in biology. *Nature* **2003,** *424* (6950), 852.

47.   Vigneron, J. P.; Simonis, P., Natural photonic crystals. *Physica B: Condensed Matter* **2012,** *407* (20), 4032-4036.

48.   Dumanli, A. G.; Savin, T., Recent advances in the biomimicry of structural colours. *Chemical Society Reviews* **2016,** *45* (24), 6698-6724.

49.   Cong, H.; Yu, B.; Wang, S.; Qi, L.; Wang, J.; Ma, Y., Preparation of iridescent colloidal crystal coatings with variable structural colors. *Optics Express* **2013,** *21* (15), 17831-17838.

50.   Yoshioka, S.; Nakamura, E.; Kinoshita, S., Origin of two-color iridescence in rock dove's feather. *Journal of the Physical Society of Japan* **2007,** *76* (1), 013801.

51.   Gu, H.; Ye, B.; Ding, H.; Liu, C.; Zhao, Y.; Gu, Z., Non-iridescent structural color pigments from liquid marbles. *Journal of Materials Chemistry C* **2015,** *3* (26), 6607-6612.

52.   Takeoka, Y., Angle-independent structural coloured amorphous arrays. *Journal of Materials Chemistry* **2012,** *22* (44), 23299-23309.

53.   Yoshioka, S.; Takeoka, Y., Production of colourful pigments consisting of amorphous arrays of silica particles. *ChemPhysChem* **2014,** *15* (11), 2209-2215.

54.   Shi, L.; Zhang, Y.; Dong, B.; Zhan, T.; Liu, X.; Zi, J. J. A. M., Amorphous Photonic Crystals with Only Short-Range Order. *Advanced Materials* **2013,** *25* (37), 5314-5320.

55.   Dong, B.; Liu, X.; Zhan, T.; Jiang, L.; Yin, H.; Liu, F.; Zi, J., Structural coloration and photonic pseudogap in natural random close-packing photonic structures. *Optics Express* **2010,** *18* (14), 14430-14438.

56.   Wang, H.; Zhang, K.-Q., Photonic crystal structures with tunable structure color as colorimetric sensors. *Sensors* **2013,** *13* (4), 4192-4213.

57. Aguirre, C. I.; Reguera, E.; Stein, A., Tunable colors in opals and inverse opal photonic crystals. *Advanced Functional Materials* **2010,** *20* (16), 2565-2578.

58. Woltman, S. J.; Jay, G. D.; Crawford, G. P., Liquid-crystal materials find a new order in biomedical applications. *Nature Materials* **2007,** *6* (12), 929.

59. Yadav, A.; De Angelis, R.; Casalboni, M.; De Matteis, F.; Prosposito, P.; Nanni, F.; Cacciotti, I., Spectral properties of self-assembled polystyrene nanospheres photonic crystals doped with luminescent dyes. *Optical Materials* **2013,** *35* (8), 1538-1543.

60. Haque, M. A.; Kamita, G.; Kurokawa, T.; Tsujii, K.; Gong, J. P., Unidirectional alignment of lamellar bilayer in hydrogel: one-dimensional swelling, anisotropic modulus, and stress/strain tunable structural color. *Advanced Materials* **2010,** *22* (45), 5110-5114.

61. Forster, J. D.; Noh, H.; Liew, S. F.; Saranathan, V.; Schreck, C. F.; Yang, L.; Park, J. G.; Prum, R. O.; Mochrie, S. G.; O'Hern, C. S. J. A. M., Biomimetic isotropic nanostructures for structural coloration. *Advanced Materials* **2010,** *22* (26-27), 2939-2944.

62. Zhang, Y.; Dong, B.; Chen, A.; Liu, X.; Shi, L.; Zi, J., Using Cuttlefish Ink as an Additive to Produce Non-iridescent Structural Colors of High Color Visibility. *Advanced Materials* **2015,** *27* (32), 4719-4724.

63. Chung, K.; Yu, S.; Heo, C. J.; Shim, J. W.; Yang, S. M.; Han, M. G.; Lee, H. S.; Jin, Y.; Lee, S. Y.; Park, N., Flexible, angle-independent, structural color reflectors inspired by morpho butterfly wings. *Advanced Materials* **2012,** *24* (18), 2375-2379.

64. Ge, D.; Yang, L.; Wu, G.; Yang, S., Spray coating of superhydrophobic and angle-independent coloured films. *Chemical Communications* **2014,** *50* (19), 2469-2472.

65. Cui, L.; Zhang, Y.; Wang, J.; Ren, Y.; Song, Y.; Jiang, L., Ultra-Fast Fabrication of Colloidal Photonic Crystals by Spray Coating. *Macromolecular Rapid Communications* **2009,** *30* (8), 598-603.

66. Harun-Ur-Rashid, M.; Bin Imran, A.; Seki, T.; Ishii, M.; Nakamura, H.; Takeoka, Y., Angle-independent structural color in colloidal amorphous arrays. *ChemPhysChem* **2010,** *11* (3), 579-583.

67. Wang, F.; Zhang, X.; Lin, Y.; Wang, L.; Zhu, J., Structural coloration pigments based on carbon modified ZnS@ SiO2 nanospheres with low-angle dependence, high color saturation, and enhanced stability. *ACS Applied Materials & Interfaces* **2016,** *8* (7), 5009-5016.

68. Lee, I.; Kim, D.; Kal, J.; Baek, H.; Kwak, D.; Go, D.; Kim, E.; Kang, C.; Chung, J.; Jang, Y., Quasi-amorphous colloidal structures for electrically tunable full-color photonic pixels with angle-independency. *Advanced Materials* **2010,** *22* (44), 4973-4977.

69.   Stöber, W.; Fink, A.; Bohn, E., Controlled growth of monodisperse silica spheres in the micron size range. *Journal of Colloid Interface Science* **1968,** *26* (1), 62-69.

70.   Carcouët, C. C.; Van De Put, M. W.; Mezari, B.; Magusin, P. C.; Laven, J.; Bomans, P. H.; Friedrich, H.; Esteves, A. C. C.; Sommerdijk, N. A.; Van Benthem, R. A., Nucleation and growth of monodisperse silica nanoparticles. *Nano Letters* **2014,** *14* (3), 1433-1438.

71.   Joannopoulos, J. D.; Johnson, S. G.; Winn, J. N.; Meade, R. D., *Photonic crystals: molding the flow of light*. Princeton university press: 2011.

72.   Takeoka, Y.; Honda, M.; Seki, T.; Ishii, M.; Nakamura, H., Structural colored liquid membrane without angle dependence. *ACS Applied Materials & Interfaces* **2009,** *1* (5), 982-986.

73.   Kumano, N.; Seki, T.; Ishii, M.; Nakamura, H.; Takeoka, Y., Tunable Angle-Independent Structural Color from a Phase-Separated Porous Gel. *Angewandte Chemie International Edition* **2011,** *50* (17), 4012-4015.

74.   Park, J. G.; Kim, S. H.; Magkiriadou, S.; Choi, T. M.; Kim, Y. S.; Manoharan, V. N., Full-Spectrum photonic pigments with non-iridescent structural colors through colloidal assembly. *Angewandte Chemie International Edition* **2014,** *53* (11), 2899-2903.

75.   Noh, H.; Liew, S. F.; Saranathan, V.; Prum, R. O.; Mochrie, S. G.; Dufresne, E. R.; Cao, H., Double scattering of light from biophotonic nanostructures with short-range order. *Optics Express* **2010,** *18* (11), 11942-11948.

76.   Noh, H.; Liew, S. F.; Saranathan, V.; Prum, R. O.; Mochrie, S. G.; Dufresne, E. R.; Cao, H., Contribution of double scattering to structural coloration in quasiordered nanostructures of bird feathers. *Physical Review E* **2010,** *81* (5), 051923.

77.   Magkiriadou, S.; Park, J.-G.; Kim, Y.-S.; Manoharan, V. N., Absence of red structural color in photonic glasses, bird feathers, and certain beetles. *Physical Review E* **2014,** *90* (6), 062302.

78.   Demir, M. M.; Wegner, G. J. M. M.; Engineering, Challenges in the preparation of optical polymer composites with nanosized pigment particles: a review on recent efforts. **2012,** *297* (9), 838-863.

79.   Sanchez, C.; Lebeau, B.; Chaput, F.; Boilot, J. P. J. A. M., Optical properties of functional hybrid organic–inorganic nanocomposites. **2003,** *15* (23), 1969-1994.

80.   Pucci, A.; Bizzarri, R.; Ruggeri, G. J. S. M., Polymer composites with smart optical properties. **2011,** *7* (8), 3689-3700.

81.   Takeoka, Y. J. J. o. M. C. C., Stimuli-responsive opals: colloidal crystals and colloidal amorphous arrays for use in functional structurally colored materials. **2013,** *1* (38), 6059-6074.

82. Diao, Y. Y.; Liu, X. Y.; Toh, G. W.; Shi, L.; Zi, J. J. A. F. M., Multiple structural coloring of silk-fibroin photonic crystals and humidity-responsive color sensing. **2013,** *23* (43), 5373-5380.

83. Zhao, Q.; Finlayson, C. E.; Snoswell, D. R.; Haines, A.; Schäfer, C.; Spahn, P.; Hellmann, G. P.; Petukhov, A. V.; Herrmann, L.; Burdet, P. J. N. c., Large-scale ordering of nanoparticles using viscoelastic shear processing. **2016,** *7,* 11661.

84. Liu, F.; Dong, B.; Liu, X.; Zheng, Y.; Zi, J., Structural color change in longhorn beetles Tmesisternus isabellae. *Optics Express* **2009,** *17* (18), 16183-16191.

85. Stavenga, D. G.; Leertouwer, H. L.; Marshall, N. J.; Osorio, D., Dramatic colour changes in a bird of paradise caused by uniquely structured breast feather barbules. *Proceedings of the Royal Society of London B: Biological Sciences* **2010**, rspb20102293.

86. Holt, A. L.; Sweeney, A. M.; Johnsen, S.; Morse, D. E., A highly distributed Bragg stack with unique geometry provides effective camouflage for Loliginid squid eyes. *Journal of The Royal Society Interface* **2011,** *8* (63), 1386-1399.

87. Zylinski, S.; Johnsen, S., Mesopelagic cephalopods switch between transparency and pigmentation to optimize camouflage in the deep. *Current Biology* **2011,** *21* (22), 1937-1941.

88. Stuart-Fox, D.; Whiting, M. J.; Moussalli, A. J. B. J. o. t. L. S., Camouflage and colour change: antipredator responses to bird and snake predators across multiple populations in a dwarf chameleon. **2006,** *88* (3), 437-446.

89. Teyssier, J.; Saenko, S. V.; Van Der Marel, D.; Milinkovitch, M. C. J. N. c., Photonic crystals cause active colour change in chameleons. **2015,** *6,* 6368.

90. Ge, D.; Lee, E.; Yang, L.; Cho, Y.; Li, M.; Gianola, D. S.; Yang, S. J. A. M., A Robust Smart Window: Reversibly Switching from High Transparency to Angle-Independent Structural Color Display. **2015,** *27* (15), 2489-2495.

91. Ito, T.; Katsura, C.; Sugimoto, H.; Nakanishi, E.; Inomata, K. J. L., Strain-responsive structural colored elastomers by fixing colloidal crystal assembly. **2013,** *29* (45), 13951-13957.

92. Lee, G. H.; Choi, T. M.; Kim, B.; Han, S. H.; Lee, J. M.; Kim, S.-H. J. A. n., Chameleon-inspired mechanochromic photonic films composed of non-close-packed colloidal arrays. **2017,** *11* (11), 11350-11357.

93. Reese, C. E.; Mikhonin, A. V.; Kamenjicki, M.; Tikhonov, A.; Asher, S. A. J. J. o. t. A. C. S., Nanogel nanosecond photonic crystal optical switching. **2004,** *126* (5), 1493-1496.

94. Burgess, I. B.; Koay, N.; Raymond, K. P.; Kolle, M.; Lonˇcar, M.; Aizenberg, J. J. A. n., Wetting in color: colorimetric differentiation of organic liquids with high selectivity. **2011,** *6* (2), 1427-1437.

95.   Wang, X. Q.; Wang, C. F.; Zhou, Z. F.; Chen, S., Hydrogels: Robust Mechanochromic Elastic One-Dimensional Photonic Hydrogels for Touch Sensing and Flexible Displays (Advanced Optical Materials 7/2014). *Advanced Optical Materials* **2014,** *2* (7), 651-651.

96.   Jia, X.; Wang, J.; Wang, K.; Zhu, J., Highly sensitive mechanochromic photonic hydrogels with fast reversibility and mechanical stability. *Langmuir* **2015,** *31* (31), 8732-8737.

97.   Hong, R.; Shi, Y.; Wang, X.-Q.; Peng, L.; Wu, X.; Cheng, H.; Chen, S., Highly sensitive mechanochromic photonic gel towards fast-responsive fingerprinting. *RSC Advances* **2017,** *7* (53), 33258-33262.

98.   Lawrence, J. R.; Ying, Y.; Jiang, P.; Foulger, S. H., Dynamic tuning of organic lasers with colloidal crystals. *Advanced Materials* **2006,** *18* (3), 300-303.

99.   Ye, S.; Fu, Q.; Ge, J., Invisible photonic prints shown by deformation. *Advanced Functional Materials* **2014,** *24* (41), 6430-6438.

100.   Ding, T.; Cao, G.; Schäfer, C. G.; Zhao, Q.; Gallei, M.; Smoukov, S. K.; Baumberg, J. J.; interfaces, Revealing invisible photonic inscriptions: Images from strain. *ACS Applied Materials & Interfaces* **2015,** *7* (24), 13497-13502.

101.   McQuarrie, D. A.; Simon, J. D., *Physical Chemistry: a Molecular Approach*. Sausalito: University Science Books: 1997.

102.   Raman, K.; Murthy, T. S.; Hegde, G., Fabrication of refractive index tunable polydimethylsiloxane photonic crystal for biosensor application. *Physics Procedia* **2011,** *19*, 146-151.

103.   Malitson, I., Interspecimen comparison of the refractive index of fused silica. *Josa* **1965,** *55* (10), 1205-1209.

104.   Yang, D.; Ye, S.; Ge, J., Solvent wrapped metastable colloidal crystals: highly mutable colloidal assemblies sensitive to weak external disturbance. *Journal of the American Chemical Society* **2013,** *135* (49), 18370-18376.

105.   Gu, Z. Z.; Uetsuka, H.; Takahashi, K.; Nakajima, R.; Onishi, H.; Fujishima, A.; Sato, O., Structural color and the lotus effect. *Angew. Chem. Int. Edit.* **2003,** *42* (8), 894-897.

106.   Vanderkooy, A.; Chen, Y.; Gonzaga, F.; Brook, M. A., Silica Shell/Gold Core Nanoparticles: Correlating Shell Thickness with the Plasmonic Red Shift upon Aggregation. *ACS Applied Materials & Interfaces* **2011,** *3* (10), 3942-3947.

107.   Rankin, A.; McGarry, S., A flexible pressure sensitive colour changing device using plasmonic nanoparticles. *Nanotechnology* **2015,** *26* (7), 075502.

108.   Jiang, N.; Zhuo, X.; Wang, J., Active plasmonics: Principles, structures, and applications. *Chemical Reviews* **2017,** *118* (6), 3054-3099.

109.   Saha, K.; Agasti, S. S.; Kim, C.; Li, X.; Rotello, V. M., Gold Nanoparticles in Chemical and Biological Sensing. *Chemical Reviews* **2012,** *112* (5), 2739-2779.

110.   Zeng, S.; Yong, K.-T.; Roy, I.; Dinh, X.-Q.; Yu, X.; Luan, F., A Review on Functionalized Gold Nanoparticles for Biosensing Applications. *Plasmonics* **2011,** *6* (3), 491.

111.   Qian, Z.; Ginger, D. S., Reversibly Reconfigurable Colloidal Plasmonic Nanomaterials. *Journal of the American Chemical Society* **2017,** *139* (15), 5266-5276.

112.   Zhao, Y.; Cao, L.; Ouyang, J.; Wang, M.; Wang, K.; Xia, X.-H., Reversible plasmonic probe sensitive for pH in micro/nanospaces based on i-motif-modulated morpholino-gold nanoparticle assembly. *Analytical Chemistry* **2012,** *85* (2), 1053-1057.

113.   Lee, S. E.; Chen, Q.; Bhat, R.; Petkiewicz, S.; Smith, J. M.; Ferry, V. E.; Correia, A. L.; Alivisatos, A. P.; Bissell, M. J., Reversible aptamer-Au plasmon rulers for secreted single molecules. *Nano Letters* **2015,** *15* (7), 4564-4570.

114.   Yan, Y.; Samai, S.; Bischoff, K. L.; Zhang, J.; Ginger, D. S., Photocontrolled DNA hybridization stringency with fluorescence detection in heterogeneous assays. *ACS Sensors* **2016,** *1* (5), 566-571.

115.   Wang, C.; Du, Y.; Wu, Q.; Xuan, S.; Zhou, J.; Song, J.; Shao, F.; Duan, H., Stimuli-responsive plasmonic core–satellite assemblies: i-motif DNA linker enabled intracellular pH sensing. *Chemical Communications* **2013,** *49* (51), 5739-5741.

116.   Liu, X.-Y.; Cheng, F.; Liu, Y.; Li, W.-G.; Chen, Y.; Pan, H.; Liu, H.-J., Thermoresponsive gold nanoparticles with adjustable lower critical solution temperature as colorimetric sensors for temperature, pH and salt concentration. *Journal of Materials Chemistry* **2010,** *20* (2), 278-284.

117.   Tagliazucchi, M.; Blaber, M. G.; Schatz, G. C.; Weiss, E. A.; Szleifer, I., Optical properties of responsive hybrid Au@ polymer nanoparticles. *ACS Nano* **2012,** *6* (9), 8397-8406.

118.   Chen, J. I.; Chen, Y.; Ginger, D. S., Plasmonic nanoparticle dimers for optical sensing of DNA in complex media. *Journal of the American Chemical Society* **2010,** *132* (28), 9600-9601.

119.   Joshi, G. K.; Blodgett, K. N.; Muhoberac, B. B.; Johnson, M. A.; Smith, K. A.; Sardar, R., Ultrasensitive photoreversible molecular sensors of azobenzene-functionalized plasmonic nanoantennas. *Nano Letters* **2014,** *14* (2), 532-540.

120.   Yan, Y.; Chen, J. I.; Ginger, D. S., Photoswitchable oligonucleotide-modified gold nanoparticles: controlling hybridization stringency with photon dose. *Nano Letters* **2012,** *12* (5), 2530-2536.

121.   Huang, F.; Baumberg, J. J., Actively tuned plasmons on elastomerically driven Au nanoparticle dimers. *Nano Letters* **2010,** *10* (5), 1787-1792.

122. Balazs, A. C.; Emrick, T.; Russell, T. P., Nanoparticle polymer composites: where two small worlds meet. *Science* **2006,** *314* (5802), 1107-1110.

123. Spildo, K.; Sæ, E. I. Ø., Effect of Charge Distribution on the Viscosity and Viscoelastic Properties of Partially Hydrolyzed Polyacrylamide. *Energy & Fuels* **2015,** *29* (9), 5609-5617.

124. Munro, J. C.; Frank, C. W., Polyacrylamide Adsorption from Aqueous Solutions on Gold and Silver Surfaces Monitored by the Quartz Crystal Microbalance. *Macromolecules* **2004,** *37* (3), 925-938.

125. Bai, J.; Li, Y.; Du, J.; Wang, S.; Zheng, J.; Yang, Q.; Chen, X., One-pot synthesis of polyacrylamide-gold nanocomposite. *Materials Chemistry and Physics* **2007,** *106* (2), 412-415.

126. Darnell, M. C.; Sun, J.-Y.; Mehta, M.; Johnson, C.; Arany, P. R.; Suo, Z.; Mooney, D. J., Performance and biocompatibility of extremely tough alginate/polyacrylamide hydrogels. *Biomaterials* **2013,** *34* (33), 8042-8048.

127. Turkevich, J.; Stevenson, P. C.; Hillier, J., A study of the nucleation and growth processes in the synthesis of colloidal gold. *Discussions of the Faraday Society* **1951,** *11*, 55-75.

128. Zhong, Z.; Patskovskyy, S.; Bouvrette, P.; Luong, J. H. T.; Gedanken, A., The Surface Chemistry of Au Colloids and Their Interactions with Functional Amino Acids. *J. Phys. Chem. B.* **2004,** *108* (13), 4046-4052.

129. Ung, T.; Liz-Marzán, L. M.; Mulvaney, P., Optical Properties of Thin Films of Au@SiO2 Particles. *J. Phys. Chem. B*. **2001,** *105* (17), 3441-3452.

130. Vanderkooy, A.; Chen, Y.; Gonzaga, F.; Brook, M. A., Silica shell/gold core nanoparticles: correlating shell thickness with the plasmonic red shift upon aggregation. *ACS Appl. Mater. Inter.* **2011,** *3* (10), 3942-3947.

131. Roylance, D., Engineering viscoelasticity. *Department of Materials Science and Engineering–Massachusetts Institute of Technology, Cambridge MA* **2001,** *2139*, 1-37.

132. Philip, D., Biosynthesis of Au, Ag and Au–Ag nanoparticles using edible mushroom extract. *Spectrochimica Acta Part A: Molecular Biomolecular Spectroscopy* **2009,** *73* (2), 374-381.

133. Shen, C.; Hui, C.; Yang, T.; Xiao, C.; Tian, J.; Bao, L.; Chen, S.; Ding, H.; Gao, H., Monodisperse noble-metal nanoparticles and their surface enhanced Raman scattering properties. *Chemistry of Materials* **2008,** *20* (22), 6939-6944.

134. Van Krevelen, D. W.; Te Nijenhuis, K., *Properties of polymers: their correlation with chemical structure; their numerical estimation and prediction from additive group contributions*. Elsevier: 2009.

135. Sato, K.; Nakajima, T.; Hisamatsu, T.; Nonoyama, T.; Kurokawa, T.; Gong, J. P., Phase-Separation-Induced Anomalous Stiffening, Toughening, and Self-Healing of Polyacrylamide Gels. *Adv. Mater.* **2015,** *27* (43), 6990-6998.

136. Tuncaboylu, D. C.; Sahin, M.; Argun, A.; Oppermann, W.; Okay, O., Dynamics and large strain behavior of self-healing hydrogels with and without surfactants. *Macromolecules* **2012,** *45* (4), 1991-2000.

137. İncel, A.; Akın, O.; Çağır, A.; Yıldız, Ü. H.; Demir, M. M., Smart phone assisted detection and quantification of cyanide in drinking water by paper based sensing platform. *Sensor. Actuat. B-Chem.* **2017,** *252*, 886-893.

138. Topcu, G.; Guner, T.; Inci, E.; Demir, M. M., Colorimetric and plasmonic pressure sensors based on polyacrylamide/Au nanoparticles. *Sensors and Actuators A: Physical* **2019,** *295*, 503-511.

139. Topcu, G.; Demir, M. M., Effect of chain topology on plasmonic properties of pressure sensor films based on poly(acrylamide) and Au nanoparticles. *Sensors and Actuators A: Physical* **2019,** *295*, 237-243.

140. Bakalik, D. P.; Kowalski, D. J. J., The reaction of polyacrylamide, formaldehyde, and sodium bisulfite. *Journal of Polymer Science Part A: Polymer Chemistry* **1987,** *25* (1), 433-436.

141. Fong, D. W.; Kowalski, D. J., An investigation of the crosslinking of polyacrylamide with formaldehyde using 13C nuclear magnetic resonance spectroscopy. *Journal of Polymer Science Part A: Polymer Chemistry* **1993,** *31* (6), 1625-1627.

142. Marandi, G. B.; Esfandiari, K.; Biranvand, F.; Babapour, M.; Sadeh, S.; Mahdavinia, G., pH sensitivity and swelling behavior of partially hydrolyzed formaldehyde-crosslinked poly (acrylamide) superabsorbent hydrogels. *Journal of Applied Polymer Science* **2008,** *109* (2), 1083-1092.

143. Juvé, V.; Cardinal, M. F.; Lombardi, A.; Crut, A.; Maioli, P.; Pérez-Juste, J.; Liz-Marzán, L. M.; Del Fatti, N.; Vallée, F., Size-dependent surface plasmon resonance broadening in nonspherical nanoparticles: single gold nanorods. *Nano Letters* **2013,** *13* (5), 2234-2240.

144. Klar, T.; Perner, M.; Grosse, S.; Von Plessen, G.; Spirkl, W.; Feldmann, J., Surface-plasmon resonances in single metallic nanoparticles. *Physical Review Letters* **1998,** *80* (19), 4249.

145. Sönnichsen, C.; Franzl, T.; Wilk, T.; von Plessen, G.; Feldmann, J.; Wilson, O.; Mulvaney, P., Drastic reduction of plasmon damping in gold nanorods. *Physical Review Letters* **2002,** *88* (7), 077402.

146. Wegner, G.; Demir, M. M.; Faatz, M.; Gorna, K.; Munoz-Espi, R.; Guillemet, B.; Gröhn, F., Polymers and inorganics: a happy marriage? *Macromolecular Research* **2007,** *15* (2), 95-99.

147. Demir, M. M.; Castignolles, P.; Akbey, Ü.; Wegner, G., In-situ bulk polymerization of dilute particle/MMA dispersions. *Macromolecules* **2007,** *40* (12), 4190-4198.

148. Denisin, A. K.; Pruitt, B. L.; interfaces, Tuning the range of polyacrylamide gel stiffness for mechanobiology applications. *ACS Applied Materials and Interfaces* **2016,** *8* (34), 21893-21902.

149. Magdeldin, S.; Enany, S.; Yoshida, Y.; Xu, B.; Zhang, Y.; Zureena, Z.; Lokamani, I.; Yaoita, E.; Yamamoto, T., Basics and recent advances of two dimensional-polyacrylamide gel electrophoresis. *Clinical Proteomics* **2014,** *11* (1), 16.

150. Naguib, M.; Saito, T.; Lai, S.; Rager, M. S.; Aytug, T.; Paranthaman, M. P.; Zhao, M.-Q.; Gogotsi, Y., Ti 3 C 2 T x (MXene)–polyacrylamide nanocomposite films. *RSC Advances* **2016,** *6* (76), 72069-72073.

151. Lee, K. E.; Khan, I.; Morad, N.; Teng, T. T.; Poh, B. T., Thermal behavior and morphological properties of novel magnesium salt–polyacrylamide composite polymers. *Polymer Composites* **2011,** *32* (10), 1515-1522.

APPENDIX A

MATLAB CODES OF THE ALGORITHM

data={sp10 sp140 sp180 sp1120 sp1160;sp20 sp240 sp280 sp2120 sp2160;sp30 sp340 sp380 sp3120 sp3160;sp40 sp440 sp480 sp4120 sp4160;sp50 sp540 sp580 sp5120 sp5160;sp60 sp640 sp680 sp6120 sp6160};

%This array 'data' contains the all dataset we use for both training and test. Here, for instance, sp440 means (sp4)40 – (fourth sample) under 4×10^4 psi pressure. Another example, sp20 means (sp2)0 – (second sample) under 0 psi pressure (no pressure applied cases).

pressurer=[];

pressureg=[];

pressureb=[];

pressurer0=[];

pressureg0=[];

pressureb0=[];

pressurer40=[];

pressureb40=[];

pressureg40=[];

pressurer80=[];

pressureg80=[];

pressureb80=[];

pressurer120=[];

pressureg120=[];

pressureb120=[];

pressurer160=[];

```matlab
pressureg160=[];

pressureb160=[];

%Here, these empty arrays are defined already to add values to them based on red,
green, or red and based on corresponding pressures.


for i=1:1:5

   for j=1:1:5

      spbw=im2bw(data{i,j},0.6);

      spbw=1-spbw;

      veri=data{i,j};

      veri(:,:,1)=double(veri(:,:,1)).*spbw;

      veri(:,:,2)=double(veri(:,:,2)).*spbw;

      veri(:,:,3)=double(veri(:,:,3)).*spbw;

      toplamr=sum(sum(veri(:,:,1)));

      toplamg=sum(sum(veri(:,:,2)));

      toplamb=sum(sum(veri(:,:,3)));

      miktar=size(nonzeros(spbw));

      miktar=miktar(1);

      if j==1

         pressurer0(end+1)=toplamr/miktar;

         pressureg0(end+1)=toplamg/miktar;

         pressureb0(end+1)=toplamb/miktar;

      end

      if j==2

         pressurer40(end+1)=toplamr/miktar;

         pressureg40(end+1)=toplamg/miktar;

         pressureb40(end+1)=toplamb/miktar;

      end

      if j==3

         pressurer80(end+1)=toplamr/miktar;

         pressureg80(end+1)=toplamg/miktar;
```

```
        pressureb80(end+1)=toplamb/miktar;

      end

      if j==4

        pressurer120(end+1)=toplamr/miktar;

        pressureg120(end+1)=toplamg/miktar;

        pressureb120(end+1)=toplamb/miktar;

      end

      if j==5

        pressurer160(end+1)=toplamr/miktar;

        pressureg160(end+1)=toplamg/miktar;

        pressureb160(end+1)=toplamb/miktar;

      end

    end

end
```

% These loops are for calculating the red, green, and blue values of related images as a result of their subtraction from their corresponding backgrounds.


```
pressures=[0 40 80 120 160];
```

% This variable stands for the pressure (x-axis)


```
pressurerson=[mean(pressurer0) mean(pressurer40) mean(pressurer80)
mean(pressurer120) mean(pressurer160)];
```

```
pressuregson=[mean(pressureg0) mean(pressureg40) mean(pressureg80)
mean(pressureg120) mean(pressureg160)];
```

```
pressurebson=[mean(pressureb0) mean(pressureb40) mean(pressureb80)
mean(pressureb120) mean(pressureb160)];
```

% These three variables present an array consisting of resulting averages of the red, green, and blue values of the corresponding pressures


```
redtoblue=pressurerson./pressurebson;
```

%This variable stands for the ratio of Red/Blue as indicated by the Figure 4.11.

VITA

PERSONAL INFORMATION

Surname, Name: Topçu, Gökhan
Nationality: Turkish (TC)
Date and Place of Birth: 29.06.1989, Fatih/İstanbul
E-mail: topcu_gokhan@windowslive.com

EDUCATION

Degree, Institution, Year of Graduation
MSc, Marmara University - Organic Chemistry, 2015
BSc, Marmara University - Chemistry, 2013

WORK EXPERIENCE

Year, Place, Enrollment
2015-2017, Izmir Institute of Technology, Research Scholar in TUBİTAK 1001 Project encoded 114Z940
2017-2019, Izmir Institute of Technology, Research Scholar in TUBİTAK 1001 Project encoded 117Z331

PUBLICATIONS

14. G Topcu, MM Demir; Sensors and Actuators A: Physical, 2019, 295, 237-243.
13. G Topcu, T Guner, E Inci, MM Demir; Sensors and Actuators A: Physical, 2019, 295, 503-511.
12. S Ozen, T Guner, G Topcu, M Ozcan, MM Demir, H Sahin; Journal of Applied Physics, 2019, 125 (22), 225705.
11. B Gokbukut, A Inanc, G Topcu, T Guner, MM Demir, MN Inci; The Journal of Physical Chemistry C, 2019, 123 (14), 9343-9351
10. G Topcu, G Koc, A Baba, MM Demir; Geothermics, 2019, 80, 86-91
9. G Topcu, A Celik, A Kandemir, A Baba, H Sahin, MM Demir; Geothermics, 2019, 77, 106-114
8. G Topcu, T Güner, MM Demir; Photonics and Nanostructures-Fundamentals and Applications, 2018, 29, 22-29.
7. T Guner, B Akbali, M Ozcan, G Topcu, MM Demir, H Sahin; The Journal of Physical Chemistry C, 2018, 122 (21), 11543-11549.
6. B Akbali, G Topcu, T Guner, M Ozcan, MM Demir, H Sahin; Physical Review Materials, 2018, 2 (3), 034601.
5. T Güner, G Topcu, U Savacı, A Genç, S Turan, E Sari, MM Demir; Nanotechnology, 2018, 29 (13), 135202.
4. A Çelik, G Topcu, T Isik, A Baba, N Horzum, MM Demir; Materials Science Forum, 2018, 915, 121-126.
3. G Topcu, E Baştürk, S Karataş; Journal of Vinyl and Additive Technology, 2018, 24, E133-E145.
2. A Çelik, G Topcu, A Baba, Y Akdogan, U Şentürk, MM Demir; Geothermics, 2017, 69, 65-73.
1. G Topcu, A Çelik, A Baba, MM Demir; ACS Energy & Fuels, 2017, 31 (8), 8489-8496.